1995

Computational Solution Of Inverse Problems With Simulated Annealing

Douglas John Moseley

National Library of Canada
Acquisitions and Bibliographic Services Branch
395 Wellington Street
Ottawa, Ontario
K1A 0N4

Bibliothèque nationale du Canada
Direction des acquisitions et des services bibliographiques
395, rue Wellington
Ottawa (Ontario)
K1A 0N4

Your file Votre référence

Our file Notre référence

NOTICE

The quality of this microform is heavily dependent upon the quality of the original thesis submitted for microfilming. Every effort has been made to ensure the highest quality of reproduction possible.

If pages are missing, contact the university which granted the degree.

Some pages may have indistinct print especially if the original pages were typed with a poor typewriter ribbon or if the university sent us an inferior photocopy.

Reproduction in full or in part of this microform is governed by the Canadian Copyright Act, R.S.C. 1970, c. C-30, and subsequent amendments.

AVIS

La qualité de cette microforme dépend grandement de la qualité de la thèse soumise au microfilmage. Nous avons tout fait pour assurer une qualité supérieure de reproduction.

S'il manque des pages, veuillez communiquer avec l'université qui a conféré le grade.

La qualité d'impression de certaines pages peut laisser à désirer, surtout si les pages originales ont été dactylographiées à l'aide d'un ruban usé ou si l'université nous a fait parvenir une photocopie de qualité inférieure.

La reproduction, même partielle, de cette microforme est soumise à la Loi canadienne sur le droit d'auteur, SRC 1970, c. C-30, et ses amendements subséquents.

Canada

LIST OF FIGURES

ISBN 0-612-03478-X

Canada

Name DOUGLAS J. MOSELEY

Dissertation Abstracts International is arranged by broad, general subject categories. Please select the one subject which most nearly describes the content of your dissertation. Enter the corresponding four-digit code in the spaces provided.

MATHEMATICS — SUBJECT TERM

0405 — SUBJECT CODE

U·M·I

Subject Categories

THE HUMANITIES AND SOCIAL SCIENCES

COMMUNICATIONS AND THE ARTS
- Architecture 0729
- Art History 0377
- [illegible] 0900
- [illegible]nce 0378
- Fine Arts 0357
- Information Science 0723
- Journalism 0391
- Library Science 0399
- Mass Communications 0708
- Music 0413
- Speech Communication 0459
- Theater 0465

EDUCATION
- General 0515
- Administration 0514
- Adult and Continuing 0516
- Agricultural 0517
- Art 0273
- Bilingual and Multicultural 0282
- Business 0688
- Community College 0275
- Curriculum and Instruction 0727
- Early Childhood 0518
- Elementary 0524
- Finance 0277
- Guidance and Counseling 0519
- Health 0680
- Higher 0745
- History of 0520
- Home Economics 0278
- Industrial 0521
- Language and Literature 0279
- Mathematics 0280
- Music 0522
- Philosophy of 0998
- Physical 0523
- Psychology 0525
- Reading 0535
- Religious 0527
- Sciences 0714
- Secondary 0533
- Social Sciences 0534
- Sociology of 0340
- Special 0529
- Teacher Training 0530
- Technology 0710
- Tests and Measurements 0288
- Vocational 0747

LANGUAGE, LITERATURE AND LINGUISTICS
- Language
  - General 0679
  - Ancient 0289
  - Linguistics 0290
  - Modern 0291
- Literature
  - General 0401
  - Classical 0294
  - Comparative 0295
  - Medieval 0297
  - Modern 0298
  - African 0316
  - American 0591
  - Asian 0305
  - Canadian (English) 0352
  - Canadian (French) 0355
  - English 0593
  - Germanic 0311
  - Latin American 0312
  - Middle Eastern 0315
  - Romance 0313
  - Slavic and East European 0314

PHILOSOPHY, RELIGION AND THEOLOGY
- Philosophy 0422
- Religion
  - General 0318
  - Biblical Studies 0321
  - Clergy 0319
  - History of 0320
  - Philosophy of 0322
- Theology 0469

SOCIAL SCIENCES
- American Studies 0323
- Anthropology
  - Archaeology 0324
  - Cultural 0326
  - Physical 0327
- Business Administration
  - General 0310
  - Accounting 0272
  - Banking 0770
  - Management 0454
  - Marketing 0338
- Canadian Studies 0385
- Economics
  - General 0501
  - Agricultural 0503
  - Commerce-Business 0505
  - Finance 0508
  - History 0509
  - Labor 0510
  - Theory 0511
- Folklore 0358
- Geography 0366
- Gerontology 0351
- History
  - General 0578
  - Ancient 0579
  - Medieval 0581
  - Modern 0582
  - Black 0328
  - African 0331
  - Asia, Australia and Oceania 0332
  - Canadian 0334
  - European 0335
  - Latin American 0336
  - Middle Eastern 0333
  - United States 0337
- History of Science 0585
- Law 0398
- Political Science
  - General 0615
  - International Law and Relations 0616
  - Public Administration 0617
- Recreation 0814
- Social Work 0452
- Sociology
  - General 0626
  - Criminology and Penology 0627
  - Demography 0938
  - Ethnic and Racial Studies 0631
  - Individual and Family Studies 0628
  - Industrial and Labor Relations 0629
  - Public and Social Welfare 0630
  - Social Structure and Development 0700
  - Theory and Methods 0344
- Transportation 0709
- Urban and Regional Planning 0999
- Women's Studies 0453

THE SCIENCES AND ENGINEERING

BIOLOGICAL SCIENCES
- Agriculture
  - General 0473
  - Agronomy 0285
  - Animal Culture and Nutrition 0475
  - Animal Pathology 0476
  - Food Science and Technology 0359
  - Forestry and Wildlife 0478
  - Plant Culture 0479
  - Plant Pathology 0480
  - Plant Physiology 0817
  - Range Management 0777
  - Wood Technology 0746
- Biology
  - General 0306
  - Anatomy 0287
  - Biostatistics 0308
  - Botany 0309
  - Cell 0379
  - Ecology 0329
  - Entomology 0353
  - Genetics 0369
  - Limnology 0793
  - Microbiology 0410
  - Molecular 0307
  - Neuroscience 0317
  - Oceanography 0416
  - Physiology 0433
  - Radiation 0821
  - Veterinary Science 0778
  - Zoology 0472
- Biophysics
  - General 0786
  - Medical 0760

EARTH SCIENCES
- Biogeochemistry 0425
- Geochemistry 0996
- Geodesy 0370
- Geology 0372
- Geophysics 0373
- Hydrology 0388
- Mineralogy 0411
- Paleobotany 0345
- Paleoecology 0426
- Paleontology 0418
- Paleozoology 0985
- Palynology 0427
- Physical Geography 0368
- Physical Oceanography 0415

HEALTH AND ENVIRONMENTAL SCIENCES
- Environmental Sciences 0768
- Health Sciences
  - General 0566
  - Audiology 0300
  - Chemotherapy 0992
  - Dentistry 0567
  - Education 0350
  - Hospital Management 0769
  - Human Development 0758
  - Immunology 0982
  - Medicine and Surgery 0564
  - Mental Health 0347
  - Nursing 0569
  - Nutrition 0570
  - Obstetrics and Gynecology 0380
  - Occupational Health and Therapy 0354
  - Ophthalmology 0381
  - Pathology 0571
  - Pharmacology 0419
  - Pharmacy 0572
  - Physical Therapy 0382
  - Public Health 0573
  - Radiology 0574
  - Recreation 0575
  - Speech Pathology 0460
  - Toxicology 0383
- Home Economics 0386

PHYSICAL SCIENCES
Pure Sciences
- Chemistry
  - General 0485
  - Agricultural 0749
  - Analytical 0486
  - Biochemistry 0487
  - Inorganic 0488
  - Nuclear 0738
  - Organic 0490
  - Pharmaceutical 0491
  - Physical 0494
  - Polymer 0495
  - Radiation 0754
- Mathematics 0405
- Physics
  - General 0605
  - Acoustics 0986
  - Astronomy and Astrophysics 0606
  - Atmospheric Science 0608
  - Atomic 0748
  - Electronics and Electricity 0607
  - Elementary Particles and High Energy 0798
  - Fluid and Plasma 0759
  - Molecular 0609
  - Nuclear 0610
  - Optics 0752
  - Radiation 0756
  - Solid State 0611
- Statistics 0463

Applied Sciences
- Applied Mechanics 0346
- Computer Science 0984
- Engineering
  - General 0537
  - Aerospace 0538
  - Agricultural 0539
  - Automotive 0540
  - Biomedical 0541
  - Chemical 0542
  - Civil 0543
  - Electronics and Electrical 0544
  - Heat and Thermodynamics 0348
  - Hydraulic 0545
  - Industrial 0546
  - Marine 0547
  - Materials Science 0794
  - Mechanical 0548
  - Metallurgy 0743
  - Mining 0551
  - Nuclear 0552
  - Packaging 0549
  - Petroleum 0765
  - Sanitary and Municipal 0554
  - System Science 0790
- Geotechnology 0428
- Operations Research 0796
- Plastics Technology 0795
- Textile Technology 0994

PSYCHOLOGY
- General 0621
- Behavioral 0384
- Clinical 0622
- Developmental 0620
- Experimental 0623
- Industrial 0624
- Personality 0625
- Physiological 0989
- Psychobiology 0349
- Psychometrics 0632
- Social 0451

ABSTRACT

The examination of inverse problems represents a fascinating, diverse and difficult area of study. Almost any problem in mathematics, physics and engineering has an associated inverse problem. The method of quasi-solutions allows one to reformulate inverse problems as a function minimization involving the associated forward problem. The function to minimize is known as a penalty function or cost function and is defined as the least squares difference between some measured quantity and a quantity computed by the forward solver. This strategy avoids the need to construct the inverse operator. The forward problem is often well posed and can be solved quickly and accurately by various numerical solution techniques. The cost function, however, is typically a complicated multidimensional, multimodal surface. These properties make it difficult to locate the global minimum where the quasi-solution exists.

The simulated annealing algorithm performs well at minimizing functions with multiple local minima and hence has been employed in the quasi-solution of the inverse problem. Regularization techniques in the area of inverse problems attempt to better condition the problem by removing the local minimum from the cost function. Focus in this work has been placed on finding the global minimum of the multimodal cost function rather than strongly regularizing the penalty function. Two physical applications are chosen to test the feasibility of the proposed inversion method.

The first application involves the mise-à-la-masse electromagnetic prospecting technique from geophysics. This technique attempts to recover the size, shape and orientation of buried conductive ore bodies based on surface measurements. Here, a finite difference method is employed to solve the potential equation in a 3D semi-infinite medium.

The second application focuses on the scattering of acoustic waves by a 2D inhomogeneous medium. In this field, acoustic waves scattered from incident waves are used to reconstruct the index of refraction of the inhomogeniety. The incident waves are time harmonic plane waves which lie in the resonance region. A special hybrid partial differential equation/integral equation solution technique is employed to solve the direct problem.

To Joanne

To Jack and his new brother/sister

To my family

ACKNOWLEDGEMENTS

I am deeply indebted to Dr. H. Rasmussen for his help in the development and preparation of this document.

TABLE OF CONTENTS

LIST OF FIGURES

LIST OF TABLES

NOMENCLATURE

A	Radius which contains inhomogeneous index of refraction for parameterization.
C	cost function, $C(x) = \|x^{c} - x^{m}\|$.
$c(\boldsymbol{x})$	speed of sound in inhomogeniety.
c_0	speed of sound in background fluid.
$\boldsymbol{d}$	incident wave direction. $\boldsymbol{d} = (\cos(\alpha), \sin(\alpha))$.
$\boldsymbol{E}$	electric field, $\boldsymbol{E} = \nabla\phi$.
$\boldsymbol{E}^{c}$	computed electric field on the surface.
$\boldsymbol{E}^{m}$	measured electric field on the surface.
$H_n^{(1)}(x)$	Hankel function of the first kind of order n, $H_n^{(1)}(x) = J_n(x) + iY_n(x)$.
i	complex constant, $i = \sqrt{-1}$.
$\boldsymbol{J}$	current density, $\boldsymbol{J} = \sigma\boldsymbol{E}$.
J_n	Bessel function of the first kind of integer order n.
k	wave number of incident wave, $k = 2\pi/\lambda$.
L	(Chapter 3) depth of buried source electrode. (Chapter 4) number of axial terms used in the Fourier expansion of $\hat{n}(\theta, R)$.
M	number of radial terms used in the Fourier expansion of $\hat{n}(\theta, R)$.
n	index of refraction defined by $n = c_0^2/c^2$.
$\tilde{n}(\theta, R)$	index of refraction found by method of quasi-solutions.
$\hat{n}(\theta, R)$	index of refraction parameterized by 2D Fourier series.
N_i	(Chapter 3) number of finite difference grid points in x-direction. (Chapter 4) number of finite difference grid points in axial direction.
N_j	(Chapter 3) number of finite difference grid points in y-direction. (Chapter 4) number of finite difference grid points in radial direction.
N_k	number of finite difference grid points in z-direction.
N_{iu}	number of uniformly spaced finite difference grid points in x-direction.
N_{ju}	number of uniformly spaced finite difference grid points in y-direction.
N_{ku}	number of uniformly spaced finite difference grid points in z-direction.
N_α	number of irradiation directions.
r	radial distance variable.

R non-dimensionalized radial distance variable ($R = \frac{kr}{2\pi}$).

R_1 radius of computational domain.

R_∞ radius where farfield pattern will be estimated based on $u_{ff}(\theta) \approx \sqrt{R_\infty}\exp(-2\pi i R_\infty)u_s(\theta, R_\infty)$.

U velocity potential of sound wave. The longitudinal fluid velocity is found from $v(x,t) = \frac{1}{\rho_0}\nabla U(x,t)$.

u complex velocity potential for time-harmonic sound waves in the Fourier domain given by $U(x,t) = Re\{u(x)e^{-i\omega t}\}$. The superposition of incident and scattered waves yields $u = u_i + u_s$.

u_i incident wave field. For plane parallel waves propagating in direction d, $u_i(x) = e^{ikx\cdot d}$.

u_s scattered wave field.

$\tilde{u}_s$ numerical approximation to scattered wave field from finite difference solution of Helmholtz's equation.

u_{ff} far-field wave pattern. Related to the scattered wave field by $u_s(\theta, R) = \frac{e^{2\pi i R}}{\sqrt{R}}u_{ff}(\theta) + O(1/R)$.

u_{ff}^m measured far-field wave pattern.

$\tilde{u}_{ff}$ computed far-field wave pattern from finite-difference solution.

$\Delta x, \Delta y, \Delta z$ grid spacing of 3D rectangular finite difference mesh.

$\Delta\theta, \Delta R$ grid spacing for 2D polar coordinate finite difference mesh.

Y_n Bessel function of the second kind of order n.

α (Chapter 2) regularization paramter.
(Chapter 4) angle of incidence between positive x-axis and direction of incident wave u_i.

β angle between unit radial vector and outward normal to face of computational domain used for the application of the Robbin boundary condition.

γ dip angle of buried ore body.

λ wave-length of incident waves.

ϕ electrostatic potential.

σ conductivity of inhomogeneous medium.

θ (Chapter 3) strike angle of buried ore body.
(Chapter 4) angular position variable.

ω_0 angular frequency of incident waves in background fluid, $c_0 = \frac{\omega_0}{k}$.

ω angular frequency of incident waves, $c = \frac{\omega}{k}$.

χ reduction factor for cooling schedule.

CHAPTER 1

Introduction

The study of inverse problems is a fascinating one which transcends the boundaries of any one discipline. Active research in this field can be found in the disciplines of pure and applied mathematics, computer science, medical physics, geophysics and engineering to name a few.

In the current work, an inverse problem is posed as a minimization problem through the use of a cost function. The cost function is based on a least-squares difference between some measured data and calculated data. The calculated data is collected from the solution of the associated direct problem. This technique is sometimes referred to as the *output least-squares* formulation. The posed minimization problem is solved with the heuristic technique called simulated annealing.

In Chapter 2, some historical context to the study of inverse problems is provided. The definition of a well-posed problem is stated as well as the definition of a quasi-solution. The notion of stability of solutions is also introduced. An illustrative example in the area of ill-posed problems is found in the backwards heat equation. This classic example exhibits existence and uniqueness but violates the stability criterion. The method of quasi-solutions applied to this problem provides illuminating results. Next, the regularization of inverse problems is discussed. Regularization can be implemented with the addition of penalty terms to the penalty function or through limiting eligible solutions based on physical reasoning. The effects of regularization and regularization error are demonstrated with the backwards heat equation. An analogy to the solution of systems of linear algebraic equations can be drawn. Finally, simulated annealing, the proposed minimization technique to be used to extract the quasi-solution from the penalty function, is introduced.

The field of geophysics contains many interesting and difficult inverse problems. A class of methods use electromagnetic fields to infer the conductivity substructure of the earth. These fields can be either naturally occurring or artificially generated. Chapter 3 contains the first physical application of the proposed inversion algorithm. Here the mise-à-la-masse electromagnetic prospecting technique is examined. A numerical method

is proposed to solve the full 3 dimensional potential equation in a semi-infinite conductively inhomogeneous domain. This solution represents the solution to the forward problem. A physically based representation of the conductivity substructure is proposed. This parameterization coupled with the simulated annealing algorithm applied to the penalty function completes the inversion technique. Noisy synthetic data as well as data generated from the dimensions of a realistic ore body are used to validate the method.

Many inverse problems can be found in the field of medical imaging. These techniques often involve time harmonic waves to produce a scattered signal. The scattered waves are measured and used to reconstruct the medium. Ultrasound techniques use time harmonic acoustic waves to generate a scattering pattern. Differing speeds of sound (index of refraction) in the medium cause incident waves to scatter. The inverse problem attempts to reconstruct the index of refraction based on the scattered wave pattern from numerous incident directions. In Chapter 4 the inverse problem of acoustic waves scattered by an inhomogeneous medium is examined. The forward problem for time harmonic waves in two dimensions is governed by Helmholtz's equation. The only boundary condition is the Sommerfeld radiation condition. This boundary condition is only valid at infinity, which makes it difficult for standard numerical techniques. A specialized hybrid solution technique is developed, which uses a finite-difference mesh in the region of the inhomogeniety and an integral equation solution to propagate the scattered waves outward. The finite difference solution employs non-reflecting boundary conditions to minimize the effect of using the artificial boundaries of a computational domain. The direct problem is verified against an analytic solution from obstacle scattering as well as an iterative Born approximation integral equation solution from medium scattering. A 2D Fourier series is used to parameterize the index of refraction. Implementation of a quasi-solution minimization with simulated annealing completes the proposed solution to this inverse problem. The inverse solver is verified using synthetic data created from three known indices of refraction.

CHAPTER 2

Inverse Problems

2.1 Introduction

Inverse problems often arise from classical *direct* problems. These direct problems are motivated by many areas of mathematics and physics. Consider a normed space X known as the domain space. Let F represent a normed space containing the range space. Consider the operator A which maps an element $x \in X$ from the range space to a solution $f \in F$ in the range space (figure 2-1). The direct problem then appears in the generic form of

$$Ax = f. \tag{2.1.1}$$

Here, A can be a linear, non-linear, integral or differential operator. Given x, one can apply the operator A to find the solution f. In the work presented here the solution to the direct problem is assumed to be well-posed. Application of the operator may require a numerical approach if analytic methods do not exist.

The inverse problem related to (2.1.1) treats the direct problem in a reverse way. Instead of using x to find f, the inverse problem requires finding x given f. The solution of this inverse problem is achieved by application of the inverse operator, A^{-1}. Hence, in principle the solution is given by

$$x = A^{-1}f. \tag{2.1.2}$$

Unfortunately, the inverse operator may be impossible to construct, or the inverse problem may be ill-posed. The study of inverse problems is intimately connected to the study of ill-posed problems, to which we now turn our attention.

2.2 Concept of Well-Posedness

Hadamard [24] formulated the concept of well-posed problems. He suggested that a mathematical problem must exhibit three properties to be considered well-posed:

1) Existence - for every $x \in X$, there exists an image f
2) Uniqueness - A is 1-1
3) Stability - the solution depends continuously on the data

Existence implies that there exists an image f in the range space for any x in the domain space. Uniqueness is the quality that indicates that two distinct elements in the domain space, map to two distinct points in the range space. That is

$$Ax_1 = Ax_2 \Leftrightarrow x_1 = x_2, \quad \forall\, x_1, x_2 \in X. \tag{2.2.1}$$

Stability ensures that the solution depends continuously on the data. Consider two nearby elements x_1, x_2 such that

$$\| x_1 - x_2 \| < \varepsilon, \tag{2.2.2}$$

for $\varepsilon \geq 0$ and $\| \cdot \|$ an appropriate norm. Let the mappings of these two elements through A be denoted by f_1, f_2 then there exists a $\delta \geq 0$ such that

$$\| f_1 - f_2 \| < \delta. \tag{2.2.3}$$

The forward problem is stable, if δ is bounded for all $x_1, x_2 \in X$. This condition is equivalent to saying that the inverse operator must be continuous [10]. A problem is considered ill-posed if its solutions violate any of these criteria. The method of quasi-solutions provides a means to approximate the solution of ill-posed inverse problems.

2.3 Method of Quasi-solutions

The method of quasi-solutions, as introduced by Tikhonov [49], involves finding a solution which best approximates the solution to the inverse problem in a least-squares sense. A quasi-solution $\tilde{x}$ is defined by

$$\tilde{x} = \inf_{x \in X} \| Ax - f \|, \tag{2.3.1}$$

where $\| \cdot \|$ is an appropriate norm defined on F. Equation (2.3.1) is also referred to as the output least-squares solution. The quantity to be minimized $\| Ax - f \|$ is referred to as the penalty function. The quasi-solution $\tilde{x}$ is unique for any given f, provided that $\| \tilde{x} \| \leq \rho$ for some $\rho > 0$ [27][28]. The advantages of this approach are two-fold.

First, calculation of the inverse operator A^{-1} is not required. This is advantageous since the operator may be difficult or impossible to construct analytically. Approximating the inverse operator is also an additional source for error.

Secondly, a quasi-solution exists even for $f \notin R(AX)$. That is, a quasi-solution can be found even if the data does not lie in the range space of the operator A. This is an important concept in solving inverse problems motivated by physical situations. Measured data is always subject to uncertainty due to instrument error. Even exact data is subject to round-off error if it is represented using a finite precision computer. The input data to an inverse problem is more realistically represented by f^δ where

$$\|f - f^\delta\| < \delta. \tag{2.3.2}$$

Here, $\delta \geq 0$ represents the uncertainty level in the measured data. It is quite possible that f^δ may lie outside the range space of AX as in figure 2-2a. Application of the exact inverse operator to f^δ would yield an undefined result. The quasi-solution, however, would still find a valid solution since a minimum must always exist.

Example 2-1: For an example of this phenomenon, consider the simple non-linear operator defined by

$$\begin{gathered} Ax = f \\ x \in X, \quad f \in F \\ X \equiv \mathcal{R}, \quad F \equiv \mathcal{R} \\ A : x \rightarrow x^2 \end{gathered} \tag{2.3.3}$$

The inverse operator can be easily constructed

$$A^{-1} : f \rightarrow \pm\sqrt{f}, \quad f \geq 0. \tag{2.3.4}$$

Note that the inverse operator exhibits non-uniqueness due to the positive and negative roots. This complication can be remedied by considering, for example, only positive roots. The range space for this operator is all non-negative real values. In attempting to solve the inverse problem for the data $f=0$, suppose that measurement error is present when the data is acquired such that

$$f^\delta = -\delta, \quad \delta > 0. \tag{2.3.5}$$

Applying the inverse operator of (2.3.4) yields an undefined result because of the square root of a negative number, while the quasi-solution given by

$$\tilde{x} = \inf_{x \in X} \|x^2 - f^\delta\|, \tag{2.3.6}$$

finds the solution $\tilde{x} = 0$ as seen in figure 2-3. In this figure, the surface represents the penalty function surface as a function of the data f and the solution x. The locus of minimum values represent the quasi-solutions. Hence, an inverse problem using quasi-solutions guarantees existence of a solution since a minimum must always exist. The quasi-solution may not be close to the true solution, but it still exists.

An important concept in solving inverse problems relates to the stability of the solution calculated. This is Hadamard's third criterion. A solution must exhibit continuous dependence upon its data or initial conditions to be considered well-posed. If there is a small perturbation in the data or the initial conditions (as from measurement or round-off error), this should lead to a corresponding predictable and bounded change in the solution.

An excellent example of an ill-posed inverse problem which violates continuous dependence on its initial conditions is the 1-D backwards heat equation. The well known classical 1-D diffusion equation with Dirichlet boundary conditions involves the evolution of a temperature distribution in a finite 1-D rod given the initial temperature profile. The definition is

$$\mathcal{D} = \{(x,t) \in \mathcal{R}^2 \mid 0 \le x \le \pi, t \ge 0\}$$

$$u = u(x,t), \quad u: \mathcal{R}^2 \to \mathcal{R}$$

$$f = f(x), \quad f: \mathcal{R} \to \mathcal{R}$$

$$u_t - u_{xx} = 0, \quad \text{in } \mathcal{D} \tag{2.3.7}$$

$$u(0,t) = u(\pi,t) = 0, \quad t \ge 0$$

$$u(x,0) = f(x), \quad 0 \le x \le \pi.$$

This PDE can be solved using separation of variables to give a temperature profile at any time greater than zero. The solution is

$$u(x,t) = \sum_{n=1}^{\infty} e^{-n^2 t} a_n \sin(nx), \tag{2.3.8}$$

where the Fourier coefficients a_n, can be calculated from the initial profile

$$a_n = \frac{2}{\pi} \int_0^{\pi} f(x) \sin(nx) dx. \tag{2.3.9}$$

The Dirichlet boundary conditions ensure that

(2.3.10) $$\lim_{t \to \infty} u(x,t) = 0.$$

Let the temperature profile at time T ($T>0$) be

(2.3.11) $$\psi(x) = u(x,T).$$

This forward problem is well-posed. Hence, specifying an initial profile f uniquely determines the profile at time T given by ψ. An analytic solution to (2.3.7) can be seen in figure 2-4 for the initial profile $f(x) = \sin(x)$. Notice that the amplitude of the initial profile diminishes quickly in time.

The inverse problem associated with this direct problem is known as the backward heat equation [49]. The backward heat equation attempts to calculate the initial profile f given the profile ψ at time T. Hence, information (temperature profile) is projected backwards in time.

Example 2-2: The inverse problem representing the backward heat equation is described by,

$$u = u(x,t): R^2 \to R$$

$$\psi = \psi(x): R \to R$$

(2.3.12) $$u_t - u_{xx} = 0$$

$$u(0,t) = u(\pi,t) = 0$$

$$u(x,T) = \psi(x)$$

The initial profile f can be calculated from ψ by using

(2.3.13) $$f(x) = u(x,0),$$

and

(2.3.14) $$u(x,t) = \sum_{m=1}^{\infty} e^{-m^2 t} b_m \sin(mx),$$

where the Fourier coefficients are

(2.3.15) $$b_m = \frac{2}{\pi} e^{m^2 T} \int_0^{\pi} \psi(x) \sin(mx) dx.$$

To show the instability of the inverse problem, consider a downstream temperature profile of (2.3.12) given by

$$\psi_1(x) = k\sin(mx), \tag{2.3.16}$$

for m an integer and k an arbitrary real number. The corresponding initial profile can be calculated using (2.3.14) and (2.3.15) to yield

$$f_1(x) = ke^{m^2T}\sin(mx) \tag{2.3.17}$$

Now consider the nearby function to (2.3.16) described by

$$\psi_2(x) = (k+\varepsilon)\sin(mx), \tag{2.3.18}$$

with ε some small parameter. This data has a corresponding initial profile

$$f_2(x) = (k+\varepsilon)e^{m^2T}\sin(mx). \tag{2.3.19}$$

The L_2-norm difference between ψ_2 and ψ_1 is

$$\|\psi_2 - \psi_1\|_{L_2(0,\pi)} = \varepsilon\sqrt{\frac{\pi}{2}}. \tag{2.3.20}$$

These two profiles can be made arbitrarily close by allowing $\varepsilon \to 0$. However, the L_2-norm difference between f_2 and f_1 is

$$\|f_2 - f_1\|_{L_2(0,\pi)} = \varepsilon e^{m^2T}\sqrt{\frac{\pi}{2}}. \tag{2.3.21}$$

For a fixed error level ε, the difference in (2.3.21) can be made arbitrarily large by either increasing m, the frequency of the sine wave profile or by increasing T, the time at which the temperature is measured. Thus, the problem is ill-posed due to the lack of stability of the solutions.

Physical reasoning explains the nature of these instabilities. The instability caused by the frequency parameter is owed to the smoothing nature of the forward heat equation. High frequency information is quickly lost to diffusion in the forward heat equation. This is due to the $\exp\{-n^2t\}$ term in the forward solution (2.3.8). Thus, the task of trying to project a high frequency profile backward in time is more difficult than projecting a low frequency profile. The instability caused by the time parameter T can be attributed to the limit of (2.3.10). All initial profiles f diffuse out over time and converge to zero in the forward heat

equation. In the backward heat equation, T indicates the amount of time that the solution is projected back. If T is large, then the temperature profile will be nearly zero making it more difficult to project backwards in time. As $T \to \infty$, all temperature profiles converge to zero making a solution backwards in time impossible. These two properties of the diffusion equation can be seen in figure 2-5. Here, an initial profile $f(x) = \sin x + \sin 10x$ with a high and a low frequency component is substituted into the forward heat equation. Notice that the amplitude of the solutions diminishes quickly in time. This decrease is more pronounced for the high frequencies.

The lack of stable solutions to the backward heat equation can also be illustrated by application of the quasi-solution method described in (2.3.1). Let A be the linear differential operator of (2.3.7) which maps initial temperature profiles to temperature profiles at time T

(2.3.22) $$A : f \to \psi.$$

This forward problem is well-posed. Consider a special subset of the range space F such that

(2.3.23) $$f(m) = \sin(mx).$$

Hence, all eligible solutions of the inverse problems will be *sine* functions with an integer frequency. This restriction severely limits the solution space but is useful for demonstration purposes. In addition, let the set Ψ, the range space, be parameterized by

(2.3.23) $$\psi(n) = \sin(nx).$$

Hence, application of the operator A in (2.3.22) yields

(2.3.24) $$Af(m) = e^{-m^2 T} \sin(mx).$$

The penalty function to minimize for the quasi-solution $\tilde{m}$ is

(2.3.25a) $$\tilde{m} = \inf_{f(m) \in F} \| Af(m) - \psi(n) \|_{L_2(0,\pi)}$$

(2.3.25b) $$\left\| e^{-m^2 T} \sin(mx) - \sin(nx) \right\|_{L_2(0,\pi)} = \begin{cases} \frac{\pi}{2}\left(e^{-m^2 T} - 1\right)^2, & n = m \\ \frac{\pi}{2}\left(1 + e^{-2m^2 T}\right), & n \neq m \end{cases}.$$

A graph of the penalty function versus the parameters (m,n) can be seen in figure 2-6. The shallow trench in the surface along the line $m=n$ corresponds to the locus of quasi-solutions $\tilde{m}$. One uses this surface as follows: given the data point n corresponding to the frequency of the measured profile at time T, the quasi-solution $\tilde{m}$ corresponds to the minimum of (2.3.25). For small values of n, the minimum of (2.3.25) is well defined. As the data value n is increased (higher frequencies) the minimum becomes less distinguishable. The function flattens out making the task of locating the minimum along $n=m$ nearly impossible, indicating that the continuous dependence of the solution on the data is lost. The other factor which accelerates the flattening out of this function, and hence the existence of a distinguishable minimum, is the parameter T. This parameter represents the length of time the inverse problem is attempting to project back. As predicted by (2.3.21), increasing T or increasing n decreases the dependence of the solution on the data and hence reduces the stability of the problem.

A method similar to the method of quasi-solutions can be seen in the numerical solution of systems of linear algebraic equations. Consider the linear system

$$\boldsymbol{A}\boldsymbol{x} = \boldsymbol{b}, \tag{2.3.26}$$

where $\boldsymbol{A}$ is an $n \times n$ matrix and $\boldsymbol{x}, \boldsymbol{b}$ are vectors in $\mathcal{R}^n$. The inverse problem requires finding $\boldsymbol{x}$ given $\boldsymbol{b}$. Direct solution methods such as LU decomposition or Gaussian elimination construct the inverse operator $\boldsymbol{A}^{-1}$ for the solution of (2.3.26). Iterative solutions, however, avoid computing the inverse operator explicitly. Generally, these methods [2] approximate the solution by minimizing the residual

$$r(\boldsymbol{x}) = \|\boldsymbol{A}\boldsymbol{x} - \boldsymbol{b}\|. \tag{2.3.27}$$

Finding the minimum residual is equivalent to computing the quasi-solution. A consistent method to add stability to ill-posed inverse problems is through the use of regularization.

2.4 Regularization of Inverse Problems

Regularization helps create well-posed problems from ill-posed problems by adding stability to the solution method. Two distinct approaches can be taken to regularize an ill-posed inverse problem.

The first approach attempts to limit the set of eligible solutions based on physical arguments. For example, continuity, differentiability, or non-negativity are sometimes properties associated with the physical data. In the case of the backward heat equation, physical reasoning could be used to limit the set of initial profiles to continuous and differentiable functions.

The second regularization strategy proposed by Tikhonov attempts to condition the non-linear inverse operator. This regularization can appear in the use of a penalty term added to the penalty function. For this reason the method is called penalized least-squares. A thorough discussion of the convergence behaviour of the penalized least-squares method can be found in [5]. The quasi-solution expression now becomes

$$\tilde{x} = \inf_{x \in X} \{\|Ax - f\| + \alpha E(x)\}, \tag{2.4.1}$$

where $E(x)$ is the penalty term, and α is the regularization parameter. The penalty term is chosen such that $E(x) \geq 0$ for all x. Increasing the value of the regularization parameter α increases the amount of regularization and in turn the stability of the inverse problem. If $\alpha = 0$, then (2.4.1) returns to the previously posed quasi-solution of (2.3.1). This property is a requirement of any regularization scheme. A careful choice of the penalty term will discourage undesired properties or encourage desired properties in the solution. For example, properties such as entropy, smoothness, or minimum value can be encouraged or discouraged. The choice of the penalty term is usually left to the physical context of the inverse problem.

Applying regularization to add stability can be illustrated by example 2-2 of the previous section. Here, the true solution lies along the line $m=n$ as seen in figure 2-6. Direct application of the quasi-solution method gives accurate solution values of n up to $n=6$. For $n>6$ the minimum becomes indistinguishable and the problem loses stability. A penalty term based on the gradient squared is added to regularize the problem. The penalty term is

$$\|f(m)\|^2 = m^2\pi. \tag{2.4.2}$$

When the penalty term is included in (2.3.25) the cost function becomes

$$C(n;m,T) = \left\| e^{-m^2T} \sin(mx) - \sin(nx) \right\|_{L_2(0,\pi)} + \alpha m^2\pi. \tag{2.4.3}$$

The surface plot of the regularized penalty function with $\alpha = 0.01$ can be seen in figure 2-7. The regularization yields a stable solution for all n as demonstrated by the pronounced minimum. The true solution lies along the line $n=m$. While the solution is now stable, it is only accurate up to $n=7$. The error in the quasi-solution can be attributed to the regularization.

2.5 Regularization Error

Creating a well-posed problem from an ill-posed problem with the use of regularization may generate a dubious solution. This phenomenon is known as regularization error.

Firstly, limiting the search space of the quasi-solution may actually exclude the true solution. Care must be taken to ensure that the parameterization of the solution space allows a reasonable approximation to the solution.

Regularization of the inverse operator increases stability of the solution scheme. However, this technique allows a stable answer to be found to a different problem. If the transformed problem is significantly different from the original inverse problem the solution may be meaningless. For example, a problem with measurement error in the data allows one to write

$$\|f - f^{\delta}\| \le \delta. \tag{2.5.1}$$

Here, f is the exact data corresponding to the exact solution x, while f^{δ} is the measured data with some error represented by the small parameter δ. Let the quasi-solution generated with regularization be denoted by x_{α}^{δ}. The error in the solution to the inverse problem can be estimated by [10]

$$\|x - x_{\alpha}^{\delta}\| \le \delta \|R_{\alpha}\| + \|R_{\alpha}(Ax) - x\|, \tag{2.5.2}$$

where R_{α} is the regularized inverse operator. The regularized operator can be defined in terms of the previous quasi-solution definition with,

$$R_{\alpha}: f \rightarrow x, \tag{2.5.3}$$

$$R_{\alpha}(f) = \tilde{x} = \inf_{x \in X} \{\|Ax - f\| + \alpha E(x)\}.$$

The first term on the right hand side of (2.5.2) represents error due to the uncertainty in the measured data as well as the norm of the regularized operator. The second term represents error caused by the regularization. This expression represents the fundamental concern when regularization is imposed. If weak regularization is used ($\alpha \to 0^+$), the second term will disappear since $R_\alpha \to A^{-1}$. However, the first term will expand because of the ill-posed nature of the problem (ie. $\|A^{-1}\| \to \infty$). If strong regularization is used, the first term will diminish since the regularized operator will be well conditioned. The second term will increase because the regularized operator will be a poorer approximation to the inverse operator. Hence, strong regularization adds stability to the problem at the expense of accuracy. Ideally, the value of the regularization parameter is chosen as small as possible while still yielding stable solutions. Estimation of this parameter *a-priori* can prove difficult [38][49].

Regularization error is illustrated clearly by examining the backward heat of equation presented in Example 2-2. Comparing figure 2-8 to figure 2-7 shows differing behaviour of the quasi-solution. In figure 2-8, the regularization parameter is $\alpha = 0.1$. This value provides a well pronounced minimum which ensures stability, however, the regularized solution departs from the true solution after $n=5$. The solution in figure 2-7, where $\alpha = 0.01$, has a less pronounced minimum but provides exact solutions until $n=7$. Hence, increasing the value of the regularization parameter causes stability to increase and accuracy to decrease.

Finding the quasi-solution is now equivalent to locating the global minimum of the penalty function. The minimization algorithm used in the present work is simulated annealing.

2.6 Minimization with Simulated Annealing

When using the quasi-solution approach of (2.3.1), the solution of an inverse problem becomes an exercise in function minimization. The function to minimize in this case is the output least-squares

(2.6.1) $$C(x;f) = \|Ax - f\|,$$

where C is known as the cost function. Given the data f, the goal is to find an x which yields a minimum cost. Many algorithms exist for the minimization of functions [7]. For example, a gradient method such as Newton's method or conjugate gradient could be used to seek a minimum. Gradient methods require determination of the derivatives of the cost function (analytically or otherwise). This could be difficult or costly in the case of a non-linear function such as (2.6.1). Also, a derivative method could become easily trapped in a local minimum where no better *downhill* solutions exist. The cost functions derived from the quasi-solution method applied to inverse problems are often multimodal allowing for the possibility of trapping a derivative method. A suitable heuristic technique for this type of cost function is simulated annealing. It is worth emphasizing that simulated annealing is a heuristic method. It does not guarantee the discovery of the global minimum, although it performs well at finding a near global minimum.

Simulated annealing is based on the Metropolis algorithm [15] and draws analogies to the freezing of crystals. This minimization procedure requires the following formulation:

1) Description of all possible system configurations.

2) Generator of random changes to the current configuration.

3) Cost Function (to maximize or minimize)

4) Control Parameter T to step down (annealing schedule)

Let the current configuration of the system be given by the current value of x in (2.6.1). Generally, x is a continuous n-dimensional function. It is difficult to describe such a system state since it has an infinite number of basis vectors. Further, the perturbations to these configurations is arduous since each of the infinite dimensions can achieve a continuum of values. It is for this reason that the magnitude of the perturbation raises a difficult question. In a discrete system such as the Travelling Salesman Problem in [31], the random changes are straightforward. In the proposed problem, the state x is a real valued function and hence can achieve a continuum of states in a infinite number of dimensions. Simulated annealing minimization of functions with continuous variables has been discussed in [6,12]. The method used in [12] involves choosing at random an n-dimensional vector from the n-dimensional unit hypersphere, where n is the dimensionality of the function to be minimized. This unit vector is then multiplied by a set of scaling factors for each dimension.

The system state is then moved by the scaled vector. The shortcoming of this method lies in its lack of ability to adjust the scaling factors to changing sensitivities of the cost function with respect to its free parameters. For example, near the beginning of annealing, large configuration changes are desirable to allow the algorithm to sample the entire state space. Near the end of annealing, small changes are required to fine tune the solution.

The *annealing* process proceeds as follows:

a) start with an initial configuration

b) calculate cost function

c) generate random change to configuration

d) recalculate cost function

e) accept or reject step

f) adjust temperature if necessary

g) if annealing is complete, stop. else go to c)

The temperature parameter T is assigned an initial value greater than the average change in the cost function for any particular random configuration change. This is commonly referred to as the *melting* temperature. This initial temperature should be high enough so that the algorithm can choose any state in the solution domain, similar to a molecule being allowed to move throughout a liquid. Randomly selected configuration changes are performed at a particular temperature level until some maximum number are attempted or a preset limit of successful reconfigurations is achieved. Then the temperature is reduced based on some relationship. The lowering of temperature is known as the cooling or annealing schedule. The process is repeated until no successful changes occur or a minimum temperature is encountered. For Boltzmann annealing, the temperature at the kth level is

$$T_k = \chi^k T_0, \tag{2.6.1}$$

where T_0 is the initial temperature and $0 < \chi < 1$ is the reduction factor [19].

The ideal cooling schedule is difficult to predict. Cooling too quickly may result in *quenching* in which the cost function achieves a local rather than global minimum. Cooling too slowly wastes computational effort. Convergence results for the simulated annealing algorithm as well as ideal cooling schedules can be seen in [19]. As the temperature is

lowered, the system becomes less like a fluid and more like a solid. By performing the cooling sufficiently slowly, the system can cool into its *crystalline* state (global minimum cost). When no more changes are accepted, it is assumed that the minimum cost is reached, and the global minimum is found.

The annealing process continues until one of the following two stopping conditions is met: 1) the minimum value of the cost function is found, or 2) continuous perturbations of the system produce no acceptances, and hence no new configurations are generated.

The first criteria assumes that the theoretical minimum is known which is not always the case. Of course, with synthetic noise-free data, the minimum cost that is $C=0$. This fact determines exactly when to stop. With the introduction of uncertainty in the data or error in the forward solver, however, the global minimum is some unknown value greater than zero. The second criteria is usually gauged in terms of the ratio of acceptances to perturbation attempts. A suitable stopping condition exists if this ratio is less than 10%. It is true that this minimum may be local, but a careful choice of the annealing schedule will guarantee that this is a global minimum [19].

During annealing, the algorithm accepts step unconditionally if $\Delta C < 0$. If $\Delta C > 0$, then this step is accepted based on the Boltzmann probability

$$Pr(\Delta C) \sim \exp\left(-\frac{\Delta C}{T}\right). \tag{2.6.2}$$

This algorithm is not *greedy*, since there is always a finite chance of accepting a state with a higher cost value in order to jump out of a local minimum [14].

Another acceptance scheme different from the Boltzmann probability, was considered for comparison. Threshold accepting (TA), as proposed by [9], is similar to simulated annealing, however, the acceptance of a random change that increases the cost function is slightly different. In TA, a random change with $\Delta C > 0$ is accepted if $\Delta C < T$, where T is the control parameter. This prevents accepting new configurations which are far worse. In Boltzmann annealing, there is always a small but finite probability that a very bad change

is accepted. The advantages of threshold accepting are seen in the low temperature fine tuning of the solution. Here, computational effort is saved since poor changes, which would have to be undone later, are not accepted.

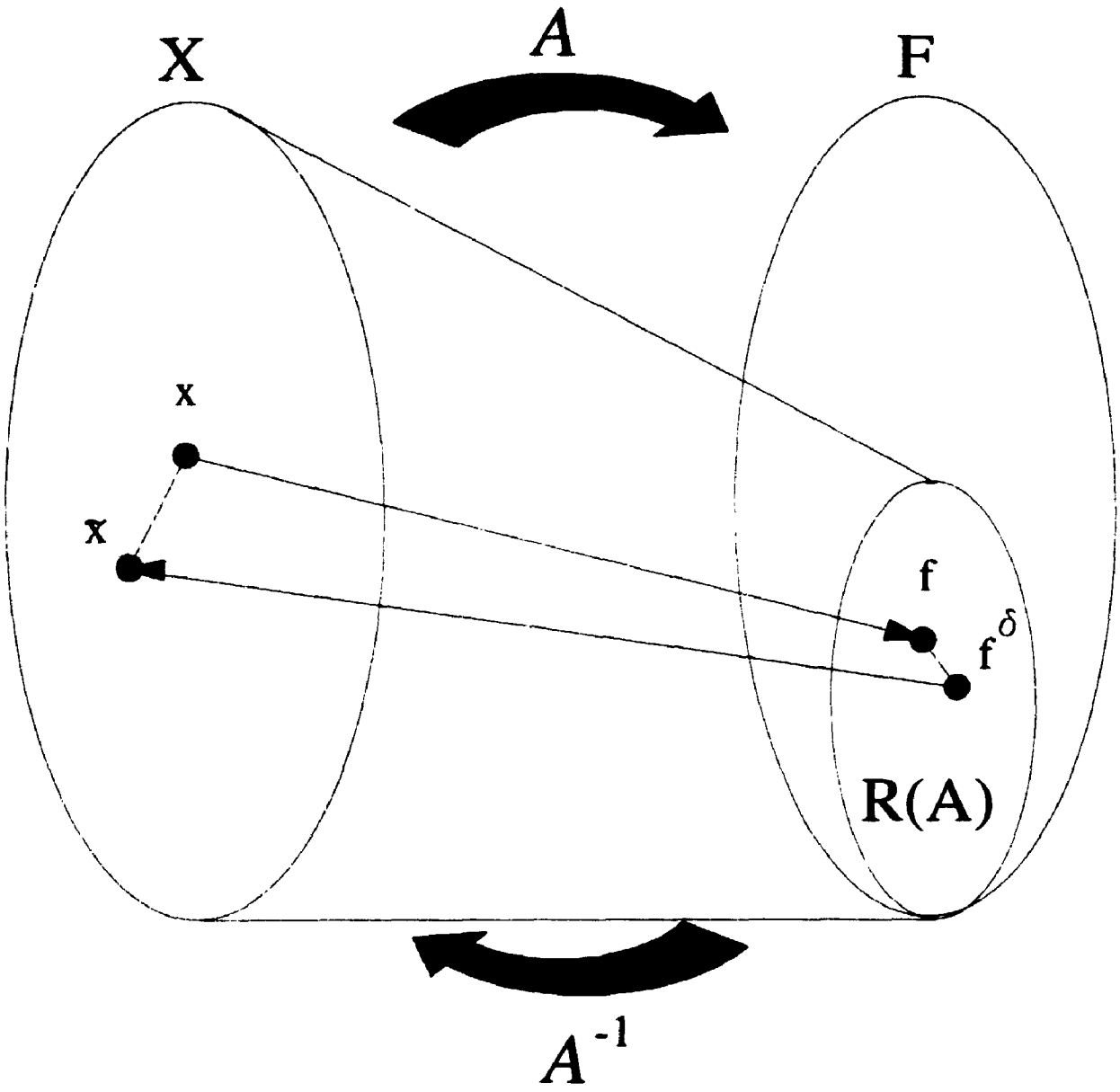

Figure 2-1. Schematic of the direct problem with the associated inverse problem. The data often contains some uncertainty represented by f^δ, where $\|f - f^\delta\| < \delta$. Whether or not this error leads to instability in the solution $\tilde{x}$ is a key aspect in the study of inverse problems.

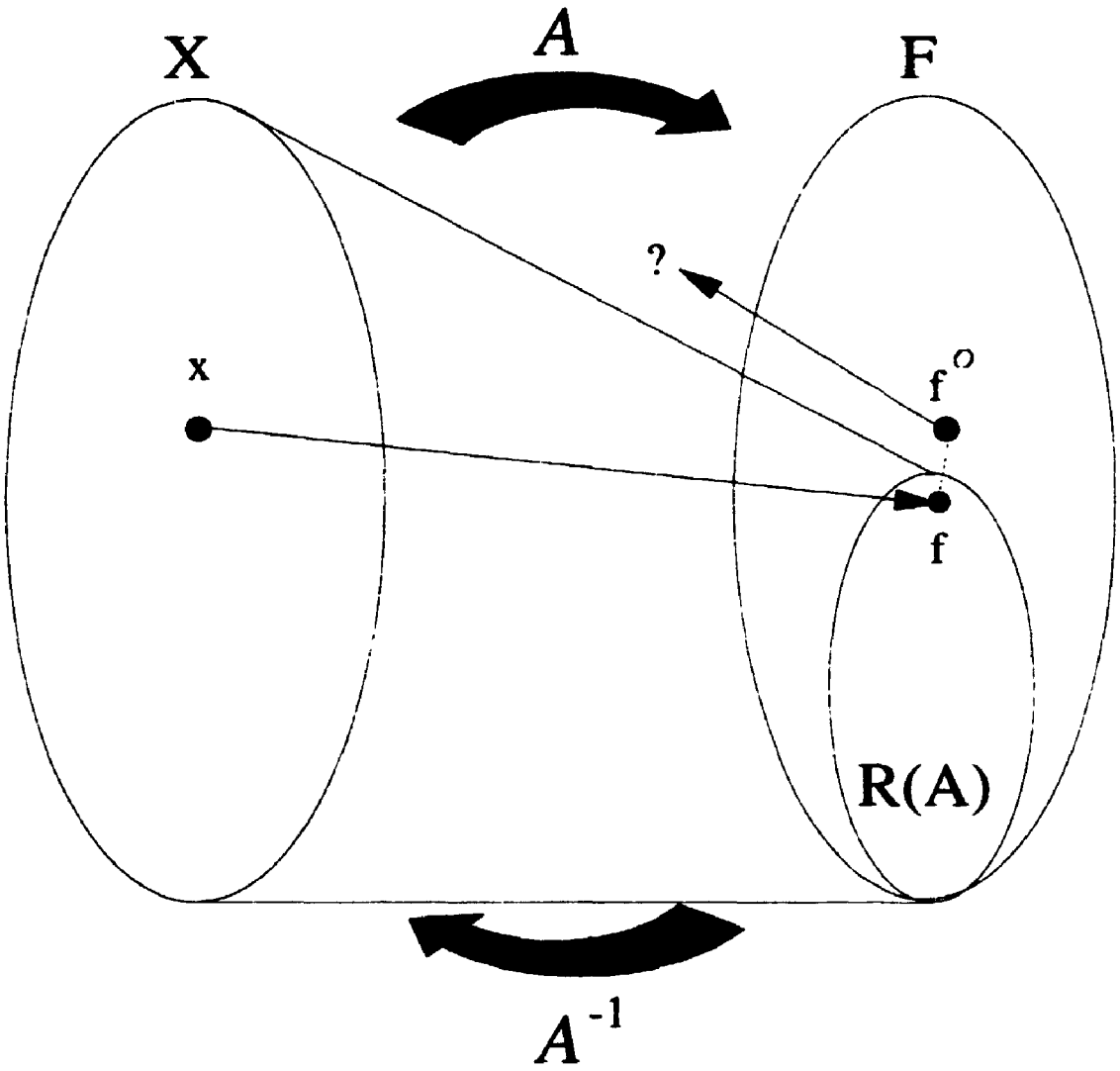

Figure 2-2a)

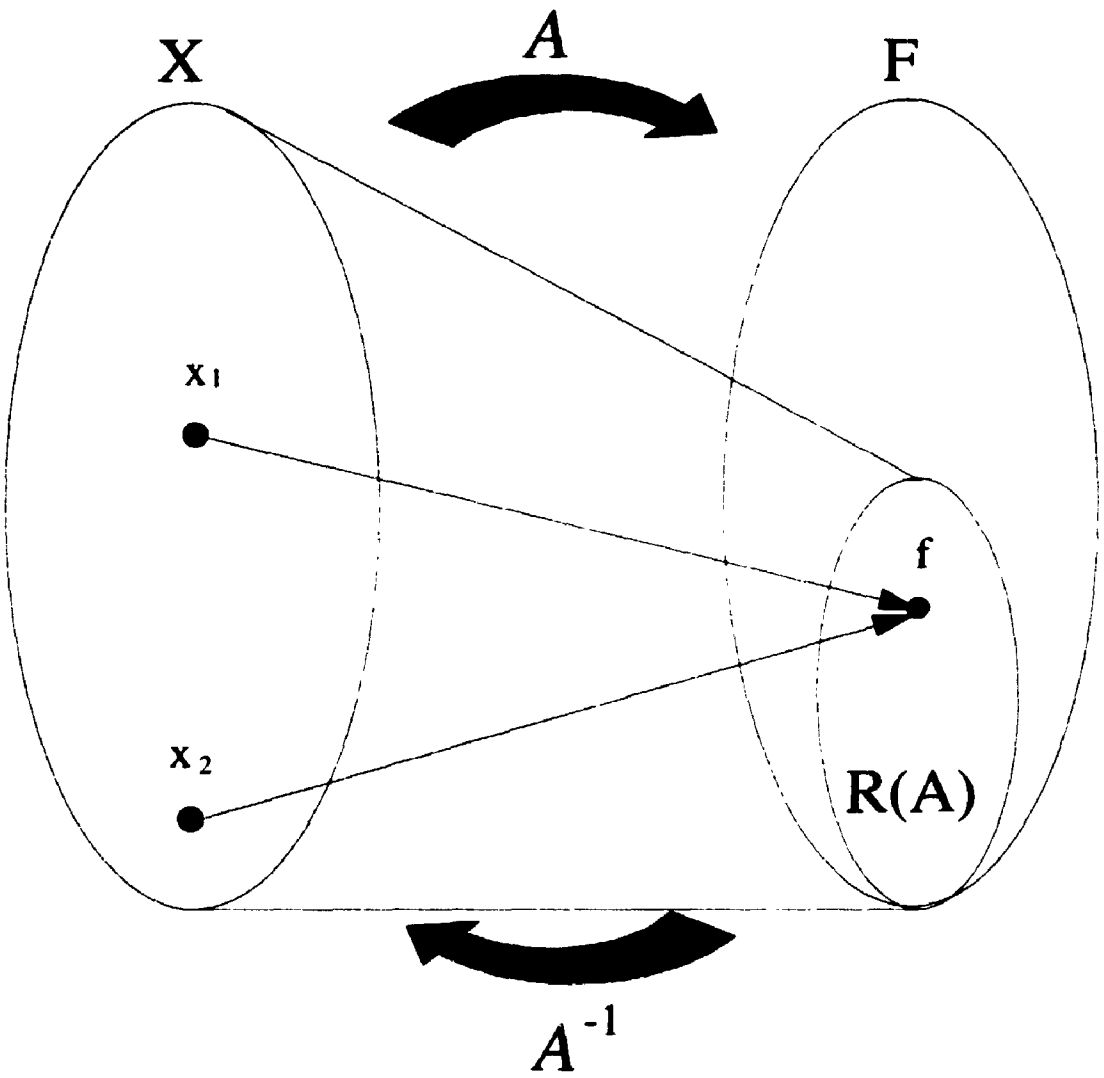

Figure 2-2b)

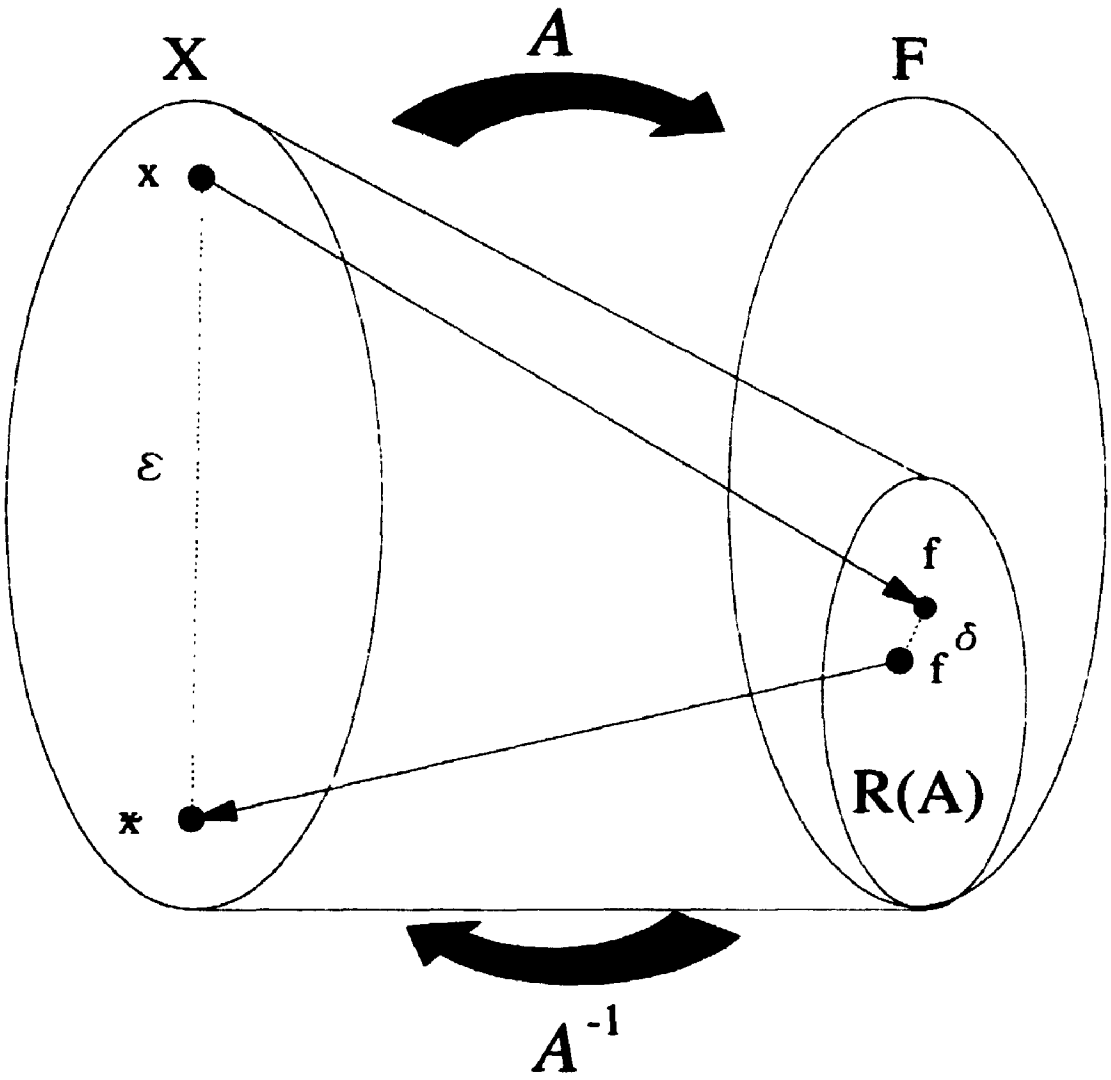

Figure 2-2c)

Figure 2-2. Sketches of systems whose inverses violate the axioms of well-posedness. a) Existence: the data f^{δ} lies outside of the range space of A, b) Uniqueness: the operator A is not one-to-one, and c) Continuous dependence: a small perturbation in the data leads to a significant perturbation in the solution of the inverse.

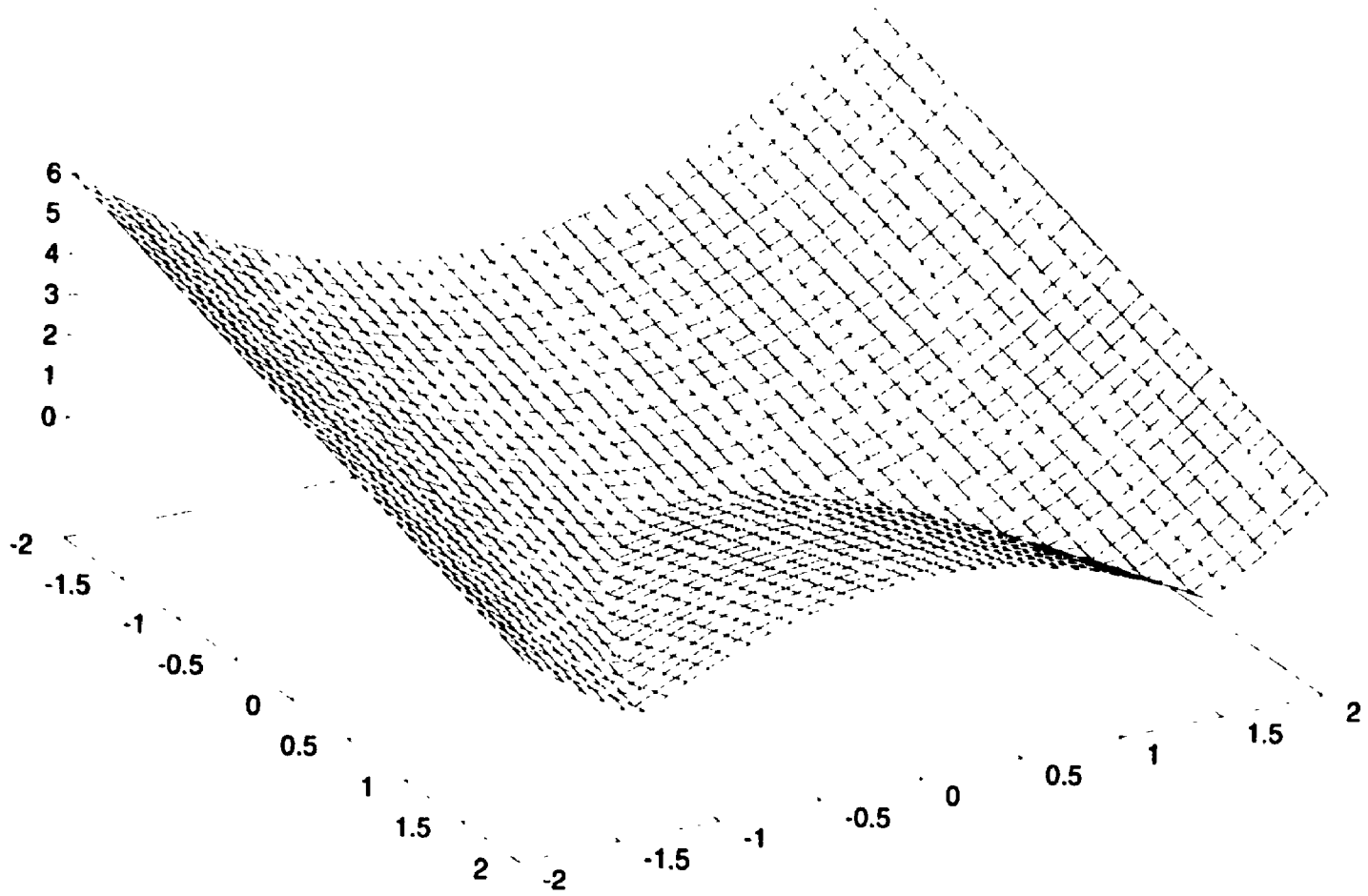

Figure 2-3. Output least-squares surface for the operator $A: x \rightarrow x^2$. The locus of minimum points represent the quasi-solution $\tilde{x}$, for various values of data f.

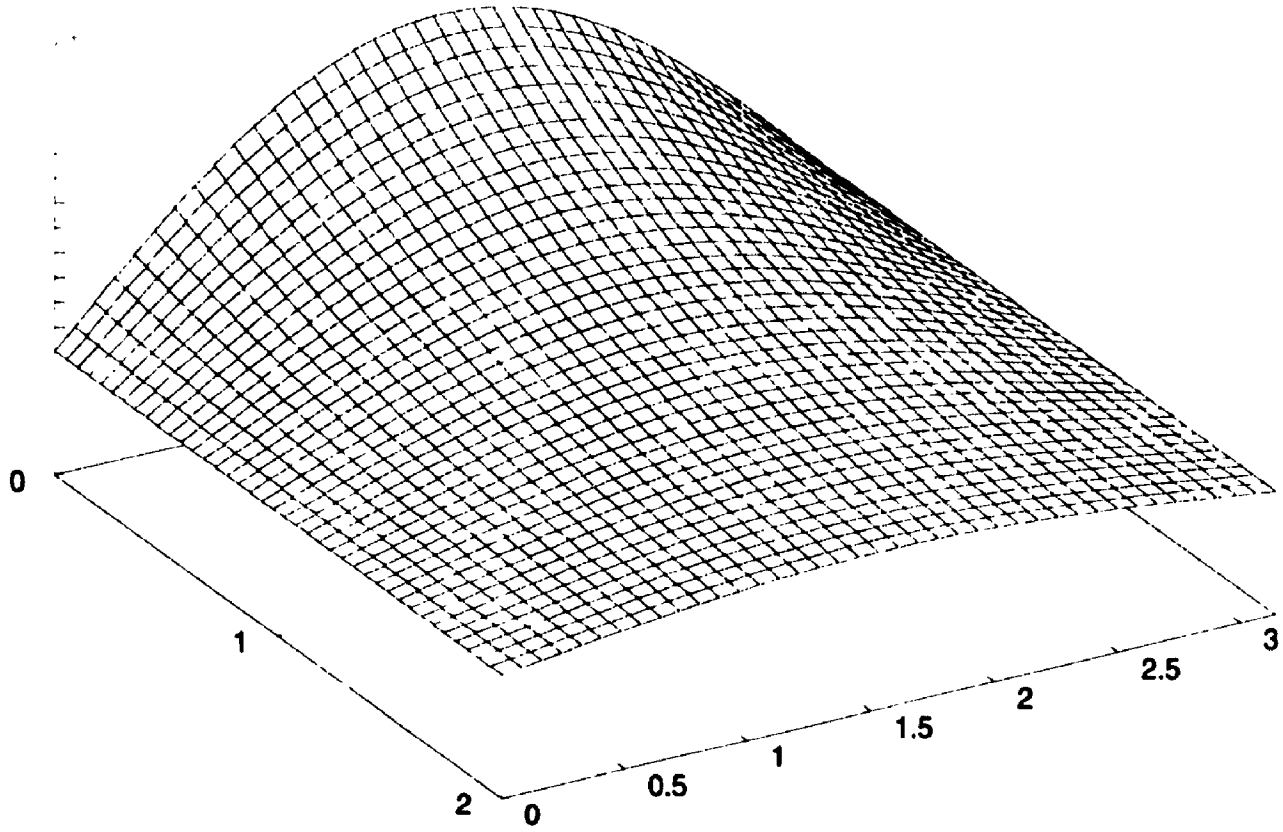

Figure 2-4. Schematic of the 1-D diffusion equation with homogeneous Dirichlet boundary conditions. The initial profile $u(x,0) = f(x)$ maps to a downstream profile given by $u(x,T) = \psi(x)$.

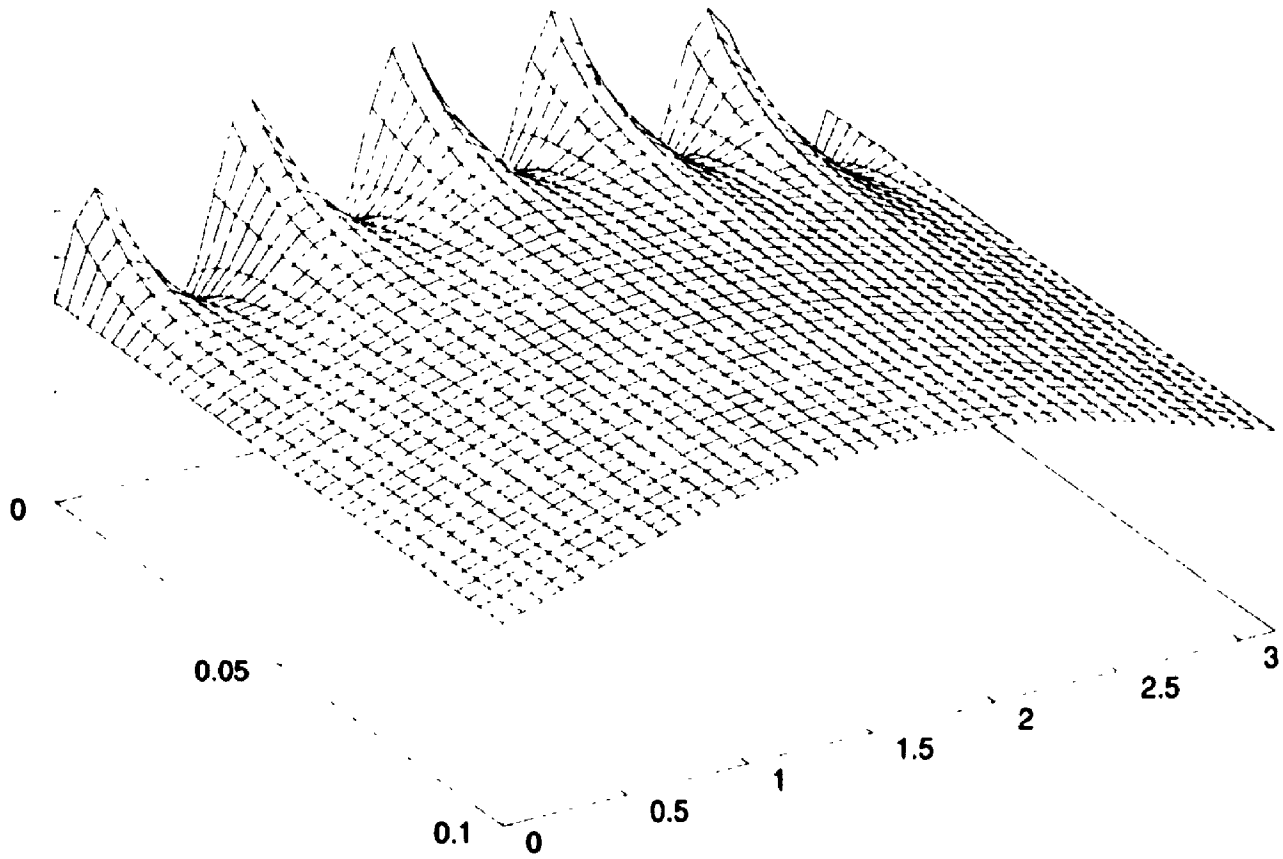

Figure 2-5. The 1-D diffusion equation with homogeneous Dirichlet boundary conditions for an initial profile $f(x) = \sin(x) + \sin(10x)$. The downstream profile at $T = 1$ shows the effects of diffusion removing the high frequency solutions from the system.

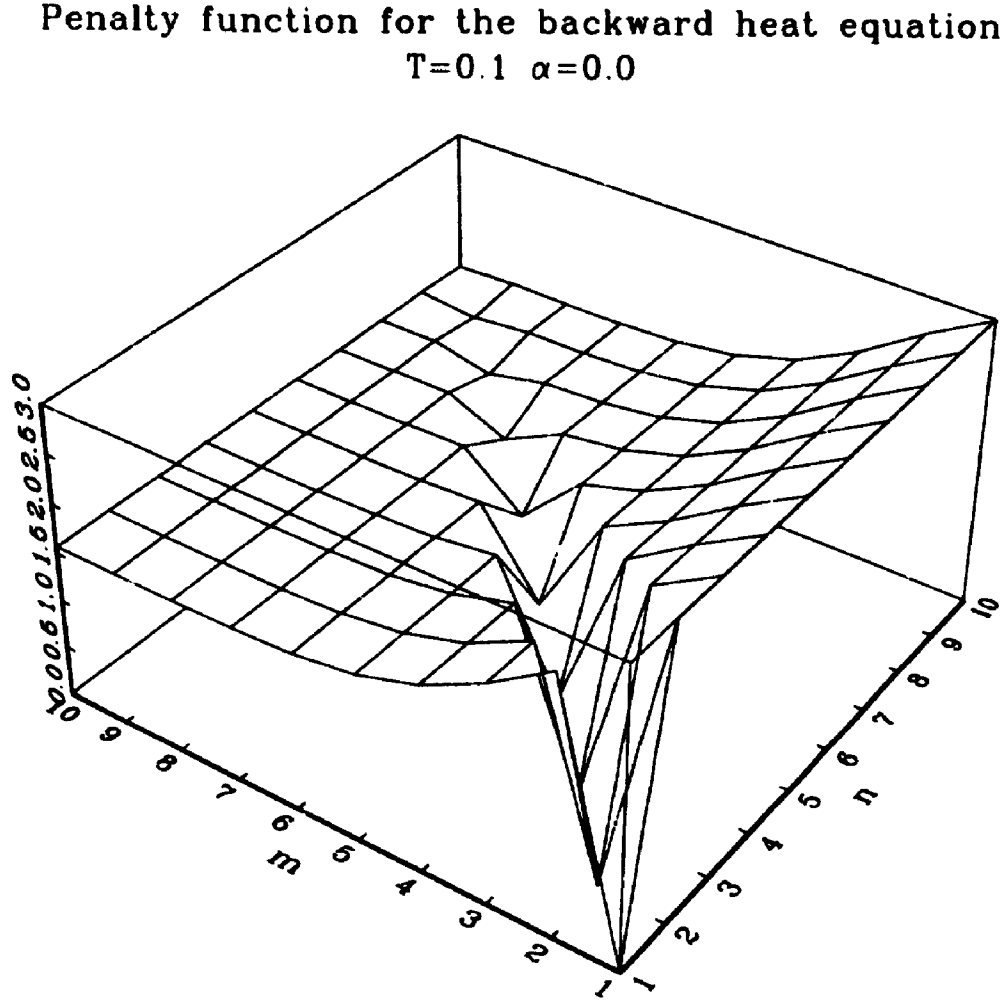

Figure 2-6. Penalty function surface for the backward heat equation with $T=0.1$. Given the data n, the quasi-solution $\tilde{m}$ lies at the point where the function surface is a minimum. The true solution lies along the diagonal $m=n$. The quasi-solution is defined as the locus of minimum points, but the minimum becomes indistinguishable for $n>6$.

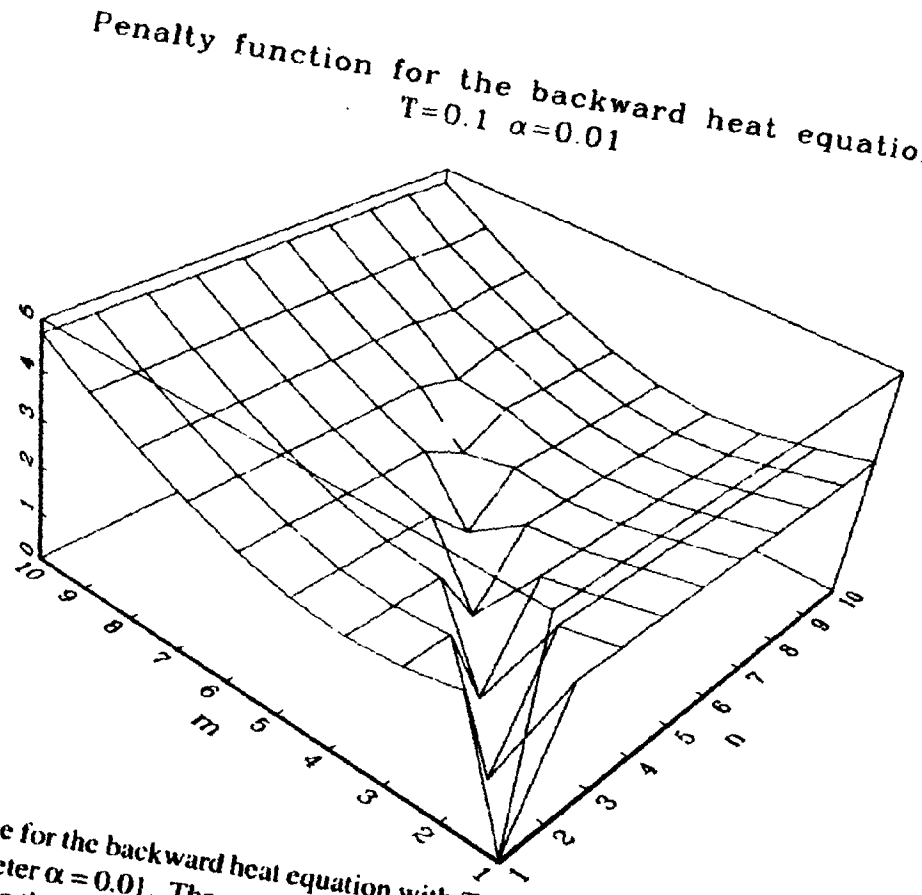

Figure 2-7. Penalty function surface for the backward heat equation with $T=0.1$ and regularization. The regularization term was defined as $\|\nabla f\|^2$ with regularization parameter $\alpha = 0.01$. The regularization permits stable solutions for all n. However, solutions lose accuracy for $n>7$. The true solution lies along the diagonal $m=n$.

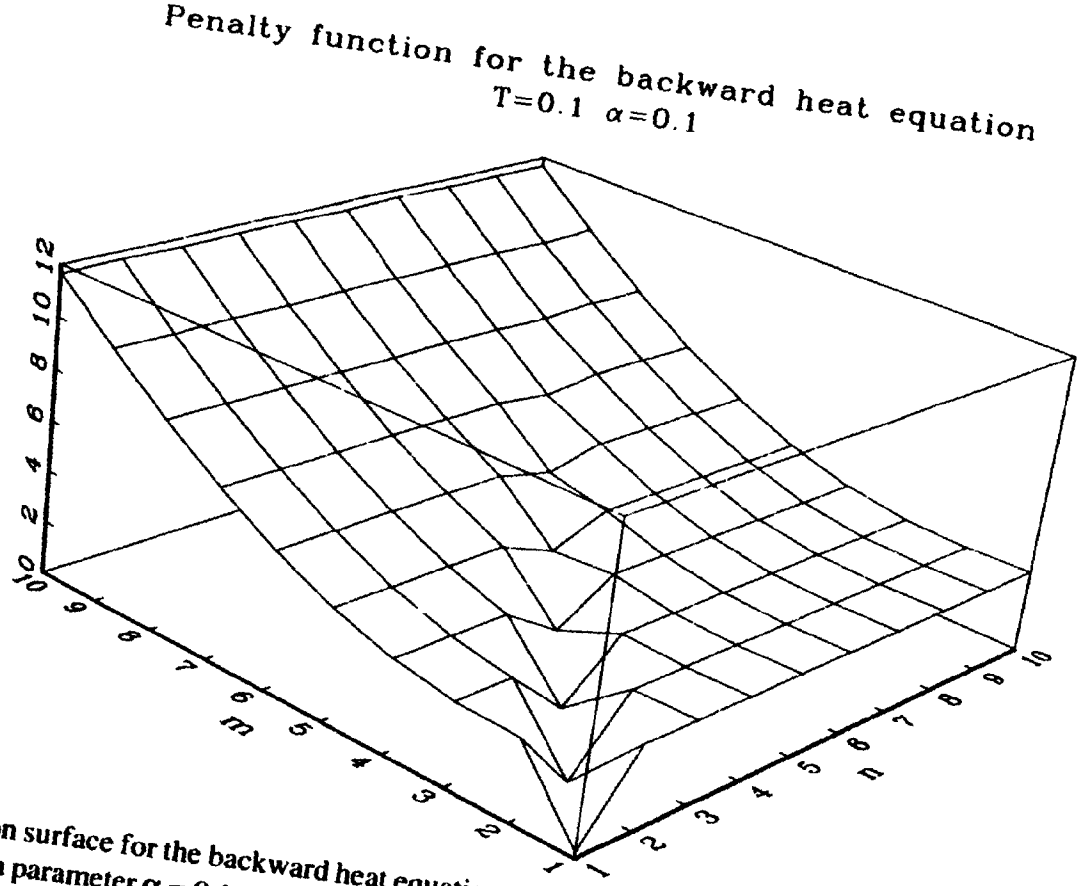

Figure 2-8. Penalty function surface for the backward heat equation with $T=0.1$ and regularization. The regularization term was defined as $\|\nabla f\|^2$ with regularization parameter $\alpha = 0.1$. Here the stronger regularization generates a more pronounced minimum but the solution lose accuracy for $n>5$. The true solution lies along the diagonal $m=n$.

CHAPTER 3

An Inverse Problem in Electromagnetic Prospecting

3.1 Introduction

Electromagnetic methods are used extensively in the field of mineral exploration. These techniques involve generating either a constant, sinusoidal or transient electromagnetic field and measuring the response caused by a buried conductive anomaly. The induced fields are then used to infer details of the conductivity structure of the subsurface. Electromagnetic techniques which utilize a constant current source (DC) are referred to as resistivity methods.

A common resistivity technique for surveying vein-type ore bodies is the mise-à-la-masse prospecting method which was pioneered by Schlumberger in the 1920's [44]. In this method, a constant current source is applied directly to the ore body, either through a drill hole which intersects the body or through an exposed outcropping. The current source is grounded at a large distance from the body to effectively isolate the source. Measurements of potential or potential gradient (electric field) are then made at numerous points on the surface to generate a 2-D response profile. Interpretation of the resultant surface fields represents a difficult inverse problem. The difficulty arises from the fact that the inverse operator is often highly non-linear, non-unique, and possesses a high degree of dimensionality. Discussion of the inverse problems associated with electromagnetic prospecting in geophysics can be found in [37].

Solution of the forward problem (i.e. knowing the conductive properties of the medium and solving for the surface fields) is achievable numerically. Suitable numerical solution techniques include finite differences [13], finite elements [36], or integral equation methods [16,54]. While these researchers consider full three dimensional models of the conductivity substructure, none attempt to solve the inverse problem; that is, recovering the conductivity structure through boundary measurements. Not only does the work presented here utilize a full 3D model, but successful inversion using the surface fields is achieved.

A class of reconstruction algorithms use the method of quasi-solutions which phrase the solution to an inverse problem in terms of a multidimensional cost function [14,40]. The cost function in this case is based on fitting the measured surface field data in a least squares sense. Using the chosen numerical forward solver, one could find an approximate solution to the inverse problem using a guess and improve method. The global minimum of the cost function now represents the best solution to the inverse problem. Finding the global minimum is a task ideally suited to the optimization technique, simulated annealing [1,6,12,31]. Inversions in geophysics have been attempted before using the simulated annealing technique. For example in [45], simulated annealing was used in the inversion of non-linear seismic soundings for a 1D earth model.

This chapter will formulate the mathematical model for the mise-à-la-masse prospecting technique. A numerical method using a finite difference approximation is proposed to solve this model. A least squares fit to the surface field is suggested as a suitable method to approximate the inverse problem including geophysically motivated assumptions which help regularize the problem. The value of the least squares fit is assigned to a cost function. The minimum value of the cost function is the best-fit of the surface fields and hence the best approximation to the inverse problem. The search for this best-fit is attempted with the use of simulated annealing. A proof of principle example using a synthetically generated data-set is furnished to validate the technique. Further work includes an example which incorporates the dimensions from a real-life vein-type ore body. Extensions to the model which investigate the effects of random data noise and conductive overburden are also considered.

3.2 Formulation

The mise-à-la-masse prospecting method can be modelled by the electrostatic problem of an electrode buried in an inhomogeneous infinite half-space. The conservation of electric charge dictates that the current density $\boldsymbol{J}$ satisfies

$$\nabla \cdot \boldsymbol{J} = 0, \tag{3.2.1}$$

when no charge flux is contained. In a linear isotropic medium, the relation between current density and electric field $\boldsymbol{E}$ is

(3.2.2) $$\boldsymbol{J} = \sigma \boldsymbol{E},$$

where σ is the conductance of the inhomogeneous medium. Let

(3.2.3) $$\sigma = \sigma(x, y, z),$$

be represented in rectangular coordinates, where z increases vertically downward (figure 3-1a). The electric field can be written in terms of a scalar potential ϕ as

(3.2.4) $$\boldsymbol{E} = \nabla\phi.$$

In terms of the scalar potential, (3.2.1) yields

(3.2.5) $$\nabla \cdot (\sigma \nabla \phi) = 0.$$

For a homogeneous conductivity field, σ would be constant and (3.2.5) reduces to Laplace's equation.

The boundary conditions consist of the potential field asymptotically approaching zero at infinity

(3.2.6*a*) $$\lim_{(x,y)\to\pm\infty} \phi(x, y, z) = 0,$$

and

(3.2.6*b*) $$\lim_{z\to+\infty} \phi(x, y, z) = 0.$$

The boundary condition at the surface arises from the continuity of $\boldsymbol{J}$ at the interface. At any interface, the normal component of the current density must be continuous. In terms of the electric field, this yields

(3.2.7) $$\hat{n} \cdot (\sigma_{air}\boldsymbol{J} \quad - \sigma_{ground}\boldsymbol{E}_{ground}) = 0.$$

Since the air layer is non-conductive (i.e. $\sigma_{air} = 0$), a no-flux condition is established on the surface given by

(3.2.8) $$\left.\frac{\partial \phi}{\partial z}\right|_{z=0} = 0.$$

The buried electrode is assumed to be maintained at a fixed potential. The corresponding boundary condition is

(3.2.9) $$\phi(0,0,L) = \phi_0,$$

where ϕ_0 is some constant.

In the mise-à-la-masse prospecting method, one attempts to reconstruct a buried conductive anomaly using either the potential or potential gradient (electric field) measured on the surface. The solution to this inverse problem is highly non-linear and most certainly non-unique. As is typical in the solution of inverse problems, certain assumptions must be made to regularize the problem [14,26,39]. That is, physical insight is applied to limit the set of solutions. For example, negative values of conductivity are not considered nor are values of conductivity which exceed that of known rock structures. In the proposed model, geophysical insight is used to construct the two following regularizing assumptions concerning the details of the ore body.

First, the ore body is assumed to be characterized by a high value of conductivity. Outside of the body, the conductivity is some lesser value. Both the ore body and the surrounding medium are assumed to be conductively homogeneous; both with conductivities constant and known. For vein type bodies a high conductivity contrast between ore bearing and non-ore bearing rock is common. A typical ratio of conductivities is on the order of 10^4:1 [36]. Hence, this conductivity ratio can be supplied as a parameter rather than found as a result of the calculation. This limits some of the degrees of freedom of the inversion; the algorithm is responsible for finding the extent of the ore body, not the conductivity of it. This assumption is similar to that found in [26] when incomplete boundary data is known.

Secondly, the shape of the ore body is assumed to be a rectangular prism with the buried source lying somewhere within this prism. This box-type structure is found commonly in modelling [13] as well as in practice [53]. The choice of a box structure provides an important uniqueness result. Theoretical results from [8] show that the solution for the potential problem for convex polyhedrons of constant conductivity is unique. Hence, two different high conductance boxes cannot produce the same external potential. It is interesting to note that a similar situation in 2-D does not hold. That is, two distinct polygons can be constructed that generate the same external potential [47].

The *box* of high conductance can be represented uniquely by 8 parameters; three values (x_0, y_0, z_0) denote the position of the box centre, three values (L_1, L_2, L_3) give the length of each box dimension and two parameters represent the dip and strike angles (γ, θ) (see figure 3-2). The dip angle is the angle between the box's L_1 axis and the xy-plane, while the strike angle represents the rotation about the z-axis. As is the practice in prospecting, these are the fundamental angles which describe an ore vein. Note that the range of the angles is only between -45° and 45°. This limited rotation is allowed by the fact that a box has constant conductivity. For example, no difference would be found between a unit cube and a unit cube rotated 90° about any axis perpendicular to a face. There is a possibility for a third angle which would describe the rotation about the x-axis, but this angle is generally ignored.

By using the forward solver, potential values $\phi = \phi(x, y, z)$ can be found for any box configuration. The electric field at the surface can then be calculated from

$$\boldsymbol{E}^c = \nabla\phi = \left(\frac{\partial\phi}{\partial x}(x, y, 0), \frac{\partial\phi}{\partial y}(x, y, 0), 0 \right), \tag{3.2.10}$$

where the superscript c denotes calculated field. Note that $E_z^c = 0$ from the no-flux boundary condition in (3.2.7). Now, one wishes to somehow assign a value of merit to any combination of the 8 box parameters. This *cost* value is based on how well the observed electric fields on the surface are approximated by the calculated electric fields. The minimum cost corresponds to the best approximation to the inverse problem.

A suitable cost function C is given by the least-squares difference between the observed electric field and the calculated electric field summed at points on the surface. That is

$$C = \| \boldsymbol{E}^m - \boldsymbol{E}^c \|^2 \text{ on } R, \tag{3.2.11}$$

which can be written

$$C = \sum_{(x,y)\in R} \sum \left[(E_x^m - E_x^c)^2 + (E_y^m - E_y^c)^2 \right], \tag{3.2.12}$$

where

$$\boldsymbol{E}^m = (E_x^m, E_y^m, 0), \tag{3.2.13}$$

is the observed electric field, and R represents a finite 2-dimensional region on the earth's surface where field measurements have been compiled (figure 3-3). The cost is a function of the 8 box parameters

(3.2.14) $$C = C(x_0, y_0, z_0, L_1, L_2, L_3, \gamma, \theta).$$

The *norm* type definition of C admits the following two properties: $C \geq 0$ and $C = 0$ if the reconstructed box is exactly the generating box. Now, the solution to the inverse problem becomes a search for the global minimum of the cost function.

An alternative formulation for the cost function of (3.2.11) using the surface potential ϕ rather than the potential gradient was also investigated. The new cost function is

(3.2.15) $$C = |\phi^m(x, y, 0) - \phi^c(x, y, 0)|^2 \text{ on } R.$$

The inversion results were similar using the cost calculation of (3.2.15) to that of (3.2.11) and hence are absent from discussion.

3.3 Numerical Procedure

3.3.1 Solution of the Forward Problem

The forward problem denotes the solution of (3.2.5) given the conductivity field of the inhomogeneous halfspace. The solution is attained numerically using a finite difference approximation for the derivatives on a 3-dimensional rectangular grid. A fixed potential was applied at the electrode.

Special consideration must be given to the remaining boundary conditions. The difficulty arises from the fact that the boundary conditions are prescribed at infinity which is impossible to facilitate given a finite grid. Fortunately, the asymptotic behaviour of the potential is

(3.3.1.1) $$\phi \sim 1/r,$$

where r is the distance from the source. Thus, cut-off lengths can be introduced where the potential, for practical purposes, will lose details of the near source conductivity structure and approach its asymptotic behaviour. The cut-off lengths were given in each dimension

by L_x, L_y, L_z thus defining a large finite box which encloses the conductive anomaly (figure 3-1b). If A is some constant, and

$$\phi = \frac{A}{r}, \tag{3.3.1.2}$$

then differentiation with respect to r yields [7]

$$\frac{\partial \phi}{\partial \hat{n}} = -\frac{A}{r^2}\hat{e}_r \cdot \hat{n}, \tag{3.3.1.3}$$

where $\hat{n}$ is the outward normal of any face of the cut-off box, and $\hat{e}_r$ is the unit radial vector. Using (3.3.1.2) in (3.3.1.3) gives

$$\frac{\partial \phi}{\partial \hat{n}} = -\frac{\cos(\beta)\phi}{r}, \tag{3.3.1.4}$$

where β is the angle between the unit radial vector and the normal vector to a face. The Dirichlet boundary condition at infinity in (3.2.6) is now approximated by the Robbin boundary condition of (3.3.1.4) at a finite distance from the electrode using the asymptotic behaviour of the potential. The only inherent length scale to the problem as opposed to the artificially imposed cut-off lengths is the depth of the electrode below the surface given by L. This value is used to scale all the length dimensions.

A non-uniform grid was implemented to assist with the boundary conditions at infinity. The aim is to choose a large domain size on whose fringe the boundary conditions can be imposed while still maintaining reasonable resolution in the centre. This task is accomplished by using a uniformly spaced rectangular grid nested within a non-uniformly spaced grid (see figure 3-3). The grid spacing in the non-uniform region was chosen to be exponentially increasing with

$$\Delta x_i = \Delta x_0 \exp\left(\frac{(i - Ni_u)}{\alpha_x}\right), \tag{3.3.1.5}$$

where Δx_0 is the uniform grid spacing, α_x a scaling constant, and Ni_u is the number of uniformly spaced points in the x-direction. A similar expression exists for the y and z directions. The rate of increase of the non-uniform spacing is not without restrictions. This

can be seen by examining the central finite difference formula for the 2nd derivative of a function, ϕ. The formula with uniform grid spacing Δx is given by

$$\phi''(x_i) = \frac{\phi(x_{i-1}) - 2\phi(x_i) + \phi(x_{i+1})}{\Delta x^2} + O(\Delta x^2). \tag{3.3.1.6}$$

The truncation error is 2nd order. However, the expression for non-uniformly spaced grid points is

$$\phi_i''(x_i) = \frac{\Delta x_i \phi(x_{i-1}) - 2\Delta\bar{x}\phi(x_i) + \Delta x_{i+1}\phi(x_{i+1})}{\Delta x_i \Delta x_{i+1}\Delta\bar{x}} + \frac{\phi'''(x_i)}{3}(\Delta x_i - \Delta x_{i+1}) + \frac{\phi^{(IV)}(x_i)}{12}(\Delta x_i^2 - \Delta x_i \Delta x_{i+1} + \Delta x_{i+1}^2) + \ldots, \tag{3.3.1.7}$$

where Δx_i is defined in (3.3.1.5), and $\Delta\bar{x} = (\Delta x_{i+1} + \Delta x_i)/2$. The grid spacing is no longer a constant but rather a function of i, the number of grid points from the source. Accordingly, the truncation error changes from 2nd order in the uniform case to something more complicated in the non-uniform case as demonstrated by the second term in (3.3.1.7). The error is a product of the third derivative of the potential with the rate at which the grid spacing increases. Far from the electrode one expects (3.3.1.2) to hold, implying that $\phi''' \sim 1/r^4$. The difference in grid spacing yields

$$\Delta x_i - \Delta x_{i+1} = \Delta x_0 \exp\left(\frac{i - Ni_u}{\alpha_x}\right)\left(1 - \exp\left(\frac{1}{\alpha_x}\right)\right), \tag{3.3.1.8}$$

which is a growing exponential. The task is to choose a reasonably large α_x such that the truncation error in (3.3.1.7) is kept sufficiently small. One can easily verify that as $\alpha_x \to \infty$, the grid spacing $\Delta x_i \to \Delta x_0$ and hence the truncation error returns to 2nd order.

The finite-difference discretization is performed on the non-homogeneous Laplace's equation of (3.2.5). Expanding (3.2.5) for Cartesian coordinates yields

$$\frac{\partial}{\partial x}\left(\sigma\frac{\partial\phi}{\partial x}\right) + \frac{\partial}{\partial y}\left(\sigma\frac{\partial\phi}{\partial y}\right) + \frac{\partial}{\partial z}\left(\sigma\frac{\partial\phi}{\partial z}\right) = 0. \tag{3.3.1.9}$$

The first term in (3.3.1.9) can be discretized for node (i,j,k) using a central difference formula, such as

(3.3.1.10)
$$\frac{\partial}{\partial x}\left(\sigma\frac{\partial\phi}{\partial x}\right)_{i,j,k}=\frac{1}{2\Delta\bar{x}}\left(\frac{\Delta x_i}{\Delta x_{i+1}}\right)\left(\sigma\frac{\partial\phi}{\partial x}\right)_{i+\frac{1}{2},j,k}$$
$$+\frac{\Delta\tilde{x}\Delta\bar{x}}{\Delta x_i\Delta x_{i+1}}\left(\sigma\frac{\partial\phi}{\partial x}\right)_{i,j,k}-\frac{1}{2\Delta\bar{x}}\left(\frac{\Delta x_{i+1}}{\Delta x_i}\right)\left(\sigma\frac{\partial\phi}{\partial x}\right)_{i-\frac{1}{2},j,k},$$

where $\Delta\bar{x}$ is the average grid spacing as above, and $\Delta\tilde{x}=\Delta x_{i+1}-\Delta x_i$ is the difference between grid spacing. The value of the conductivity σ at the midpoint is chosen to be the average value

(3.3.1.11)
$$\sigma_{i+\frac{1}{2},j,k}=\frac{\sigma_{i+1,j,k}+\sigma_{i,j,k}}{2}.$$

The derivatives at the midpoints in (3.3.1.10) can be expanded in terms of the central difference formula to give

(3.3.1.12*a*)
$$\left(\sigma\frac{\partial\phi}{\partial x}\right)_{i+\frac{1}{2},j,k}=\sigma_{i+\frac{1}{2},j,k}\left(\frac{\phi_{i+1}-\phi_i}{\Delta x_{i+1}}\right)$$

(3.3.1.12*b*)
$$\left(\sigma\frac{\partial\phi}{\partial x}\right)_{i-\frac{1}{2},j,k}=\sigma_{i-\frac{1}{2},j,k}\left(\frac{\phi_i-\phi_{i-1}}{\Delta x_i}\right)$$

(3.3.1.12*c*)
$$\left(\sigma\frac{\partial\phi}{\partial x}\right)_{i,j,k}=\sigma_{i,j,k}\left\{\frac{(\Delta x_i)^2\phi_{i+1,j,k}+2\Delta\tilde{x}\Delta\bar{x}\phi_{i,j,k}-(\Delta x_{i+1})^2\phi_{i-1,j,k}}{2\Delta x_i\Delta x_{i+1}\Delta\bar{x}}\right\}.$$

The terms in (3.3.1.12) can be substituted into (3.3.1.10) to give the complete expression for the x derivative. This process can be repeated for the y and z derivatives to give the complete discretized equation for (3.3.1.9). For a uniform grid spacing, $\Delta\tilde{x}=0$, which means that equation (3.3.1.12c) would not appear in (3.3.1.10).

The finite-difference discretization generates a linear system of $N_i \cdot N_j \cdot N_k$ simultaneous algebraic equations

(3.3.1.13)
$$\mathbf{A}\phi=\boldsymbol{b}$$

where N_i, N_j, N_k represent the number of grid points in each of the respective (x,y,z) coordinate directions. One can easily see that the size of the linear system in (3.3.2.13) increases as a cubic which demonstrates the difficulty of modelling in 3-D. However, the matrix **A** has at most 7 entries in any row allowing the use of sparse matrix techniques. The sparse matrix

solver used was *Mat1* which utilizes the Yale sparse matrix storage technique. *Mat1* is an iterative solver that implements an Orthomin acceleration technique as well as an incomplete factorization to approximate the solution of a linear system of equations [18].

Analytic solutions of (3.2.5) [50] often represent the buried source as a delta function, which is impossible to represent exactly using numerical techniques. To validate the numerical results, the asymptotic behaviour of the computed potential was examined for the case of a surface electrode on a homogeneous halfspace. Assuming a solution of the form

(3.3.1.14) $$\phi = A r^{b}$$

and taking logarithms yields

(3.3.1.15) $$\ln(\phi) = \ln(A) + b \ln(r).$$

If (3.3.1.2) is true, one expects the value of b to be constant and equal to -1. This relationship can be seen in figure 3-4 for the Robbin and Dirichlet boundary conditions. The value of b is calculated by a linear regression fit of (3.3.1.15) using the value of ϕ at all grid points. The length scale L_x represents the outer edge of the computational domain where the boundary conditions are applied. The model was run with equal lengths in all the coordinate directions implying that $L_y = L_x$ and $L_z = L_x$. The value of b computed for Dirichlet boundary conditions improves as the size of the computational domain is increased. The value for Robbin boundary conditions, however, is exactly -1, independent of the domain size.

3.3.2 Solution of the Inverse Problem

The cost function is an 8-dimensional multimodal scalar function. One possible technique to find the global minimum is to calculate the cost for all possible configurations and choose the smallest value calculated. This type of brute force solution is possible theoretically, but impractical given finite computing time and resources.

Cross-sections of the cost function verify its multimodal nature (figure 3-5). While some dimensions show C to be strongly unimodal, other dimensions contain several local minima. It is for this reason that the simulated annealing algorithm is used to perform the minimization.

The current state of the system is given by the 8 box parameters described in figure 3-2. The random changes consist of perturbing one of these 8 box parameters. Choosing the magnitude of this perturbation raises a difficult question. Each of the parameters is real valued and hence can assume a continuum of values. In the present example, choosing a new configuration is fairly straightforward. A change of less than one grid spacing fails to change the finite difference linearization of (3.3.1.9) since the conductivity is stored only at discrete grid points. Accordingly, the potential field will remain unchanged leaving the cost function the same. An appropriate magnitude for any perturbation is then given by the grid spacing for each dimension. A smaller change would go unnoticed while a larger change would skip intermediate configurations. A perturbation for parameters in the x-direction would be $x_0 \pm \Delta x_0$ and $L_1 \pm \Delta x_0$. Similarly, the changes in the y and z directions are $y_0 \pm \Delta y_0$, $L_2 \pm \Delta y_0$ and $z_0 \pm \Delta z_0$, $L_3 \pm \Delta z_0$, respectively. A natural increment does not exist for the dip and strike angles. A perturbation of $\gamma \pm 5°$ and $\theta \pm 5°$ was found to give acceptable resolution as well as providing changes of reasonable magnitude. Thus, at each step an increase or decrease of one of the 8 box parameters yields a maximum of 16 possible choices to construct a new configuration.

The temperature parameter T is assigned an initial value greater than the average change in the cost function for any particular random configuration change. This is commonly referred to as the *melting* temperature. This initial temperature should be high enough so that the algorithm can choose any state in the solution domain, similar to a molecule being allowed to move throughout a liquid. Randomly selected configuration changes are performed at a particular temperature level until some maximum number are attempted or until a preset limit of successful reconfigurations is achieved. Then the temperature T is reduced by 20%, and the process is repeated until no successful changes occur. The temperature at the kth level is

$$T_k = (0.80)^k T_0, \tag{3.3.2.1}$$

where T_0 is the initial temperature. By performing the cooling sufficiently slowly, the system can settle into its *crystalline* state (global minimum cost). When no more changes are accepted, it is assumed that the minimum cost is reached and the reconstruction of the high conductance box is complete.

The annealing process continues until one of the following two stopping conditions is met: 1) the minimum value of the cost function is found, or 2) continuous perturbations of the system produce no acceptances and hence no new configurations are generated.

The first criterion assumes that the theoretical minimum is known, which is not always the case. Of course, with the synthetic noise-free data, the minimum cost that can be achieved is C=0 (figure 3-8a). This fact determines exactly when to stop. With the introduction of noisy data, however, the global minimum is some unknown value greater than zero (figure 3-8b). The second criterion is usually gauged in terms of the ratio of acceptances to perturbation attempts. A suitable stopping condition is satisfied if this ratio is less than 10%. Fortunately, the current model possesses a finite number of state changes (16 in total). This property simplifies the second stopping criterion. Extensive searching at the low temperature levels of annealing is not necessary since there are only a finite number of changes to the configuration possible. If all 16 changes are tried and rejected, then a minimum is assumed, and further searching is pointless. It is true that this minimum may be local, but a careful choice of the annealing schedule will guarantee that it is a global minimum.

3.4 Validation

Testing of the reconstruction algorithm was done using synthetically generated data. The *synthetic* data set is created in the following manner. A set of 8 box parameters (Table 3-1) was chosen to run through the forward solver. The resulting solution ϕ was used to find the electric field measurements on the surface. These values were regarded as the experimentally measured values which the algorithm was attempting to recover. There are two pieces of information one can exploit from this synthetic data: 1) the generating conductivity structure is known, and 2) the global minimum is guaranteed to be zero. The latter fact is a result of the cost function being non-negative and the linear system in (3.3.1.9) having a unique solution.

(x_0, y_0, z_0)	(L_1, L_2, L_3)	Dip and Strike
(-0.375,0.25,1.0)	(1.75,1.0,0.5)	$\gamma = 30°, \theta = -30°$

Table 3-1. Box parameters for synthetically generated data set.

Reconstruction of the original configuration proceeded by choosing an initial guess box and then applying the Metropolis algorithm. The initial guess was chosen to be a unit cube with zero dip and strike angles (see figure 3-6). Solving for the guess box and calculating the cost function yields an initial cost of $C = 90.23$. The simulated annealing algorithm is then allowed to perturb this initial configuration and accept or reject new guesses accordingly. The entire annealing process requires 438 iterations (Table 3-2) to successfully reconstruct the correct box. Of these attempted perturbations 233 changes were accepted.

Noise	Minimum Cost		Re-configurations		Reconstructed Box		
(%)	Best	Final	Accept	Attempt	(x_0, y_0, z_0)	(L_1, L_2, L_3)	(γ, θ)
0	0	0	233	438	(-.375,.25,1.0)	(1.75,1.0,0.5)	(30°,-30°)
10	2.55	2.55	253	671	(-.375,.25,1.0)	(1.75,1.0,0.5)	(30°,-30°)
30	22.87	22.86	314	1111	(-.5,.25,1.0)	(2.0.1.0,0.5)	(30°,-35°)
35	40.2	40.1	1893	3472	(-0.5,0.25,0.93)	(1.5,1.0,0.625)	(30°,-30°)
40	50.4	50.4	3345	9004	(-.375,0.25,1.0)	(1.75,1.0,0.5)	(30°,-30°)
50	82.7	-	∞	∞	-	-	-

Table 3-2. Performance of the annealing reconstruction with uniformly distributed random noise added to the surface field data

In any real world experiment, errors, whether measurement or otherwise, will be present. The merit of an inversion scheme relies upon its ability to deal with random noise in the data. Uniformly distributed random noise was added to the synthetically generated data set to test the inversion scheme's robustness. To add N% noise to a measurement M, the formula used is

$$M_{noise} = \left(1 \pm \frac{N}{100} \cdot U[0,1)\right) \cdot M, \tag{3.4.1}$$

where $U[0,1)$ represents a uniformly distributed random number between 0 and 1. The effect of 40% random noise added to the surface signal can be seen in figure 3-7. Inversion results with the noisy data can be seen in Table 3-2. Note that the known minimum cost is no longer zero. The known minimum value is calculated by substituting the synthetic data and the synthetic data with noise in the cost formula (3.2.11). This new minimum cost should represent the cost when the reconstruction is complete. The inversion worked with

up to 40% random noise added. The solution effort, however, increases dramatically with the addition of noise. The number of iterations required by the simulated annealing search increases by an order of magnitude from 0% noise to 35% noise. This can be attributed to the blurring of the global minimum of the cost function when noise is added as sketched in figure 3-8b. In fact, the actual minimum achieved in the 35% noise case is lower than the minimum cost value expected. This phenomenon represents the theoretical breakdown of the inversion scheme. If the cost value for the true answer is not the global minimum, then the simulated annealing search will be unable to locate the conductivity structure which generated the data in the first place. For 50% random noise, the annealing search failed to converge to a global minimum.

3.5 Further Results

The reconstruction method was further tested using synthetically generated data that represents a real-life ore body. The dimensions for this test configuration were extracted from a vein type body found on the Cavendish Geophysical test range [53]. The test range consists of an extensively surveyed hard rock site. It was established in 1967 and is used for the testing and evaluation of electromagnetic prospecting techniques. The tests conducted include airborne and ground based EM surveys, as well as a comprehensive diamond drilling program. The drilling program involved removing core samples which were classified as to type of rock and minerals present. Metals found included Cu, Pb, Ni, and Sn in sulphide type deposits. The dimensions used were that of the *Zone A* body which lies 3m below the surface and is the shape of a rectangular slab 200m by 20m by 3m. These dimensions were non-dimensionalized using the drill hole depth L=8.9m. Borehole resistivity measurements conducted in [36] measured the conductivity of the ore body and the surrounding ground. This ratio was approximately 10,000 to 1. The sharp conductivity contrast, however, proved difficult for the numerical solver. Hence, a conductivity ratio of 100 to 1 was used. This ratio will provide similar results.

The initial box parameters for the Cavendish Zone A body can be seen in table 3-3 while the details of the recovery can be seen in table 3-4. The inversion achieved a lowest cost corresponding to C=33.1 starting from an initial cost value of C=1003.0. The non-zero

(x_0, y_0, z_0)	(L_1, L_2, L_3)	Dip and Strike
(0.25,1.08,1.50)	(0.38,15.18,2.5)	$\gamma = -20°, \theta = 20°$

Table 3-3. Box parameters for the synthetically generated data set modelled after the Zone A ore body found at the Cavendish Geophysical Test Range. The hole depth L=8.9m was used to non-dimensionalize all the distance measurements.

lowest cost is not a shortcoming of the minimization algorithm, but rather a limitation of the coarseness of the finite difference mesh. A large grid spacing in the y-direction, $\Delta y = 0.5$, was required in order to fit this dimension within the domain. This coarseness makes exact recovery impossible. Most importantly, the dip and strike angles are in the correct direction and are close in magnitude.

Minimum Cost		Re-configurations		Reconstructed Box		
Known	Final	Accepted	Attempted	(x_0, y_0, z_0)	(L_1, L_2, L_3)	(γ, θ)
0	33.1	258	597	(0.5,0.0,2.0)	(0.5,15.0,1.75)	(-30°,20°)

Table 3-4. Recovery of ore body for dimensions from the Cavendish Geophysical test range.

The Cavendish Zone A ore body dimensions were also used to test inversion in the presence of a thin conductive layer near the surface. This layer is known as conductive overburden. The higher conductivity found in an overburden layer is a result of moisture and dissolved salts lying in the soil above the bedrock. The effect of this layer is to partially shield the electrical response of the buried ore body and thereby reduce the magnitude of the electric fields measured on the surface. The overburden was given a conductivity ratio relative to the background of $\sigma_{over}/\sigma_{b} = 10$ and a scaled thickness $L/4$. This thickness corresponds to a layer approximately 2m thick. The results of the inversion with this conductive layer can be seen in Table 3-5 as well as results with a conductive layer twice as thick (ie. $L/2$).

The conductive overburden does not seriously effect the length and width recovery of the inversion algorithm, but it does seriously effect the resolving power in the z-direction. Determination of the width and length of the conductive anomaly relies on the location and magnitude of the peaks of the surface fields. The recovery of the depth information depends on the complete structure of the surface fields over a large area on the surface. The smoothing

Layer Thickness	Minimum Cost		Re-configurations		Reconstructed Box		
	Known	Final	Accepted	Attempts	(x_0, y_0, z_0)	(L_1, L_2, L_3)	(γ, θ)
$L/4$	0	25.67	245	587	(-0.25,1.0,1.75)	(0.5,15.5,1.25)	(-20°,20°)
$L/2$	0	16.54	325	888	(0.0,0.5,2.0)	(0.5,15.0,1.75)	(-30°,20°)

Table 3-5. Recovery of ore body for dimensions from the Cavendish Geophysical test range with a thin layer of conductive overburden lying on the surface. The layer of overburden was chosen to have a conductivity ratio $\sigma_{ovr}/\sigma_{b} = 10$.

of the signal on the surface is more pronounced with a highly conductive layer near the surface as is demonstrated by comparing figure 3-9a and figure 3-9b. This smoothing makes the recovery of the depth information difficult. Most importantly, the dip and strike angles are recovered exactly in the case of a layer of thickness $L/4$. Hence, the proposed inversion schemes works reasonably well in the presence of a conductive overburden.

3.6 Discussion

A full 3-dimensional model of the mise-à-la-masse prospecting method is developed. A finite difference approximation is used to solve the electrostatic potential numerically when given the conductivity field. By making regularizing assumptions pertaining to the conductivity sub-structure, the inverse problem is converted to a search for the global minimum of an 8-dimensional scalar cost function. This idea proves successful with a simple synthetic noise-free data set.

A more difficult reconstruction occurs when uniformly generated random noise is added to the surface field data. Here, the simulated annealing minimization requires more iterations to find the global minimum as the amount of noise is increased. The algorithm is successful with up to 40% random noise added to the data. The theoretical breakdown of the method begins to occur beyond 40% noise. This means that the global minimum of the cost function corresponds to a conductivity structure which is not necessarily the generating conductivity structure. Hints of this breakdown can be seen in the 35% noise case, but these false minimums are still close to the correct answer. With 50% random noise, the search for a global minimum failed outright.

A realistic ore body reconstruction is successfully completed using dimensions from the Cavendish Geophysical Test Range. Further extensions to the model included inversion in the presence of a conductive overburden. A reconstruction using experimentally measured field data would be the next logical step.

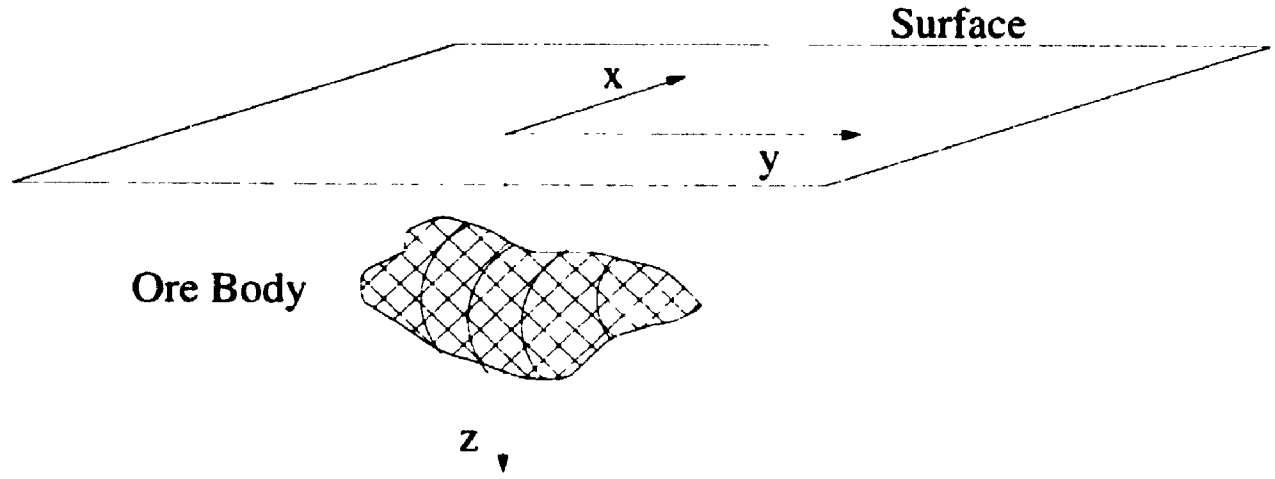

a)

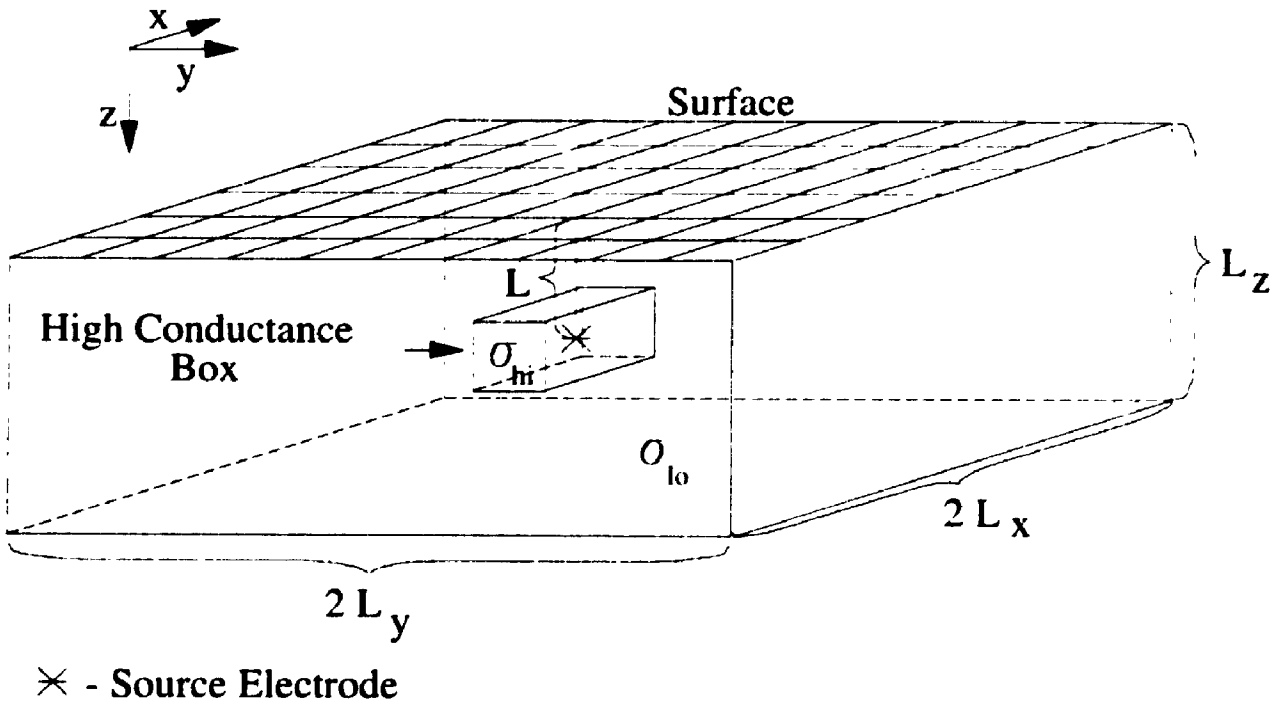

✳ - Source Electrode

b)

Figure 3-1. a) Coordinate system used for mise-à-la-masse model. The z-direction points vertically downward into the earth. b) The idealized ore body with length scales shown. The source electrode lies buried within the ore body at the position (0,0,L). A finite region *R* is defined on the surface where the surface field measurements are compiled

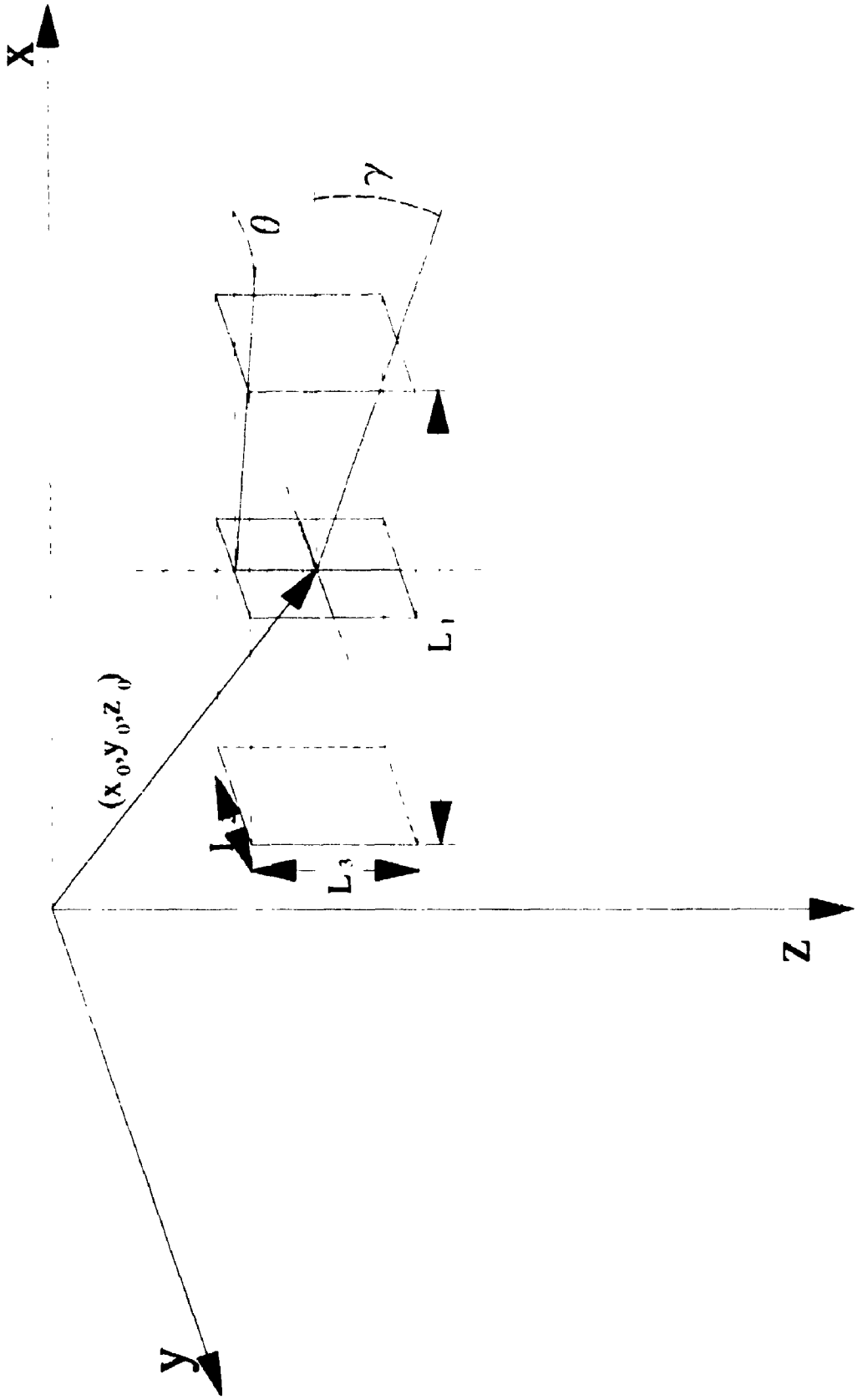

Figure 3-2. Sketch of the high conductance *box* detailing the 8 parameters used. The centre of the box is given by (x_0, y_0, z_0), while the length of the sides are (L_1, L_2, L_3). The angle γ denotes the dip angle, and θ is the strike angle. Within the box, the conductivity is σ_H. Outside the box, the conductivity is σ_H.

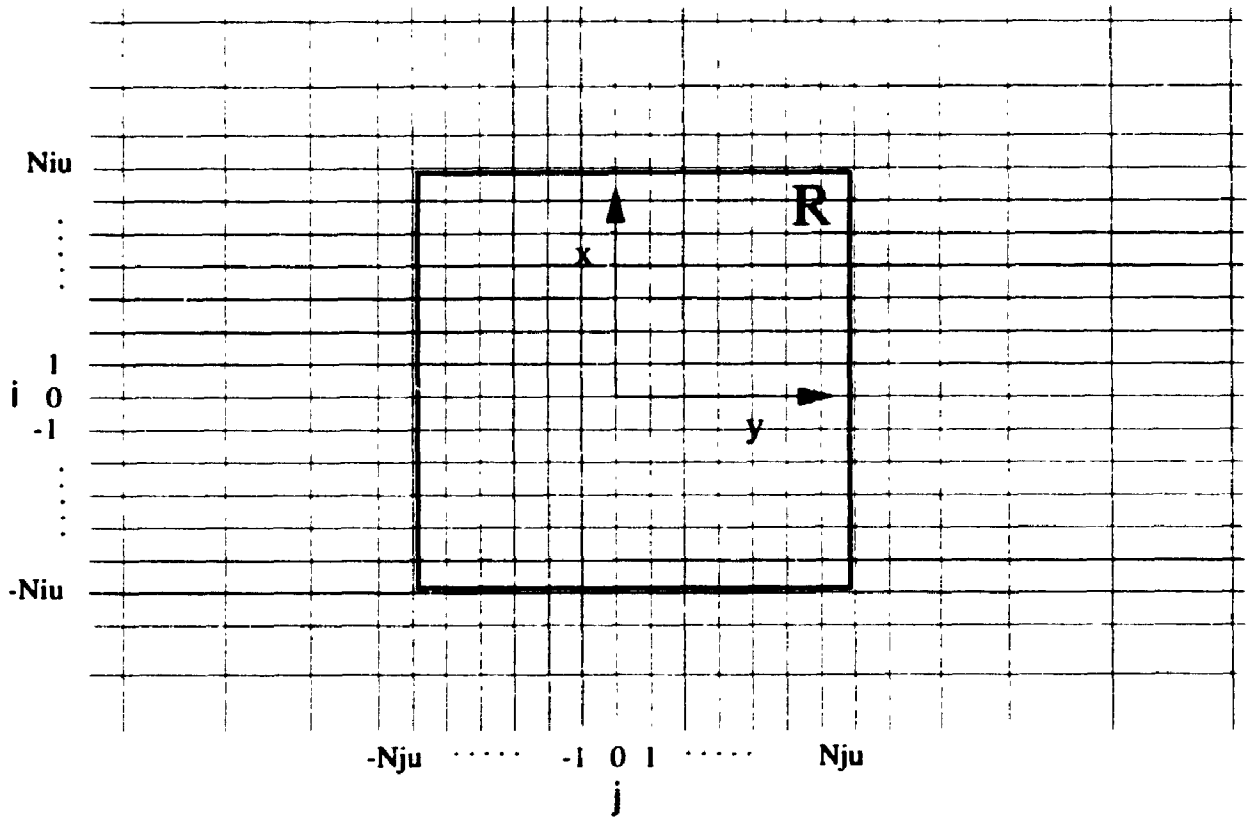

Figure 3-3. Diagram of the grid used for the finite-difference discretization. Within the region *R*, uniform grid spacing is used. Outside this region, a non-uniformly spaced grid is used.

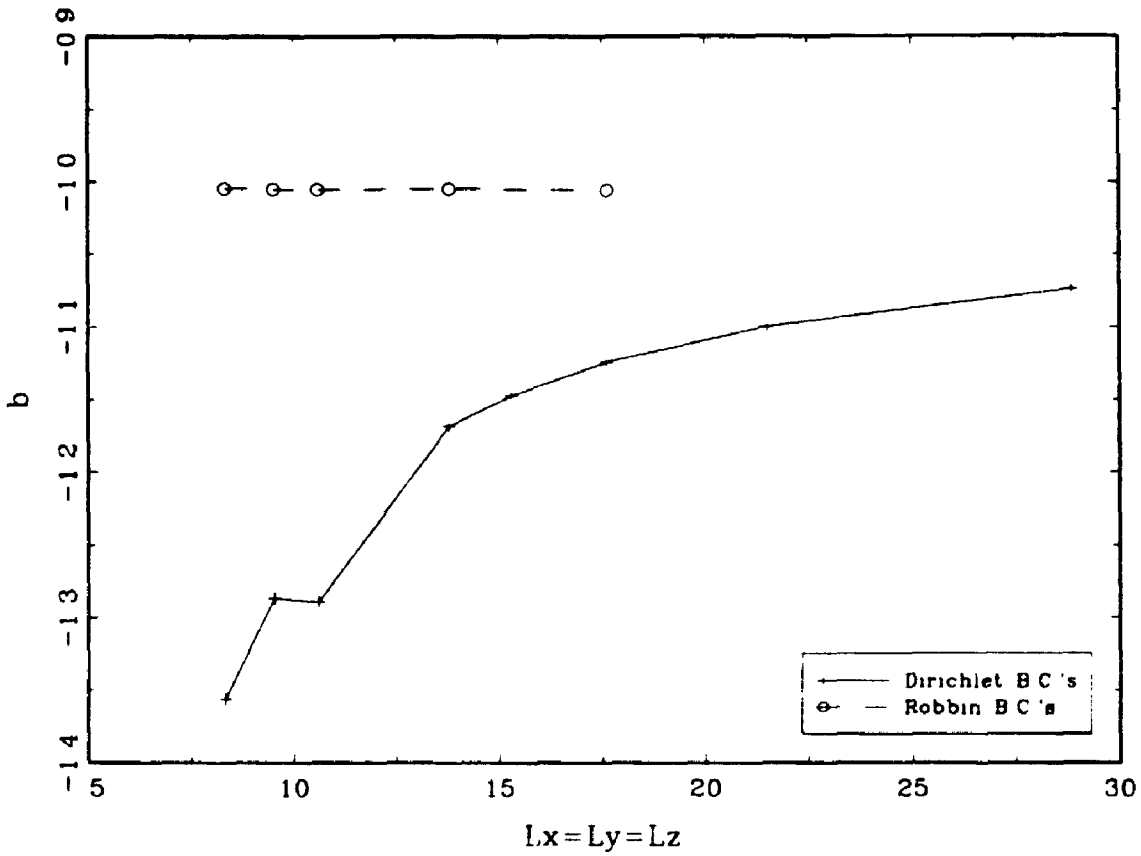

Figure 3-4. Plot of b vs. L_x for the numerical solution of a surface electrode and a conductively homogeneous earth for both Dirichlet and Robbin boundary conditions. The variable b is the slope of the linear regression of $\ln(\phi) = \ln(A) + b \ln(r)$, where ϕ is the potential and A is a constant. The variable r is the distance from the source electrode, and L_x is the size of the finite domain in the x direction.

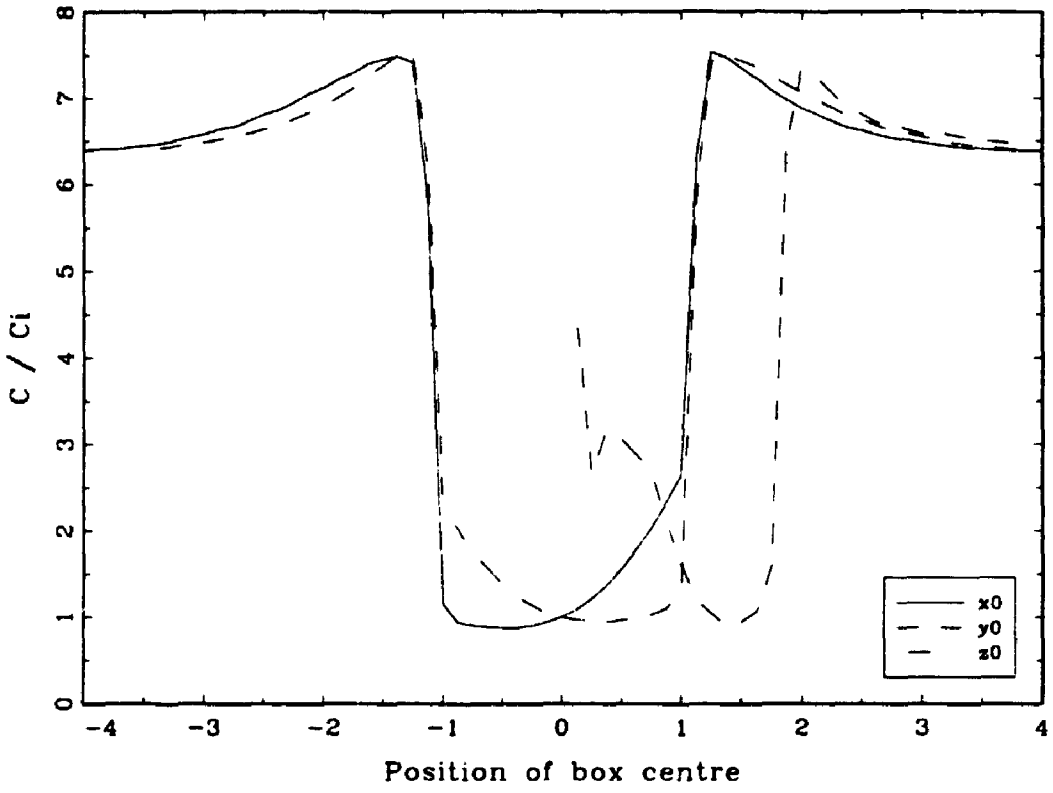

Figure 3-5a)

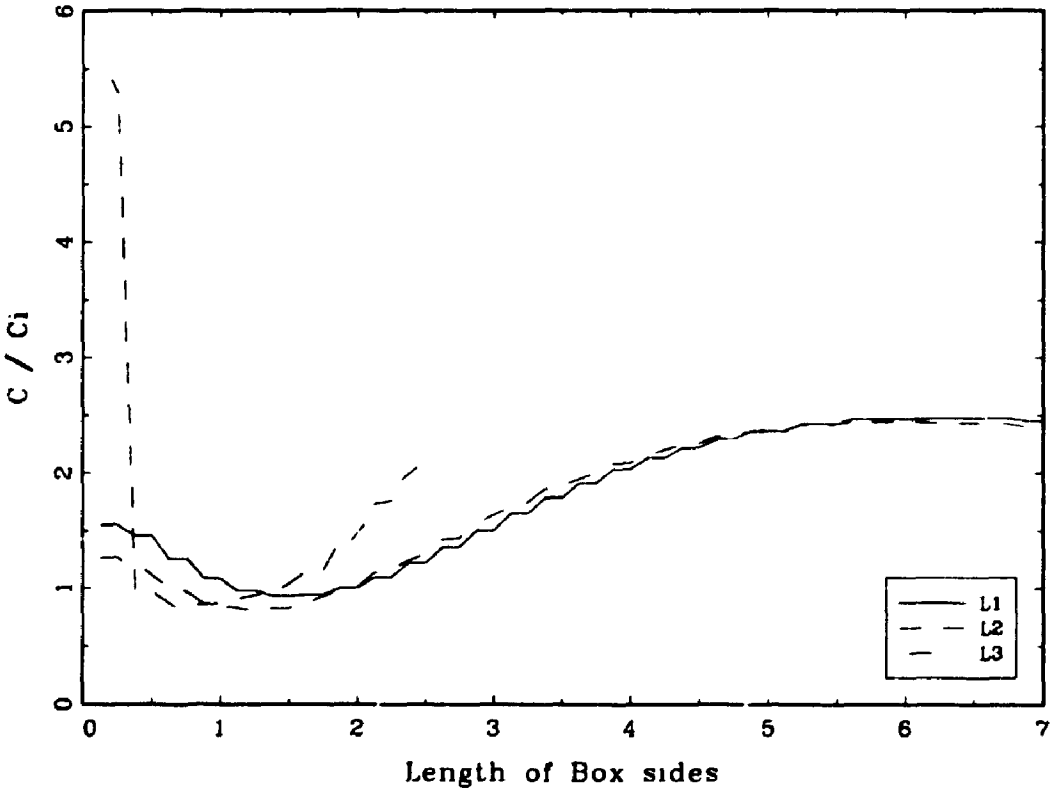

Figure 3-5b)

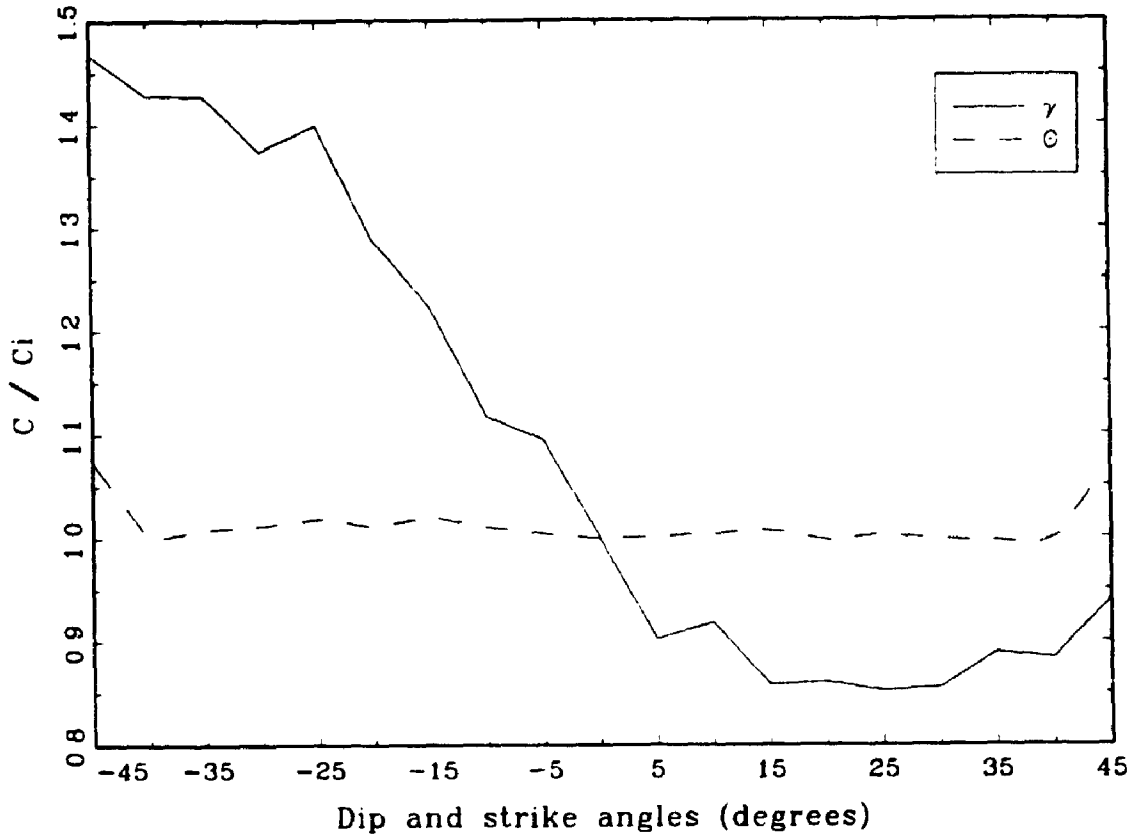

Figure 3-5c)

Figure 3-5. Plot of initial profiles of the cost function vs. its parameters a) (x_0, y_0, z_0), b) (L_1, L_2, L_3) and c) (γ, θ). The cost function is normalized by its initial value C_i.

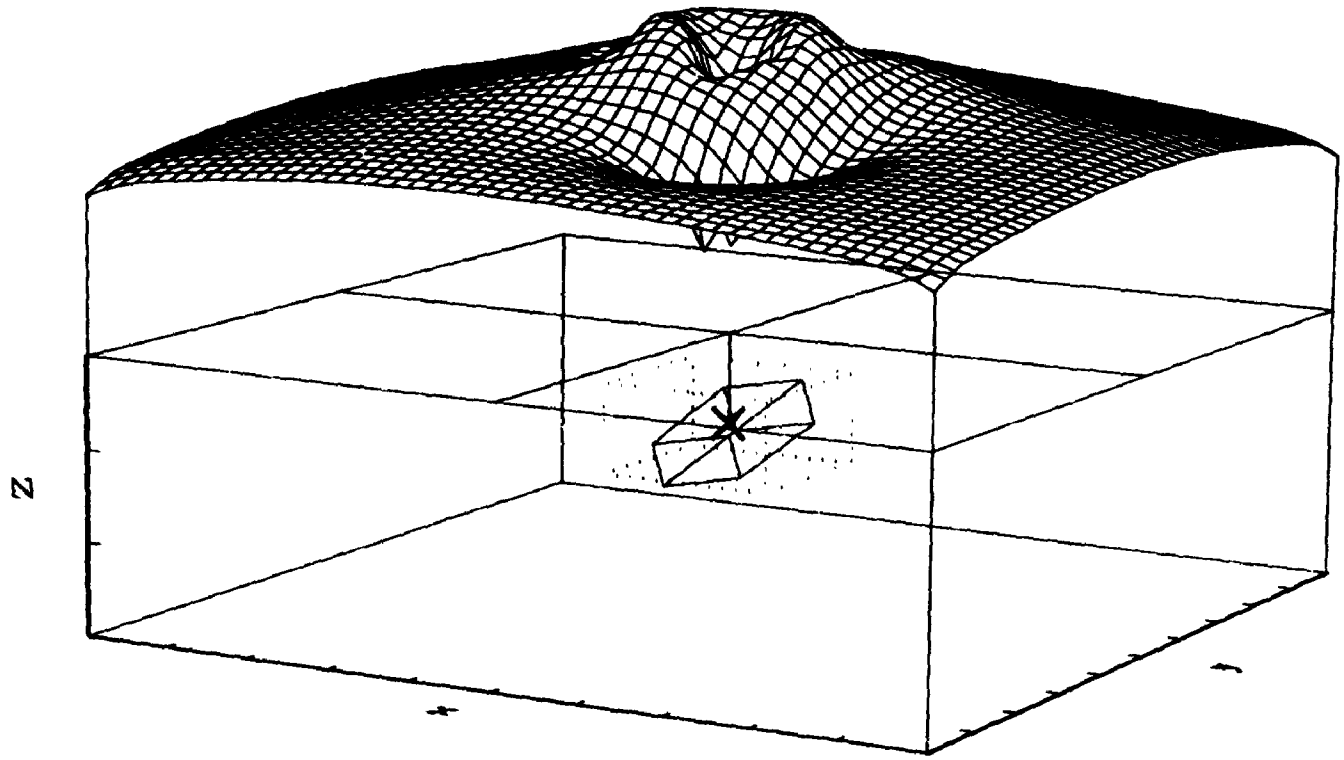

Figure 3-6. Plot of the high conductance box used to generate the noiseless synthetic data as well as the initial guess box used to start the annealing. The *X* marks the electrode in contact with the true high conductance box (solid line). The dashed box represents the initial guess box used to start the annealing recovery. The surface represents the cost function *C* at each grid point. These points are summed to give an initial cost value *C*=90.23.

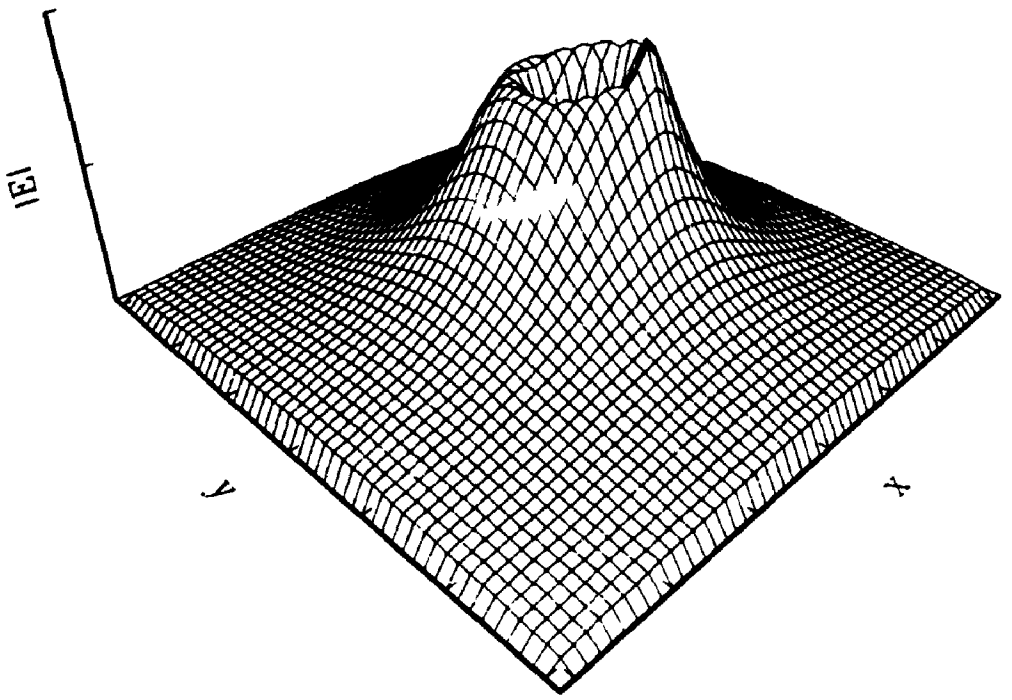

a)

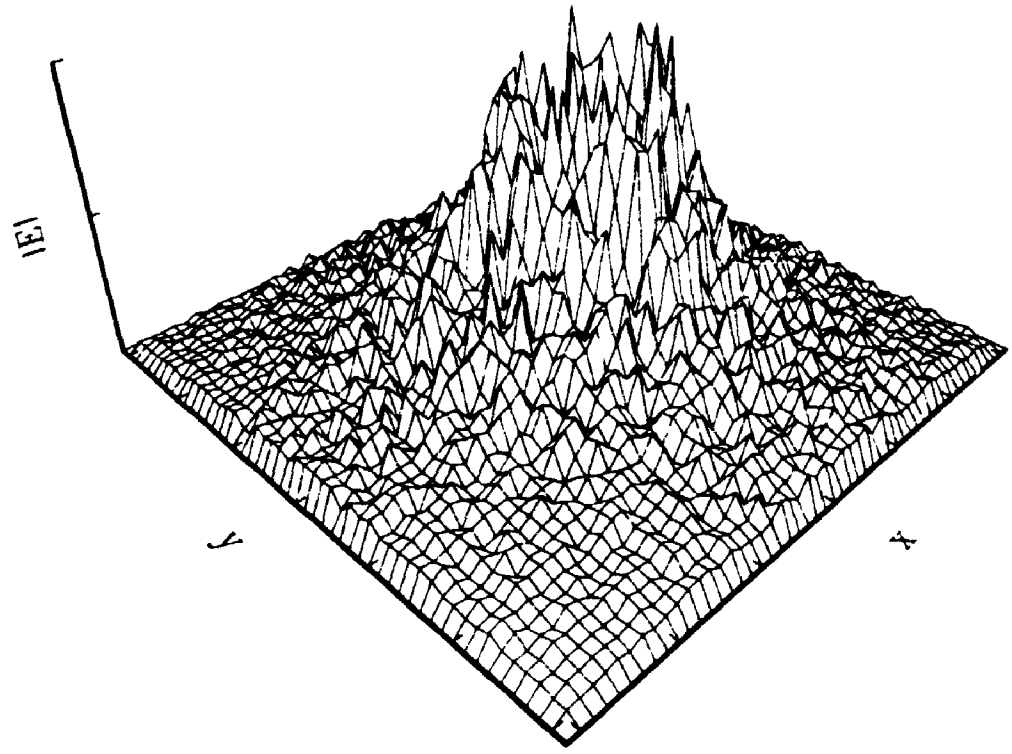

b)

Figure 3-7. Surface plots of the magnitude of the Electric field | E | for a) noiseless synthetic data and b) with 40% uniformly distributed random noise added.

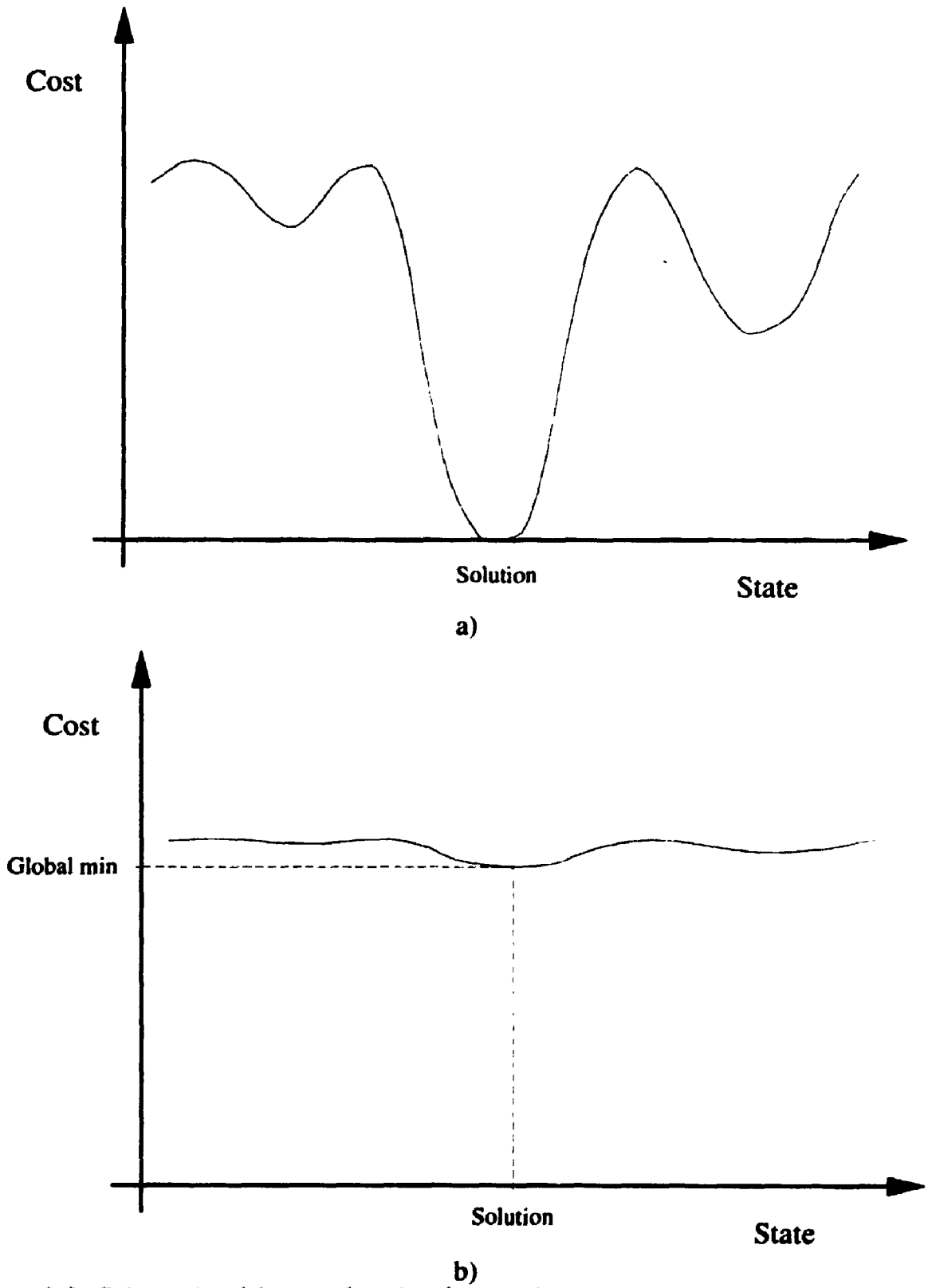

Figure 3-8. Schematic of the cost function for a) noiseless synthetic data and b) noisy data. The situation in b) foreshadows the theoretical breakdown of the method. If the global minimum cost does not correspond to the correct solution, then the inversion will fail.

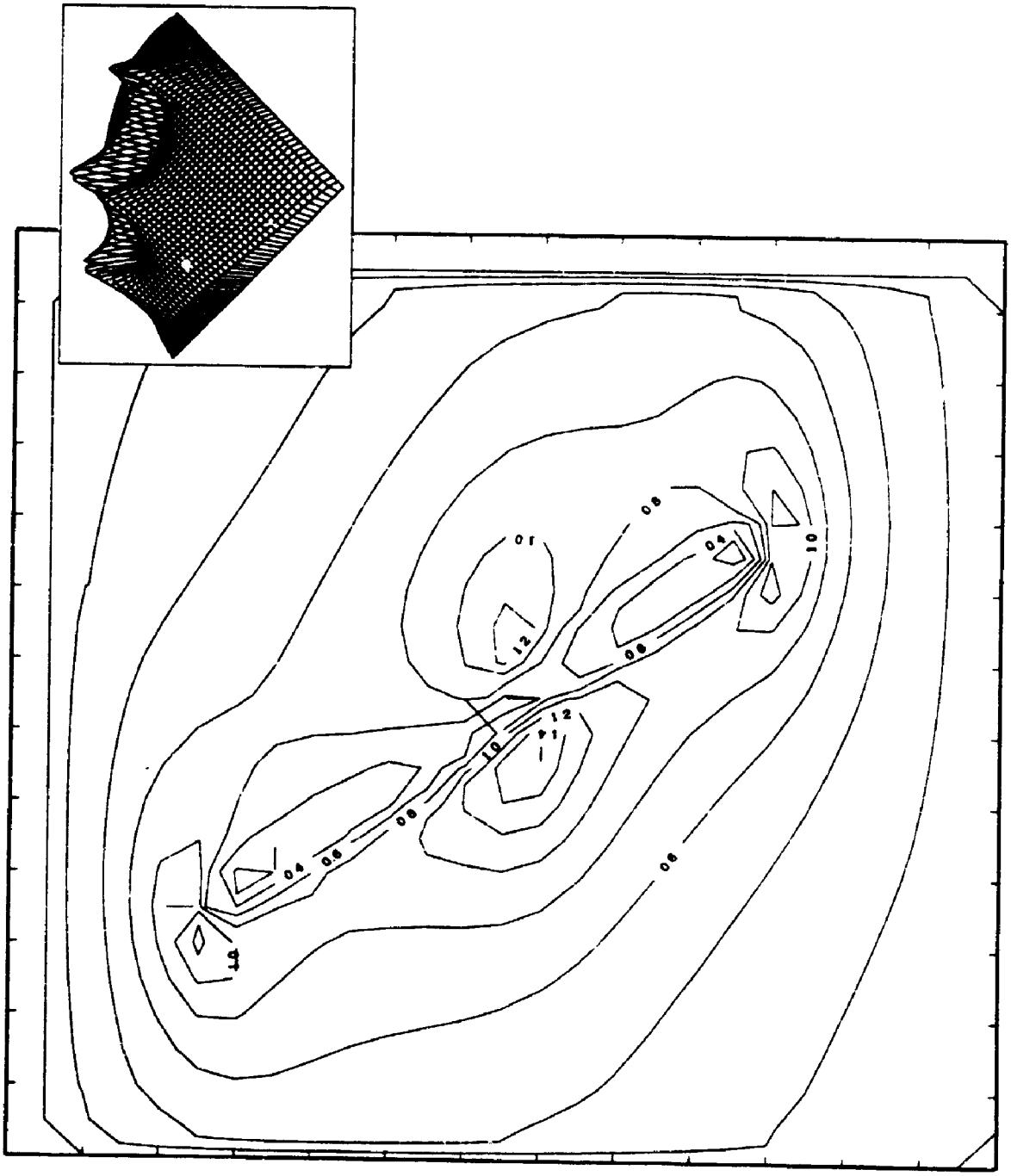

Figure 3-9a)

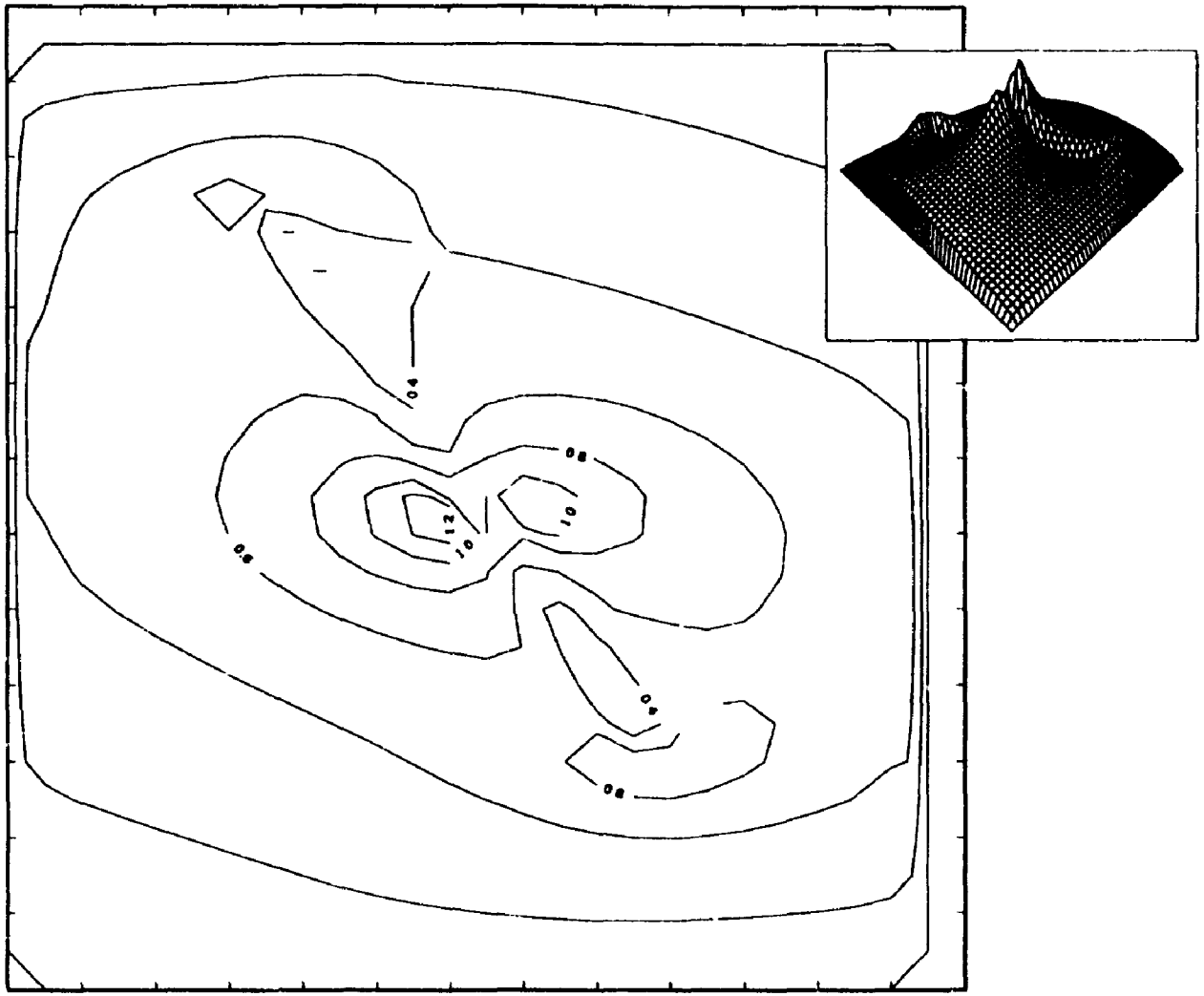

Figure 3-9b)

Figure 3-9. Surface and contour plots of the magnitude of the electric field $|\boldsymbol{E}|$ for synthetic data using dimensions from the Cavendish Geophysical Test Range. In a) the conductivity structure is $\sigma_{HI} = 100$ within the ore body, and $\sigma_{LO} = 1$ everywhere else. In b) a thin layer (thickness $L/4$) of conductive overburden just below the surface with $\sigma_{over}/\sigma_{lo} = 10$ is considered.

CHAPTER 4

An Inverse Problem in Acoustic Scattering

4.1 Introduction

Scattering is defined as the refraction, reflection and diffraction of an incident wave by an obstacle or medium. The scattering obstacle or medium has some sort of different property than the embedding medium, which causes the wave to scatter. The associated direct problem (calculate the scattered wave given the properties of the obstacle or medium) has been studied extensively. Many analytical and numerical solutions exist [29,34,48]. The inverse problem requires one to reconstruct the obstacle or medium given the scattered wave pattern [10,11,32,41,43,46]. Solution of this inverse problem is important in the fields of medical imaging, radar imaging, geophysical prospecting, and non-destructive testing. The forward problem falls into the class of open domain problems. That is, the external boundary conditions are applied at infinity. The boundary condition at infinity is referred to as a radiative boundary condition since it is applied to scattered waves radiating outwards. This class of boundary conditions requires special treatment when using numerical solution techniques [3,16,28].

In obstacle scattering the object is often assumed impenetrable to incoming waves. The scattering mechanism is controlled by the boundary of the object. The boundary can be sound *soft*, sound *hard*, or possess properties of each (impedance boundary condition). Sound *soft* indicates that the boundary is displaced by the incoming waves. This displacement generates an auxiliary wave. With a sound *hard* condition, the boundary is assumed to be rigid. Incident waves simply bounce off the surface. Unlike obstacle scattering, scattering by an inhomogeneous medium allows incident waves to propagate through the medium as well as interact at the boundary of the medium. The transmitted waves are refracted by the inhomogeneous nature of the medium. In the case of electromagnetic scattering, differing conductivity will cause a wave to scatter. In acoustic scattering, differing wave speeds of the media (ie. index of refraction) generate the scattered waves.

The unbounded domain is difficult to model in wave scattering. A truncated computational domain is often used to represent the unbounded domain. This truncated domain imposes artificial boundaries which require artificial boundary conditions. Spurious reflections of outgoing scattered waves often occur on these artificial boundaries leading to inaccurate solutions. Enquist and Majda [17] construct a pseudo-differential operator to apply a local boundary condition on the computational boundary. This local condition is designed to minimize reflections but does not eliminate them. In [48] Tam and Webb propose an improved version of the Bayliss-Turkel [3] conditions, but problems with the anisotropy of the underlying Cartesian finite-difference mesh have to be corrected.

This chapter will present the mathematical model for 2D acoustic waves scattered by an inhomogeneous medium. A numerical method using a finite difference approximation is proposed to solve the modified wave equation in an unbounded domain. In [30] a novel non-reflecting boundary condition (NRBC) is applied to the exterior Helmholtz problem to approximate the infinite domain. This global boundary condition is adapted for use in the case of a scattering medium. An approximation for the Sommerfeld radiation condition (SRC) at infinity (the simplest local boundary condition) is compared with a non-reflecting boundary condition (a global boundary condition). The difference between a local and global boundary condition is the domain of influence for a discrete point in the finite difference approximation. With a local boundary condition, a point only depends on its neighbours as opposed to a global boundary condition, where every point on the boundary is linked to every other point on the boundary. This linking takes place via a Fourier integral. Calibration of the numerical solver is sought with an analytic solution from obstacle scattering. A sample index of refraction describing an inhomogeneous medium is chosen to produce a scattered wave field. The numerical solution for this inhomogeneous medium is contrasted with a highly accurate iterative integral equation (IE) solution which uses a Born approximation as the initial guess.

Once the validity of the forward problem is verified, the inverse problem will be posed. A quasi-solution method as described in chapter 2 is proposed to approximate the inverse problem. The key to the success of a quasi-solution method is to have a fast, efficient and

accurate forward solver as well as a robust minimization algorithm. The minimization scheme that will be used is a variation of the simulated annealing algorithm which can deal with the continuous variables in the parameter space.

Three sample indices of refraction are proposed to test the robustness of the inversion scheme. These sample indices of refraction are substituted into the forward solver to generate the synthetic far-field data. This synthetic data will then be used to represent the measured data required for input into the inverse problem. A reasonable parameterization of the index of refraction to be recovered based on a Fourier expansion is proposed. This parameterization is then used to recover the index of refraction from the synthetic far-field wave pattern.

4.2 Formulation

Direct Problem

The wave equation which governs the propagation of acoustic waves can be derived from the equations of fluid mechanics [10,29]. In a compressible fluid, neglecting viscosity, non-dispersive acoustic waves are governed by the linear wave equation

$$\nabla^2 U = \frac{1}{c^2}\frac{\partial^2 U}{\partial t^2}, \tag{4.2.1}$$

where $U = U(\boldsymbol{x}, t)$ is the velocity potential of the acoustic wave, and $c = c(\boldsymbol{x})$ is the speed of sound in the inhomogeneous medium. The velocity potential U is related to the velocity of the medium $\boldsymbol{v}$ by

$$\boldsymbol{v}(\boldsymbol{x}, t) = \frac{1}{\rho_0}\nabla U, \tag{4.2.2}$$

where ρ_0 is the background density of the fluid. Assuming a time harmonic velocity potential allows one to write

$$U(\boldsymbol{x}, t) = Re\{u(\boldsymbol{x})e^{-i\omega t}\}, \tag{4.2.3}$$

where $u(\boldsymbol{x})$ is the complex valued velocity potential in the Fourier domain, and the wave equation of (4.2.1) becomes the familiar Helmholtz equation or so-called reduced wave equation

(4.2.4) $$\nabla^2 u + \frac{\omega^2}{c^2(x)} u = 0.$$

Let c_0 represent the speed of sound in the homogeneous surrounding medium. Then (4.2.4) becomes

(4.2.5) $$\nabla^2 u + k^2 n(x) u = 0.$$

Here, $k = \omega/c_0$ is the wave number in the homogeneous medium, and $n(x) = c_0^2/c^2(x)$ is the refractive index of the inhomogeneous medium.

The scattered waves are induced by some form of incident waves which interact with the inhomogeneous medium. The simplest form of incident waves which satisfy (4.2.5) outside the inhomogeneous medium are plane polarized waves given by

(4.2.6) $$u_i = e^{ikx \cdot d},$$

where d is a unit vector in the direction of propagation of the plane polarized waves. In 2D, the direction vector d can be written in terms of an angle α as

(4.2.7) $$d = (\cos(\alpha), \sin(\alpha)).$$

Here, α is the angle measured counter-clockwise from the positive x-axis.

Due to the linearity of the governing equation, the total wave field consists of a super-position of incident and scattered waves

(4.2.8) $$u = u_i + u_s.$$

Substituting (4.2.8) into (4.2.5) yields

(4.2.9) $$\nabla^2 u_s + k^2 n(x) u_s = f(x),$$

where

(4.2.10) $$f(x) = (1 - n(x)) e^{ikx \cdot d}.$$

When in the background fluid, n(x)=1. Hence, the source term of (4.2.8) is zero. In this region, scattered waves are simply propagated. When in the inhomogenous medium, however, f(x) is different from zero and represents a driving term.

The only boundary condition is the Sommerfeld radiation condition [29]

(4.2.11) $$\lim_{r \to \infty} \sqrt{r} \left(\frac{\partial u_s}{\partial r} - iku_s \right) = 0.$$

Two valid solutions of (4.2.9) consist of scattered waves propagating outwards as well as scattered waves propagating inwards from infinity. The radiation condition of (4.2.11) ensures that only outwardly propagating waves are considered.

To simplify the application of the boundary conditions, the problem is formulated in 2D polar coordinates ($x = r\cos\theta, y = r\sin\theta$) as

$$\frac{\partial^2 u_s}{\partial r^2} + \frac{1}{r}\frac{\partial u_s}{\partial r} + \frac{1}{r^2}\frac{\partial^2 u_s}{\partial \theta^2} + k^2 n(r,\theta) u_s = f(r,\theta), \quad \text{with}$$

(4.2.12)
$$f(r,\theta) = \{1 - n(r,\theta)\}\exp\{ikr(\cos\theta, \sin\theta)\cdot \boldsymbol{d}\}, \quad \text{and}$$

$$\lim_{r\to\infty} \sqrt{r}\left(\frac{\partial u_s}{\partial r} - iku_s\right) = 0.$$

The equations of (4.2.12) are non-dimensionalized. Two characteristic length scales exist in the problem. They are the wavelength of the incident field given by $\lambda = 2\pi/k$ and the length of a typical dimension of the inhomogeneous medium or obstacle given by a. If the value of k is such that $ka \gg 1$, then the wavenumber is said to lie in the high frequency region. This implies that the second term in Helmholtz's equation is more important than the first, and the resulting phenomenon is diffraction. If $ka \approx 1$, then this regime is called the resonance region. Here, both terms in the reduced wave equation are of equal importance. Wave phenomena such as refraction will be observed for these values of wave number k. A third case exists when $ka \ll 1$. This implies that $k \to 0$, and hence Helmholtz's equation becomes Laplace's equation. In this case, oscillatory solutions are replaced by steady-state solutions. For the purposes of the present work, the irradiating wave number k is assumed to lie in the resonance region. A non-dimensional radial distance variable R is achieved by normalizing by the wave number k to yield

(4.2.13)
$$R = \frac{k}{2\pi} r.$$

The factor of 2π is included to give a wavelength $\lambda = 1$. The system of (4.2.12) now becomes

$$\frac{\partial^2 u_s}{\partial R^2}+\frac{1}{R}\frac{\partial u_s}{\partial R}+\frac{1}{R^2}\frac{\partial^2 u_s}{\partial \theta^2}+(2\pi)^2 n(R,\theta)u_s = F(R,\theta), \quad \text{with}$$

(4.2.14) $$F(R,\theta) = (2\pi)^2(1-n(R,\theta))\exp\{2\pi i R(\cos\theta,\sin\theta)\cdot \boldsymbol{d}\}, \quad \text{and}$$

$$\lim_{R\to\infty}\sqrt{R}\left(\frac{\partial u_s}{\partial R}-2\pi i u_s\right)=0.$$

Inverse Problem

The inverse problem requires an experimentally measured quantity to be used in the reconstruction. A common measurement in the field of acoustic scattering is derived from the outgoing scattered waves. This measurement is referred to as the far-field pattern or is sometimes called the scattering amplitude [10]. This quantity refers to the pattern generated at a large radial distance from the source. At this large distance, specific details of the scattering medium are not noticeable, but rather the medium appears as point source. Here, the domain of influence shrinks from a wedge to a line. This allows the solutions to be separable. That is, the 2D far-field pattern u_{ff} is related to the scattered wave u_s by the asymptotic expression

(4.2.15) $$u_s(r,\theta) = \frac{e^{ikr}}{\sqrt{r}}u_{ff}(\theta)+O\left(\frac{1}{r^{3/2}}\right), \quad r\to\infty.$$

Hence, the far-field pattern represents a function which is defined on the unit circle. The value of the scattered velocity potential in the far-field is given by the angular value of u_{ff} and how far it has propagated from the centre.

The inverse problem involves the index of refraction mapping onto the far-field pattern. Given the index of refraction of the inhomogenous medium, the direct problem calculates the resulting scattered far-field pattern based on an incident wave. Typically, the inhomogeneous medium is bombarded with incident waves from many directions. Hence, the farfield pattern can be thought of as a function of both the angle and the incident wave direction. That is,

(4.2.16) $$u_{ff} = u_{ff}(\theta;\boldsymbol{d}).$$

The inverse problem now requires one to compute the index of refraction given the set of far-field patterns. Consider the operator $\mathcal{M}$ which describes the direct problem. Hence

$$\mathcal{M}n(r,\theta) = u_{ff}(\theta;\boldsymbol{d}), \tag{4.2.17}$$

where $\mathcal{M}$ is based on the Helmholtz equation of (4.2.14) and the definition of the far-field pattern in (4.2.15). Let $\tilde{n}(r,\theta)$ represent the quasi-solution to this inverse problem. The quasi-solution can be computed from the expression

$$\tilde{n} = \min_{n \in \mathcal{N}} \left\{ \sum_{\forall \boldsymbol{d}} \| \mathcal{M}n - u_{ff}^{m}(\theta;\boldsymbol{d}) \| \right\}, \tag{4.2.18}$$

where $\mathcal{N}$ represents the function space from which valid indices of refraction can be selected. The superscript m represents the experimentally measured far-field pattern which is used in the least squares output function and summed over all irradiation directions $\boldsymbol{d}$. The expression on the right hand side of (4.2.18) will be referred to as the cost function. Now the minimization attempts to find the index of refraction which achieves the global minimum of the cost function. The minimization algorithm which will be implemented is simulated annealing.

4.3 Numerical Procedure

Direct Problem

Solution of the partial differential equation of (4.2.14) is facilitated using a finite difference approximation for the derivatives. The computational domain is defined on a discrete mesh of $N_i \times N_j$ points in the respective (θ, R) directions. That is

$$\theta = \theta_0 + i\Delta\theta, \quad i = 0..N_i - 1, \qquad \Delta\theta = \frac{\theta_1 - \theta_0}{N_i - 1}, \tag{4.3.1}$$

$$R = R_0 + j\Delta R, \quad j = 0..N_j - 1, \qquad \Delta R = \frac{R_1 - R_0}{N_j - 1},$$

where (θ_0, R_0) is the bottom left and (θ_1, R_1) is the top right corner of the rectangular domain. This discretization yields a system of linear equations

$$A\tilde{\boldsymbol{u}}_s = \boldsymbol{b}, \tag{4.3.2}$$

where A is a square matrix with $N_i \times N_j$ rows and $\tilde{\boldsymbol{u}}_s$ is the discrete scattered wave field.

The origin must be given special consideration since there is a singularity in the coordinate transformation at R=0. For axisymmetric problems, this is of no concern because the singular terms can be eliminated in (4.2.14) by a straightforward application of l'hôpital's rule. A more general approach is sought which does not assume this symmetry. The Mean Value Theorem for Laplace's equation allows one to write

$$u(0,0) = \frac{1}{2\pi a} \int_C u(a,\theta) d\theta, \tag{4.3.3}$$

where C is a circle of radius a, centred on the origin. This result generalizes to the special case of Helmholtz's equation by

$$u(0,0) = \frac{1}{J_0(ka)} \int_C u(a,\theta) d\theta. \tag{4.3.4}$$

Hence, an expression for the centre point could be derived in terms of the points at $R = \Delta R$, the next ring of points. A simpler approach replaces the computational molecule at the origin with a single Cartesian molecule. The equation governing this single point is

$$\frac{\partial^2 u_s}{\partial x^2} + \frac{\partial^2 u_s}{\partial y^2} + (2\pi)^2 n(x) u_s = f(x). \tag{4.3.5}$$

This molecule is then rotated through the angles $\theta = i\Delta\theta$, $i = 0..N_t - 1$. The value at the origin would then be the average value obtained by all the rotated Cartesian molecules.

The Sommerfeld radiation condition (SRC) of (4.2.12) is the lone boundary condition. This relation is only satisfied as $R \to \infty$, which is impossible to represent exactly given a finite grid. One suitable treatment is to apply

$$\left(\frac{\partial u_s}{\partial R} - 2\pi i u_s \right) \Big|_{R = R_\infty} = 0, \tag{4.3.6}$$

where R_∞ is some large but finite number.

A new approach to approximate the boundary conditions at infinity is proposed by Keller and Givoli [30] with the use of non-reflecting boundary conditions (NRBC). These NRBC's use the analytic solution to the exterior Helmholtz problem to construct a Dirichlet

to Neumann (DtN) map. The DtN map relates the radial derivative on the boundary to boundary values by

$$\left.\frac{\partial u_s}{\partial R}\right|_{R=R_-} = 2\sum_{n=0}{}'\frac{H_n^{(1)\prime}(2\pi R)}{H_n^{(1)}(2\pi R_-)}\int_0^{2\pi}\cos\{n(\theta-\theta')\}u_s(R_-,\theta')d\theta', \tag{4.3.7}$$

where

$$H_n^{(1)}(z) = J_n(z) + iY_n(z) \tag{4.3.8}$$

is the Hankel function of the first kind of order n. The prime on the summation symbol indicates that the $n=0$ term is multiplied by a factor of $\frac{1}{2}$.

This boundary condition differs from the SRC in that it is a global condition, rather than a local condition. That is, every point on the boundary depends on every other point on the boundary due to the integrals in (4.3.7). The effect of this global condition is an alteration to the sparsity pattern associated with the discrete linear differential operator A in (4.3.2). The discretized linear operator associated with a local boundary condition has a block tridiagonal form

$$A = \begin{pmatrix} T & D & & & & & \\ D & T & D & & & & \\ & D & T & D & & & \\ & & D & T & D & & \\ & & & \cdot & \cdot & \cdot & \\ & & & & D & T & D \\ & & & & & D & T \end{pmatrix}, \tag{4.3.9}$$

where T is a tridiagonal matrix and D is a diagonal matrix. Matrix A has at most 5 entries per row. Each block is an $N_i \times N_i$ matrix, and there are N_j blocks in total. The sparsity pattern with the global boundary condition is similar since

$$A = \begin{pmatrix} T & D & & & & & \\ D & T & D & & & & \\ & D & T & D & & & \\ & & D & T & D & & \\ & & & \cdot & \cdot & \cdot & \\ & & & & D & T & D \\ & & & & & D & S \end{pmatrix}. \tag{4.3.10}$$

Here, S represents a dense matrix since every point on the boundary depends on every other point on the boundary. This reinforces the idea that NRBC's are global boundary conditions, rather than local boundary conditions.

The NRBC's, while complicating the sparsity structure, eliminate the reflection of outgoing waves off the artificial boundary. This reflection is minimal for waves travelling perpendicular to the artificial boundary but increases dramatically with higher angles of incidence. The only issue with the use of a NRBC is the number of terms used to approximate the infinite sum in the DtN map. Each term in (4.3.7) represents the next highest harmonic in the angular direction. The highest harmonic representable on a discrete grid is determined by the grid spacing, similar to a Nyquist frequency. If N is the highest harmonic, then

$$N\Delta\theta < \frac{\pi}{2}. \tag{4.3.11}$$

This allows a minimum of five grid points per wavelength. Since $\Delta\theta = 2\pi/(N_t - 1)$, the highest harmonic is given in terms of the number of angular grid points by

$$N < \frac{N_t - 1}{4}. \tag{4.3.12}$$

It is beneficial to use the maximum possible number of terms in (4.3.7) since adding higher harmonics does not affect the sparsity pattern of A, but simply adds correction terms to the existing elements of S in (4.3.10). Adding harmonics above the Nyquist frequency of (4.3.12) causes unpredictable results.

The matrix was stored in compressed row storage (CRS) format [2] which stores only non-zero matrix elements using a row and column pointer array. This is the most practical storage scheme since the origin and the global boundary condition cause an irregular sparsity pattern. The row and column pointers represent extra storage and element access overhead, but this overhead is offset by the savings in storage and matrix operations. An iterative solver was implemented with the Bi-CGSTAB accelerator [50]. This convergence accelerator was chosen since the coefficient matrix was neither symmetric nor positive definite. A Jacobi diagonal scaling was the only preconditioning performed on the sparse matrix. A

more sophisticated preconditioner may reduce the number of iterations required, but it increases the computational expense per iteration. Note that all the storage and acceleration methods have been adapted to deal with complex numbers.

The quantity which will be computed by the direct problem is the far-field scattering pattern for a given index of refraction. It is necessary to derive the far-field at a large distance from the scattering medium, where the waves are propagating outward. Solving the scattering equations in the far-field with a finite difference formulation requires a large computational grid. Having a large grid increases computational effort while sacrificing accuracy and resolution. For this reason, specific numerical techniques need to be implemented. A special hybrid solution technique was employed to solve the direct problem posed in (4.2.18). The finite difference solution of the governing equations requires a finite domain and does not easily facilitate the calculation of the far-field scattering patterns. On the other hand, an integral equation formulation requires no special treatment of the boundary conditions, but it is difficult to solve numerically due to the singularity in the kernel. The proposed hybrid method exploits the strengths of both these techniques. A finite difference solution is used in the region of the inhomogeniety. Then, an integral equation is used to propagate this solution into the far-field.

For the finite difference solution, the inhomogeniety in the index of refraction is assumed to be contained within a finite domain. The index of refraction $n(x) \geq 1$ is different from one within this finite domain, while outside this domain $n(x)=1$. Let

$$\mathcal{D}_A = \left\{ (\theta, R) \in \mathcal{R}^2 \middle| \begin{matrix} -\pi < \theta \leq \pi \\ R < R_A \end{matrix} \right\} \tag{4.3.13}$$

represent this two dimensional domain. This domain will also be chosen for the computational domain described in (4.3.1). Let the computational domain be

$$\mathcal{D}_c = \left\{ (\theta_i, R_j) \middle| \begin{matrix} -\pi < \theta_i \leq \pi, & i = 0..N_i - 1 \\ 0 < R_j < R_A, & j = 0..N_j - 1 \end{matrix} \right\}$$

$$\theta_i = -\pi + i\Delta\theta, \qquad \Delta\theta = \frac{\pi - (-\pi)}{N_i - 1} \tag{4.3.14}$$

$$R_j = 0 + j\Delta R, \qquad \Delta R = \frac{R_A - 0}{N_j - 1}.$$

The far-field pattern is now calculated based on the velocity potential calculated by the finite-difference solution. Let the value R_- denote the radial distance where the far-field pattern will be computed. This value is large but finite. The error in using this approximation is $O(1/R^{3/2})$. The scattered velocity potential at the distance R_- is calculated using

$$u_s(\theta, R_-) = -\pi^2 i \int\int_{\mathcal{D}} H_0^{(1)}(2\pi\tilde{r})\,(1 - n(\theta', R'))u(\theta', R')dA', \tag{4.3.15}$$

where

$$\tilde{r}^2 = R_-^2 + r'^2 - 2R_- r'\cos(\theta - \theta'), \tag{4.3.16}$$

and (θ', R') represent the integration variables. This integral can be easily computed explicitly using $u(\theta, R)$ from the finite difference solution. There is no singularity to consider since (θ, R_-) does not lie in $\mathcal{D}$, and thus the argument of the Hankel function never vanishes ($\tilde{r} > 0$). If $(\theta, R_-) \in \mathcal{D}$, then $\tilde{r} = 0$ for $(\theta', R') = (\theta, R_-)$, and the singularity in the kernel is encountered. The far-field pattern u_{ff} is now achieved by rearranging (4.2.15) to give

$$u_{ff}(\theta; \boldsymbol{d}) \approx \sqrt{R_-}\, e^{-2\pi R_- i} u_s(\theta, R_-; \boldsymbol{d}). \tag{4.3.17}$$

In summary, the hybrid technique involves two steps: 1) solve the PDE in the region of the inhomogeniety, 2) use the solution there as input to the associated integral equation in order to propagate the scattered wave to a large radial distance where the far-field pattern can be approximated accurately.

Inverse Problem

To perform the quasi-solution minimization with simulated annealing, it is necessary to parameterize the index of refraction. One reasonable parameterization is to use the finite difference mesh so that

$$n_{ij} = n(\theta_i, r_j). \tag{4.3.18}$$

This gives a total number of free parameters equal to the total number of gridpoints, $N_i \times N_j$. A reasonably fine mesh used in the computations was 41×17 grid points, which would represent 697 degrees of freedom. This number is fairly intractable for any minimization algorithm. A more sensible parameterization would utilize a Fourier series to reduce the

number of free parameters [23]. The two dimensional finite Fourier series representation chosen was

$$(4.3.19)\qquad \hat{n}(\theta,r)=\begin{cases} 1+a_0\left(1-\dfrac{r}{A}\right)+\displaystyle\sum_{l=-L}^{L}\sum_{m=1}^{M} c_{lm}e^{il\theta}\sin\left(\frac{m\pi r}{A}\right), & 0<r<A \\ 1, & r\geq A \end{cases}$$

where $a_0 \geq 0$ represents the value at the origin, A $(0<A\leq R_A)$ is the radius of a circle which completely contains the inhomogeneity, and c_{lm} represent the complex-valued Fourier coefficients. Note that if we consider only pure real functions for the index of refraction, then $c_{-lm}=\overline{c_{lm}}$ and $Im\{c_{0m}\}=0$. Now the total number of free parameters is $(2L+1)M+2$, where L is the number of Fourier terms in the angular direction, and M is the number of Fourier terms in the radial direction. These parameters can be chosen to produce considerably fewer degrees of freedom than $N_i \times N_j$ while still yielding reasonable approximations to the function.

The advantage of using a Fourier series representation of the index of refraction is that high order terms can be truncated. These high order terms contribute little to the reconstruction but can cause great difficulty for the quasi-solution minimization. The finite Fourier series also provides a certain degree of regularization. By using this representation, we limit the set of eligible functions to those which are continuous and differentiable on $(0,A)$.

The cost function to be minimized is

$$(4.3.20)\qquad C(n(x);d)=\frac{\sum_{N_\alpha}\| u_{ff}^m-\tilde{u}_{ff}\|}{\sum_{N_\alpha}\| u_{ff}^m\|},$$

where the sum is over all the incident wave directions. The factor $\sum_{N_\alpha}\| u_{ff}^m\|$ is included to scale the cost function for different numbers of incident wave directions. A variant of the simulated annealing algorithm is applied to find the global minimum of the cost function. This method provides a clever way to choose the random steps on continuous parameter spaces. In a combinatorial problem, moving between states involves taking discrete steps. The problem when dealing with a continuous parameter space is that a step in a direction could take a continuum of values. No step lengths are defined *a priori*. Taking steps that

are too small wastes computational effort, while failing to fully explore the domain of the cost function. Steps that are too large will be rejected, and no information on the cost function is gained. In the method proposed by Vanderbilt and Louie [51], the excursions of the random walk itself are used to accumulate statistics on the size and shape of the multidimensional cost function. The first and second moments of the walk segments are accumulated based on the accepted reconfigurations. At the end of the *k*th temperature level, the mean and co-variance are used to compute the scaling factors for each dimension. These scaling factors are then used to compute the random steps for the $k+1$st temperature level. As the temperature is decreased, the average accepted step length shrinks since the minimum is being approached. The step statistics can account for this and shrink the scaling factors automatically. The other aspects of the simulated annealing algorithm, such as cooling schedule and stopping criteria are exactly the same as detailed in section 2.6.

4.4 Validation of the Direct Problem

Calibration of the numerical scheme was achieved using two examples. The first comparison uses an analytic solution from obstacle scattering to test the validity of the radiative boundary conditions. The second example uses a sample index of refraction and a numerical integral equation solution to gauge the accuracy of the proposed method for medium scattering. Analytic solutions in obstacle scattering are available for various obstacle geometries and boundary conditions The example chosen from Morse and Feshbach v.2 [34] calculates the scattered wave when plane polarized waves bombard a circular cylinder with a sound-*soft* boundary. A sound-*soft* boundary implies that $u = 0$ when $R=A$, where A is the cylinder radius. Physically, this would refer to a cylinder of Jello which would vibrate freely in the presence of oncoming sound waves. The incident wave displaces the boundary and generates a secondary or scattered wave. This process is much like the noise made when a piece of paper vibrates in front of a loud speaker.

The physical problem is described in non-dimensional coordinates by

$$\nabla^2 u + (2\pi)^2 u = 0 \quad (\theta, R) \in \mathcal{D} \tag{4.4.1}$$

$$u = 0 \qquad \text{on } C.$$

Since $u = u_i + u_s$ and the incident waves are plane polarized,

$$u_i = \exp(2\pi i x). \tag{4.4.2}$$

Then (4.4.1) becomes

$$\nabla^2 u_s + (2\pi)^2 u_s = 0 \qquad (\theta, R) \in \mathcal{D}$$

$$u_s = -\exp(2\pi i R\cos\theta) \qquad \text{on } C \tag{4.4.3}$$

$$\lim_{R\to\infty} \sqrt{R}\left(\frac{\partial u_s}{\partial R} - 2\pi i u_s\right) = 0.$$

This system is closely related to (4.2.14) and allows assessment and comparison of the two different boundary conditions SRC and NRBC. The analytic solution of (4.4.3) is

$$u_s(\theta, R) = -2i \sum_{n=0}^{\infty}{}' \exp\left\{\left(\frac{n\pi}{2} - \delta_n\right)i\right\} \sin(\delta_n) H_n^{(1)}(2\pi R)\cos(n\theta), \tag{4.4.4}$$

where

$$\delta_n = arg\{H_n^{(1)}(2\pi A)\} + \frac{\pi}{2}, \tag{4.4.5}$$

is the phase angle of the Hankel function.

The computational domain $\mathcal{D}$ is

$$\mathcal{D} = \left\{ (\theta, R) \;\middle|\; \begin{array}{l} \theta \in [-\pi, \pi]; \quad \Delta\theta = \dfrac{2\pi}{N_\theta - 1} \\ R \in [1, R_\infty]; \quad \Delta r = 2^{-4} \end{array} \right\}. \tag{4.4.6}$$

The analytic solution represented by (4.4.4) can be seen in figure 4-5. Note the peak amplitude is in the wake of the cylinder where the incident waves are reflecting. Two error measures were used for evaluation purposes. One was the $\|\cdot\|_{L_2}$ of the difference between the analytic solution and the numerical solution. That is

$$Error = \frac{\| u_s - \tilde{u}_s \|_{L_2(r,\theta)\in\mathcal{D}}}{\| 1 \|_{L_2(r,\theta)\in\mathcal{D}}}, \tag{4.4.7}$$

where $\bar{u}_s$ is the numerical solution. The difference in (4.4.7) is normalized by $\| \ \|_{L_2(r,\theta)\in\mathcal{D}}$ to allow comparison between different computational domains. The other error measure was the percentage norm error given by

$$\%Error(\theta,R)=\frac{|u_s-\bar{u}_s|^2}{|u_s|^2}\cdot 100\%. \tag{4.4.8}$$

The percentage error plot (figure 4-6a) for the SRC shows a maximum error of about 1.5%. This maximum occurs near $\theta = 0$, which represents the area in the wake of the plane polarized incident waves. Most error is expected in this region since this is where most refraction occurs. Reflection off the surface of the obstacle generates outgoing waves which strike the computational boundary at near normal incidence. This is the case near $\theta = \pi$. The refracted waves, however, strike the computational boundary at an oblique angle causing erroneous reflections. The maximum error for the NRBC (figure 4-6b) is < 0.1%, which is an order of magnitude better than the numerical solution with the SRC.

Another useful comparison is to see how the accuracy of the numerical solution scales with the mesh spacings. The finite difference approximation for a second derivative using a central difference formula is deemed second order since

$$f''_i=\frac{f_{i+1}-2f_i+f_{i-1}}{\Delta x^2}+O(\Delta x^2). \tag{4.4.9}$$

Assuming that the truncation error is a function of the mesh spacing $(\Delta\theta, \Delta r)$ and is independent for each direction allows one to write

$$E_1(\Delta\theta) \doteq (\Delta\theta)^{\alpha}, \quad \text{and} \tag{4.4.10a}$$

$$E_2(\Delta r) = (\Delta r)^{\beta}, \tag{4.4.10b}$$

where E_1 and E_2 represent the defect in the solution due to truncation error in the finite difference approximation. If the number of points are doubled, the error should behave like

$$E_1(\Delta\theta/2) = (\Delta\theta/2)^{\alpha}, \quad \text{and} \tag{4.4.11a}$$

$$E_2(\Delta r/2) = (\Delta r/2)^{\beta}. \tag{4.4.11b}$$

Dividing (4.4.10) by (4.4.11) and solving for α and β yields

$$\alpha = \ln\left(\frac{E_1(\Delta\theta)}{E_1(\Delta\theta/2)}\right)/\ln(2) \qquad (4.4.12a)$$

$$\beta = \ln\left(\frac{E_2(\Delta r)}{E_2(\Delta r/2)}\right)/\ln(2). \qquad (4.4.12b)$$

$\Delta r = 2^{-5}$	α		$\Delta\theta = 2\pi/160$	β	
$\Delta\theta$	NRBC	SRC	Δr	NRBC	SRC
$2\pi/40$	3.89	1.43	2^{-3}	2.80	2.54
$2\pi/80$	1.31	0.50	2^{-4}	2.10	0.90
$2\pi/160$	1.54	0.021	2^{-5}	1.25	0.264

Table 4-1. Values of the Error exponents α and β for various mesh spacings. A theoretical maximum of 2 exists since a second order finite difference formula is used to discretize the derivatives in the PDE.

Table 4-1 shows the results of these calculations. A theoretical maximum of 2 should be reached if there are no other sources of error other than truncation error. This is not true in the present case due to the approximation of the infinite boundary condition. Note that the values for the NRBC are much closer to the theoretical limit than the values for the SRC case. Also, the exponent α is larger than the exponent β for the NRBC case, which indicates that the error in the solution is more sensitive to changes in the angular mesh width. This is due to the fact that the angular mesh spacing limits the highest harmonic which can be resolved in the application of the integral boundary conditions of (4.3.6). Note that when increasing the number of points in the θ direction from 81 to 161 points, there is virtually no increase in the accuracy of the solution for the SRC case. Here, the method has saturated the possible accuracy of the numerical solution. Any savings at this point in truncation error are offset by the approximation of the boundary condition at infinity. This observation can also be seen in figure 4-7. Here, the solution error is plotted for various combinations of gridspacings $\Delta\theta$, ΔR. The error is less with the NRBC than the SRC for all grid spacings. Best performance of the finite difference solution is found when $\Delta\theta$ and ΔR are of the same magnitude.

Validation of the scattering solution in the presence of an inhomogeneous medium was performed by comparing the finite difference solution to an numerical integral equation solution for a sample index of refraction. The function given by

$$n_1(R) = \begin{cases} 2 - 5/3R, & 0 < R < 0.6 \\ 1, & R \geq 0.6 \end{cases} \tag{4.4.13}$$

was chosen since it is continuous and independent of θ. A sketch of this scalar field can be seen in figure 4-8. The real and imaginary parts of the velocity potential u scattered by the inhomogeneous medium can be seen in figure 4-9. This solution was generated using NRBC on the computational domain

$$\mathcal{D} = \left\{ (\theta, R) \middle| \begin{array}{ll} \theta \in (-\pi, \pi] & \Delta\theta = 2\pi/160 \\ R \in [0,2] & \Delta R = 2^{-5} \end{array} \right\}. \tag{4.4.14}$$

The maximum values of the scattered potential occur on the ray $\theta = 0$. This is expected since this area is in the wake of the medium.

The integral equation (IE) describing this system is

$$u(r) = u_i(r) - i\pi^2 \iint_{\mathcal{D}} H_0^{(1)}(2\pi|r - r'|)(1 - n(r'))u(r')dA', \tag{4.4.15}$$

where $r = (\theta, R)$ is the space variable, and $r' = (\theta', R')$ is the integration variable. This is a Fredholm integral equation of the second kind. The Born approximation replaces u under the integral sign with u_i allowing (4.4.15) to be solved explicitly. This approximation eliminates secondary scattering effects since only incident waves are assumed to scatter; scattered waves do not scatter again. This is referred to as the *zero*th order Born approximation. A more accurate numerical solution to the integral equation of (4.4.15) can be achieved by using an iterative method where successive approximations for u are substituted under the integral sign. That is,

$$u^{(n+1)}(r) = u_i(r) - i\pi^2 \iint_{\mathcal{D}} H_0^{(1)}(2\pi|r - r'|)(1 - n(r'))u^{(n)}(r')dA' \tag{4.4.16}$$

$$u^{(0)} = u_i.$$

Solutions can be found to high accuracy by taking a large number of iterations. The iterates converge to the exact solution provided that the kernel in (4.4.16) is contractive. This method, however, is computationally intensive. For example, each iteration in the integral equation solution takes 374.7 CPU seconds on a Pentium/90. The corresponding PDE solution on a 81x33 point grid takes only 65.1 CPU seconds in total. The first iteration yields the Born approximation as suggested above. The 50th order solution is computed and displayed in figure 4-10. Estimates of the accuracy of this solution were drawn from the magnitude of the difference between successive iterates

$$\| u^{(50)} - u^{(49)} \|_{L_2} < 10^{-5}. \tag{4.4.17}$$

Comparison between the 50th order Born approximation and the PDE solution with non-reflecting boundary conditions is seen in figure 4-11. Here the absolute value of the difference between the IE and the PDE solutions is plotted per grid point. The maximum absolute difference of 0.097 occurs on the centreline in the wake of the medium near the outer boundary. This corresponds to a relative difference of 1.3%. The L_2 norm of the error was found to be 0.13. The integral equation solution, while accurate, is not feasible for a reconstruction algorithm since it requires significant amounts of CPU every time it is solved. The finite difference solution with non-reflecting boundary conditions provides accurate results in a fraction of the time.

4.5 Validation of the Inverse Problem

Three proof of principle examples were used to evaluate the performance of the inversion. Synthetic far-field data is generated by substituting the known indices of refraction into the forward solver developed in (4.3.1). The synthetic far-field data from the forward solution represents the measured far-field values. Two indices of refraction are chosen to be axisymmetric, while the other one is non-axisymmetric. The inversion scheme is applied to the synthetic data to see if the generating indices of refraction can be reconstructed. The performance of the reconstruction is measured in terms of the reconstruction error defined as

$$\frac{\| n - \hat{n} \|}{\| n \|} \cdot 100\%. \tag{4.5.1}$$

A fine grid (161x33 points) was used to generate the synthetic data to high precision. The method used to generate the synthetic data for the inversion should be independent of the solver for the direct problem. This is to avoid what Colton and Kress [10] refer to as an *inverse crime*. If the same solution scheme generates both the synthetic data and the forward solutions for the quasi-solution minimization, then one is merely testing the reproducibility of the direct problem. Identical calculation errors will be seen in both far-field computations. Generating synthetic data using a different method which uses different approximations and creates different round-off errors will give a true test of the robustness of the inversion scheme.

Example 4-1: Conical cap

This index is an axisymmetric index of refraction which was used in the validation of the direct problem. The function is given by

$$(4.5.2) \qquad \cdot_1(R) = \begin{cases} 2 - 5/3R, & 0 < R < 0.6 \\ 1, & R \geq 0.6 \end{cases}.$$

Let $\hat{n}_1$ represent the parameterization of this function. The parameterization is

$$(4.5.3) \qquad \hat{n}_1 = \begin{cases} A = 0.6 \\ a_0 = 1 \\ c_{lm} = 0 \end{cases}.$$

Table 4-2 contains the parameters and results for the reconstruction of this function for two different grid resolutions. The parameterization of this simple function is exact as can be seen by the best possible reconstruction error of 0%. The function was assumed to be axisymmetric by choosing L=0. This also allows one incident wave direction to be used, $N_\alpha = 1$. The algorithm finds a minimum cost of 2.168×10^{-3} when the 41x17 point mesh is used. This corresponds to a reconstruction error of 1.4%. Comparison of the two reconstructed functions is seen in figure 4-17. Notice that the 41x17 grid reproduces a sharper function.

Interesting results are observed when the function to be reconstructed is assumed to be non-axisymmetric (see Table 4-3). Here, two Fourier terms in the axial direction are assumed (L=2). The best possible reconstruction has an error of 0% because the simple conical cap can be represented exactly with the chosen parameterization. The minimum

N_α	N_i	N_j	L	M	Minimum Cost		$\|n-\hat{n}\|/\|n\| \cdot 100\%$	
					Possible	Found	Possible	Found
1	21	9	0	2	6.7e-3	6.8e-3	0%	1.3%
1	41	17	0	2	5.6e-4	2.2e-3	0%	1.4%

Table 4-2. Performance of the reconstruction algorithm for the conical cap of figure 4-8.

possible cost is non-zero since the far-field data was generated by an independent means. This over-parameterization makes it more difficult for the reconstruction if only one irradiation direction is used. The reconstruction with $N_\alpha = 1$ and $L=M=2$ is pictured in figure 4-18a. Notice that the centre peak is shifted forward in the direction of the incoming wave. Hence, the silhouette of the function seen by the incoming wave appears unchanged. It is only when the reconstructed function is observed transverse to the irradiation direction that the poor reconstruction is noticeable. To perform a realistic reconstruction, more than one wave direction is required such as in figure 4-18b where $N_\alpha = 3$. Here, the centre peak is correctly located at the origin. Slight asymmetries affect the function. However, the reconstruction results in an error of 4.4%. This is less than half of the reconstruction error that results when only one incident wave direction is used.

N_c	N_i	N_j	L	M	Minimum Cost		$\|n-\hat{n}\|/\|n\| \cdot 100\%$	
					Possible	Found	Possible	Found
1	41	17	2	2	5.6e-4	0.038	0%	9.8%
3	41	17	2	2	2.4e-3	0.011	0%	4.4%

Table 4-3. Performance of the reconstruction algorithm for the conical cap when a non-axisymmetric function is assumed.

Example 4-2: Top hat Function

This index is an axisymmetric index of refraction given by

$$n_2(\theta,R) = \begin{cases} 2, & 0 < R < 0.6 \\ 1, & R \geq 0.6 \end{cases}. \tag{4.5.4}$$

This function was used as an example in [23,11]. Let $\hat{n}_2$ represent the parameterization of this function. The parameterization is,

$$\hat{n}_2 = \left\{ \begin{array}{c} A = 0.6 \\ a_0 = 1 \\ c_{0m} = (-1)^{m+1} \dfrac{2}{m\pi} \\ c_{lm} = 0, \quad l \neq 0 \end{array} \right\}, \tag{4.5.5}$$

as illustrated in figure 4-14b. Note the Gibb's ringing near the sharp edge of the hat at *R=0.6*. This sharp edge makes it more difficult for the inversion process since the Fourier series contains significant power in the higher frequencies.

N_α	N_l	N_j	L	M	Minimum Cost		$\|n-\hat{n}\|/\|n\| \cdot 100\%$	
					Possible	Found	Possible	Found
1	21	9	0	2	0.07	0.025	7.2%	13.0%
1	21	9	0	4	0.07	0.024	2.7%	12.9%
1	21	9	0	6	0.07	0.019	3.8%	19.1%
1	41	17	0	4	0.01022	0.01025	10.2%	9.9%

Table 4-4. Performance of the reconstruction algorithm for the top hat of figure 4-14a.

The results for the reconstruction of the top hat function can be viewed in Table 4-4. The first three reconstructions use a very coarse numerical grid for the solution of the direct problem and a single incident direction $N_\alpha = 1$. These results illustrate a serious danger in the application of this inversion scheme. The quasi-solution method relies on the minimum cost solution to be the best approximation to the inverse problem. Here the cost found is significantly less than the cost generated by the true index of refraction, yet the reconstruction error is greater than the error when the best possible parameterization is used. Increasing the number of terms in the parameterization decreases the minimum cost found but worsens the reconstruction results as seen when *M=6*. This phenomenon represents the theoretical breakdown of the method. Here, the minimum cost is not the best reconstruction. The only way the quasi-solution method can distinguish between competing functions for reconstruction is based on their output least-squares cost. If a function has a lower cost but actually is a worse approximation, then the inversion by quasi-solution fails.

The breakdown of the quasi-solution inversion as detailed above can be attributed to the poor resolution used in the forward problem. The 21x9 point mesh is too coarse to give an accurate solution of the forward problem. Doubling the number of meshpoints in each dimension remedies the problem. The 41x17 point mesh in Table 4-4 has a minimum theoretical cost of 0.01022. The best recovered cost was 0.01025, which is very close to the theoretical minimum. The corresponding reconstruction error was 9.9%.

Example 4-3: Twin Peaks

This index is an asymmetric index of refraction used as Example 2 of [11] given by

$$n_3(r) = \begin{cases} \frac{1}{2}(3+\cos 2\pi r_1), & 0 < r_1 < 0.5 \\ \frac{1}{2}(3+\cos 2\pi r_2), & 0 < r_2 < 0.5 \\ 1, & \text{otherwise} \end{cases}. \tag{4.5.6}$$

Let $\hat{n}_3$ represent the parameterization of this function. The parameterization was computed numerically using a Fourier integral. The parameterized function for $L=2$ and $M=2$, is

$$\hat{n}_3 = \begin{Bmatrix} A = 1 \\ a_0 = 0 \\ c_{lm} = 0, \quad l \in odd \\ c_{01} = 0.2731 \\ c_{02} = 0.04211 \\ c_{21} = 0.2021 + 0i \\ c_{22} = 0.0138 + 0i \end{Bmatrix}. \tag{4.5.7}$$

The error in using this parameterization is 6.6%.

N_α	N_i	N_j	L	M	Cost		$\|n-\hat{n}\|/\|n\| \cdot 100\%$	
					Possible	Found	Possible	Found
9	41	25	2	2	6.42e-3	0.1352	6.6%	9.2%

Table 4-5. Performance of the reconstruction algorithm for the twin peaks of figure 4-15a.

The performance of the twin peaks reconstruction can be seen in Table 4-4. Here nine irradiation directions were used since the function is not axisymmetric. There is still room for improvement in the minimization since the best found cost is still 3 orders of magnitude

larger than the theoretical global minimum. Nonetheless, the reconstructed function was only in error by 9.2%. In [11] where this function was suggested, Colton and Monk were able to achieve a reconstruction with only 1% error by using 51 incident wave directions as well as 4 different wavenumbers. This gives considerably larger amounts of measured data to compare with. For the current inversion algorithm, this number of incident wave directions and wavenumbers would be unfeasible.

4.6 Discussion

A fast, computationally efficient numerical solver was developed for the solution of 2D acoustic scattering in an inhomogeneous medium. Calibration of the numerical scheme was achieved using an analytic solution in obstacle scattering. The obstacle scattering example also allowed comparison of two separate approximate boundary conditions. The numerical solution with non-reflecting boundary conditions proved superior as compared to the numerical solution which uses a straightforward application of the Sommerfeld radiation condition at a finite distance.

An accurate numerical solution to the inhomogeneous medium problem was generated using an iterative Born approximation. This integral equation solution was used to compare with the numerical solution of the associated PDE with non-reflecting boundary conditions. The NRBC was found to be in error by no more than 2% in the wake of the inhomogeneous medium. The real advantage is the savings in computation time. The finite difference solution used approximately one minute of CPU. The integral equation solver used approximately six minutes of CPU per iteration. Hence, the 50th order solution requires five hours to achieve an accurate solution.

The reconstruction algorithm used the finite difference forward solver along with a simulated annealing minimization scheme to approximate the inverse problem. A suitable parameterization for the index of refraction in terms of a 2D Fourier series was proposed. The reconstruction was tested using three sample indices of refraction.

The reconstruction of axisymmetric profiles is performed well if the parameterized function is assumed to be axisymmetric. Only one irradiation direction is required to give good results. If the parameterized function is assumed to be not axisymmetric, then the

resolving power of the reconstruction in the direction of the incident wave is severely limited. More than one incident wave direction is required to achieve accurate reconstructions. Also, truncating the Fourier series can benefit the reconstruction since higher order terms do not necessarily mean more accurate reconstruction. The four term reconstruction of the top hat on a 21x9 point mesh achieved a reconstruction error of 12.9%. The corresponding six term reconstruction had a reconstruction of 19.1%. The complicated twin peaks function was reconstructed using nine incident wave directions for an error of 9.2%.

While the proposed inversion method is feasible, the computational load of the simulated annealing algorithm is considerable. For example, the reconstruction of the top hat function on a 21x9 grid required 7614 function evaluations to find the global minimum which corresponds to 7.9 hours of CPU time. Possible remedies include reducing the cost of each penalty function evaluation. A penalty function evaluation requires the iterative solution of the finite difference matrix. Increasing the efficiency of the iterative sparse matrix solver would reduce the load of each function evaluation. The sparse matrix solver uses the Bi-CGSTAB accelerator. More sophisticated pre-conditioning may reduce the number of iterations required. Also, a careful choice of annealing parameters is required to reduce the number of iterations while being careful not to quench the system into a local minimum.

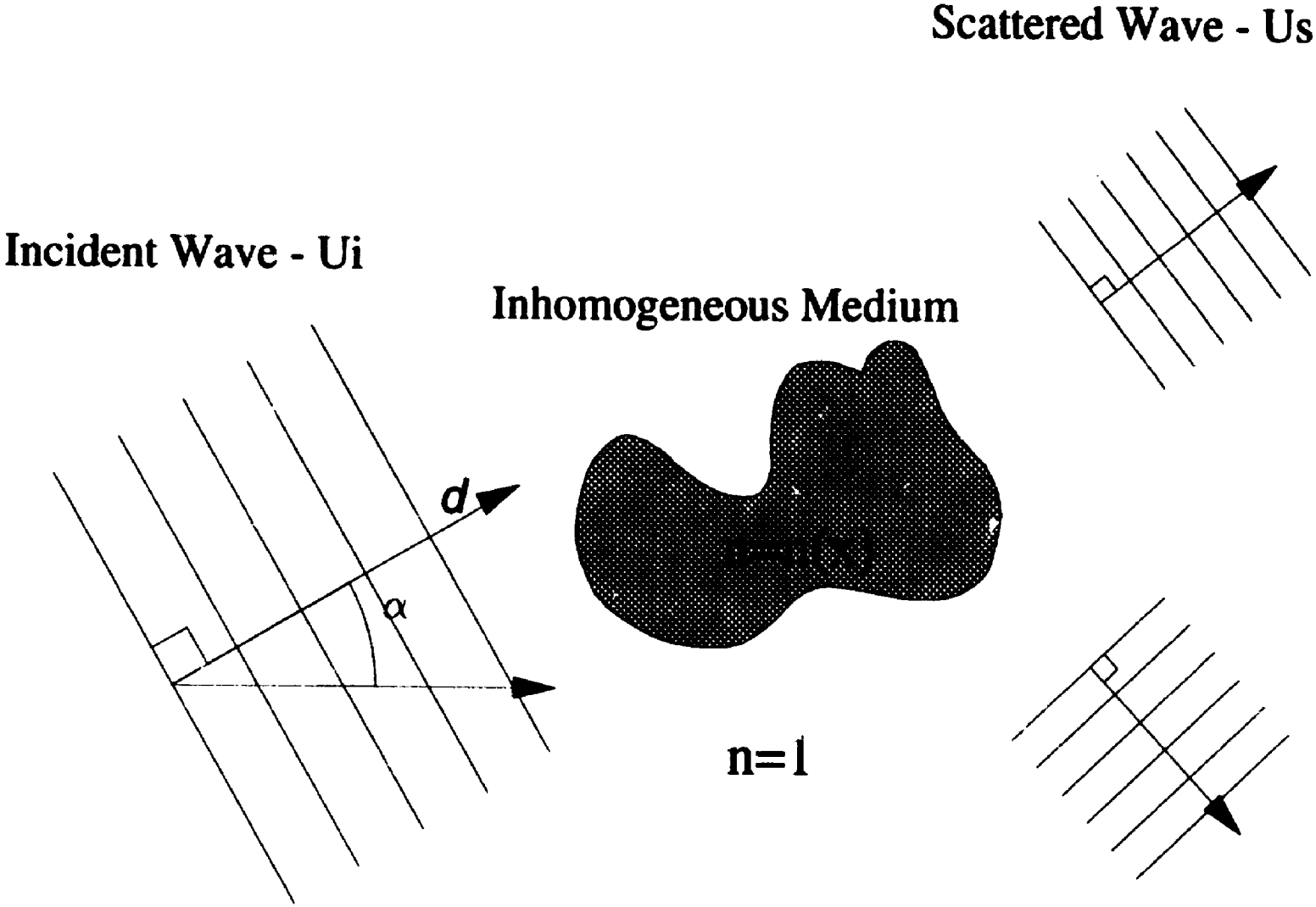

Figure 4-1. Schematic of inhomogeneous medium scattering. Incident waves are imparted on the medium from various directions ***d***. The scattered waves leave in all directions. The inverse problem attempts to use the scattered waves from numerous irradiation directions to reconstruct the index of refraction n of the inhomogeneous medium.

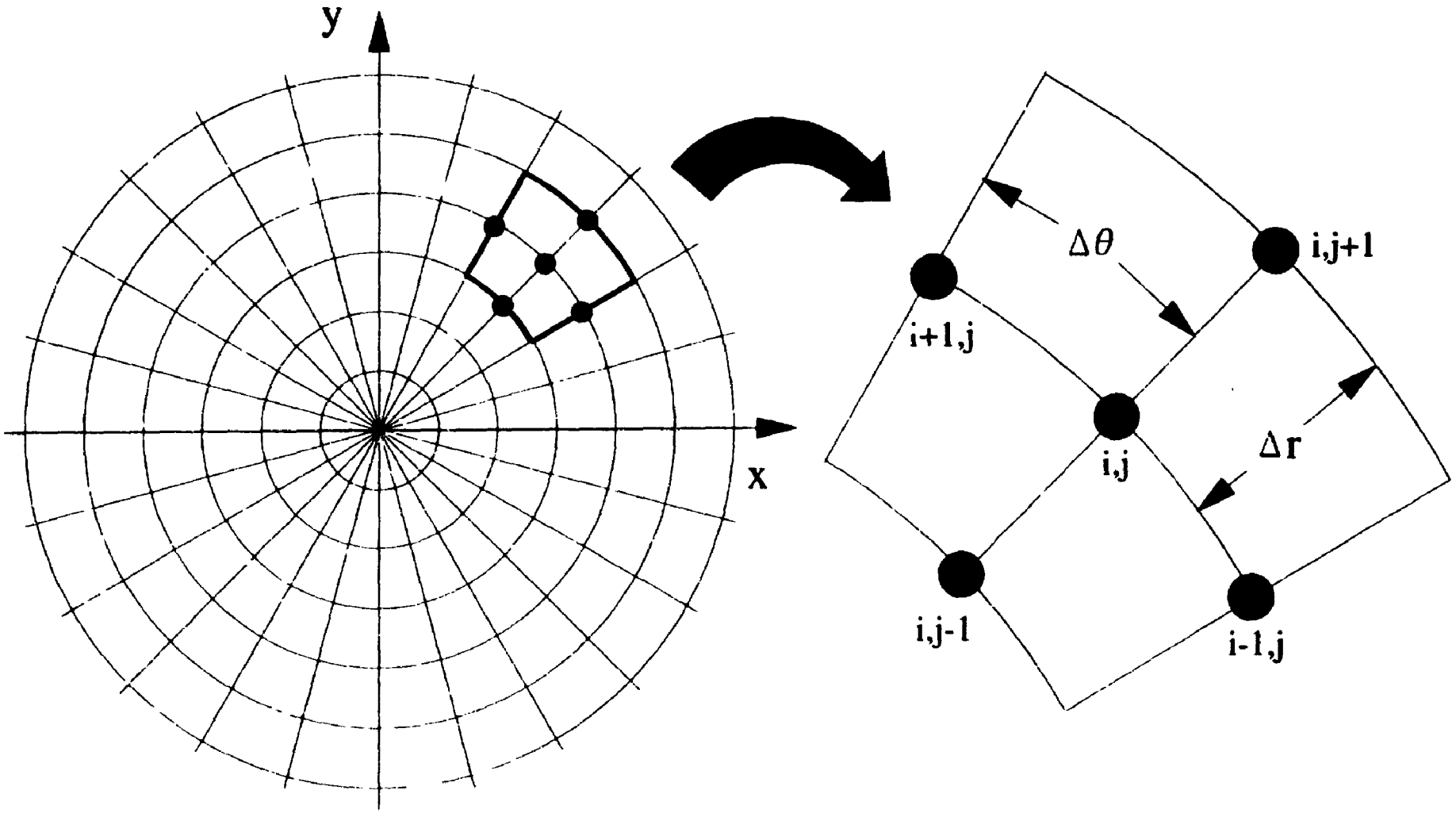

Figure 4-2. Sketch of the computational domain in cylindrical polar coordinates used for the finite difference discretization. Inset is the computational molecule and the node numbering scheme. The domain is $N_i \times N_j$ points in the (θ, r) directions, respectively.

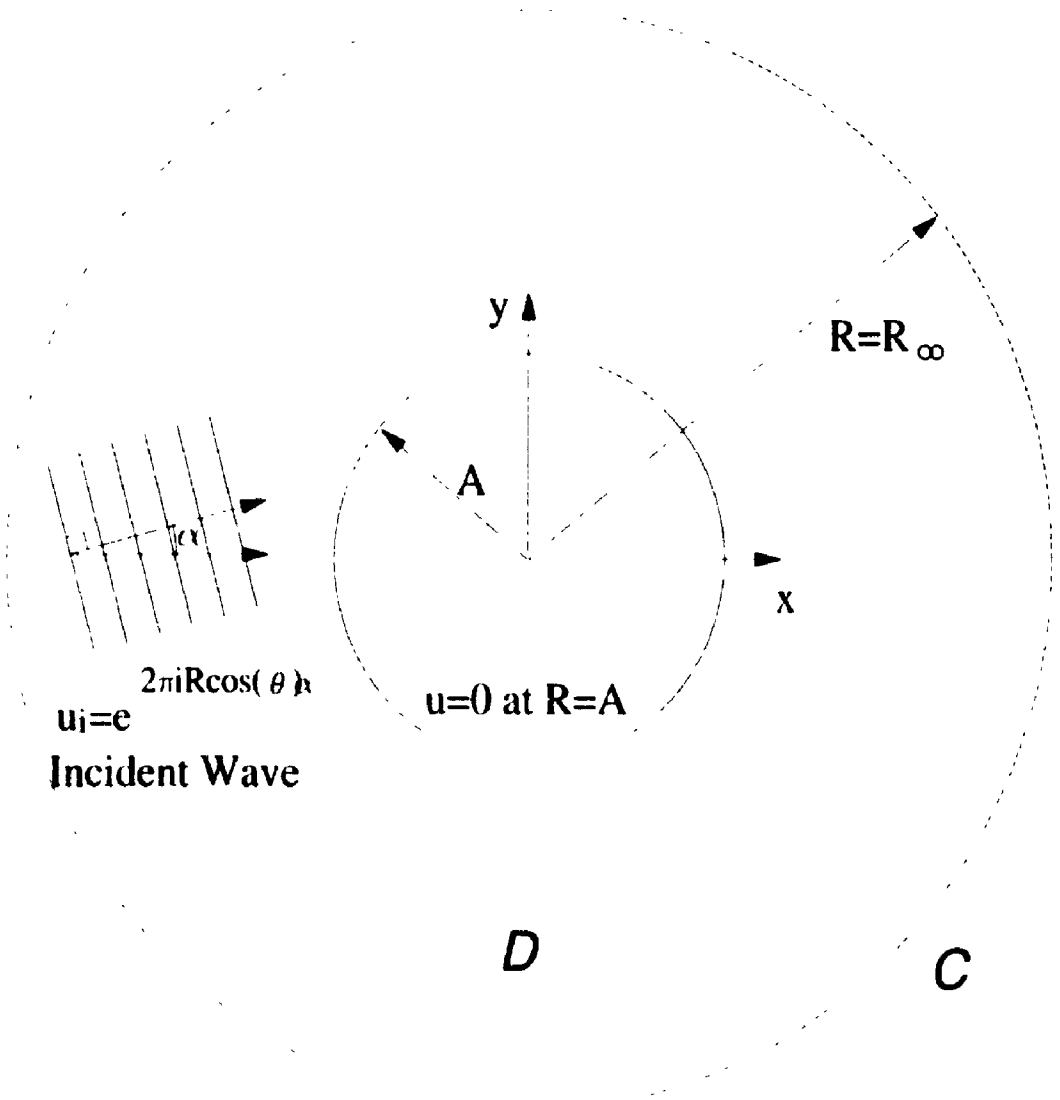

Figure 4-3. Schematic of the computational domain for the obstacle scattering problem used to calibrate the numerical solution. A plane parallel wave is imparted on an infinite cylinder of radius *A* with a sound *soft* boundary.

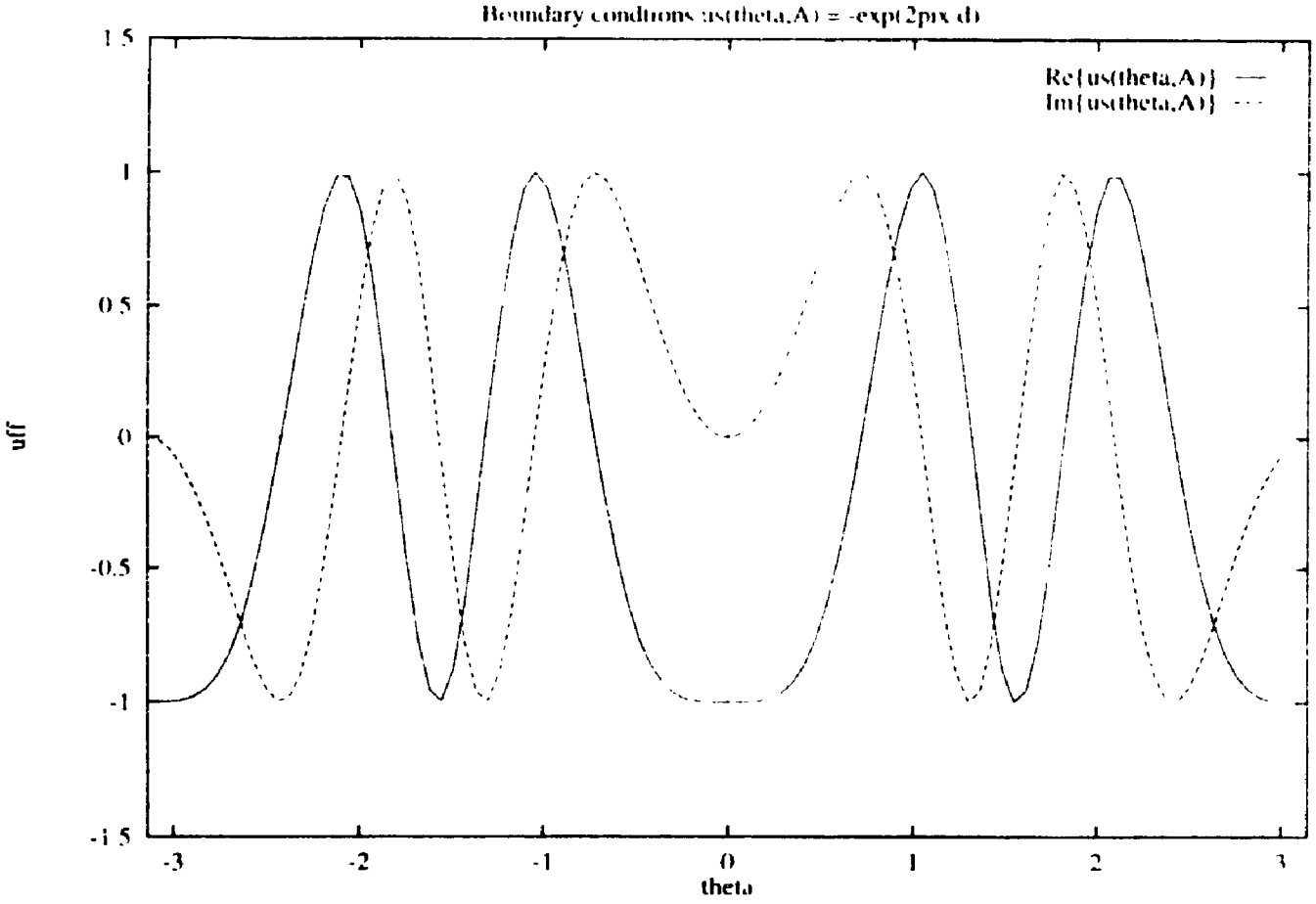

Figure 4-4. Boundary Conditions on the cylinder (R=A) for the obstacle scattering problem. Sound *soft* boundaries imply that u=0, hence $u_s = -\exp\{2\pi i x \cdot \boldsymbol{d}\}$ at R=A.

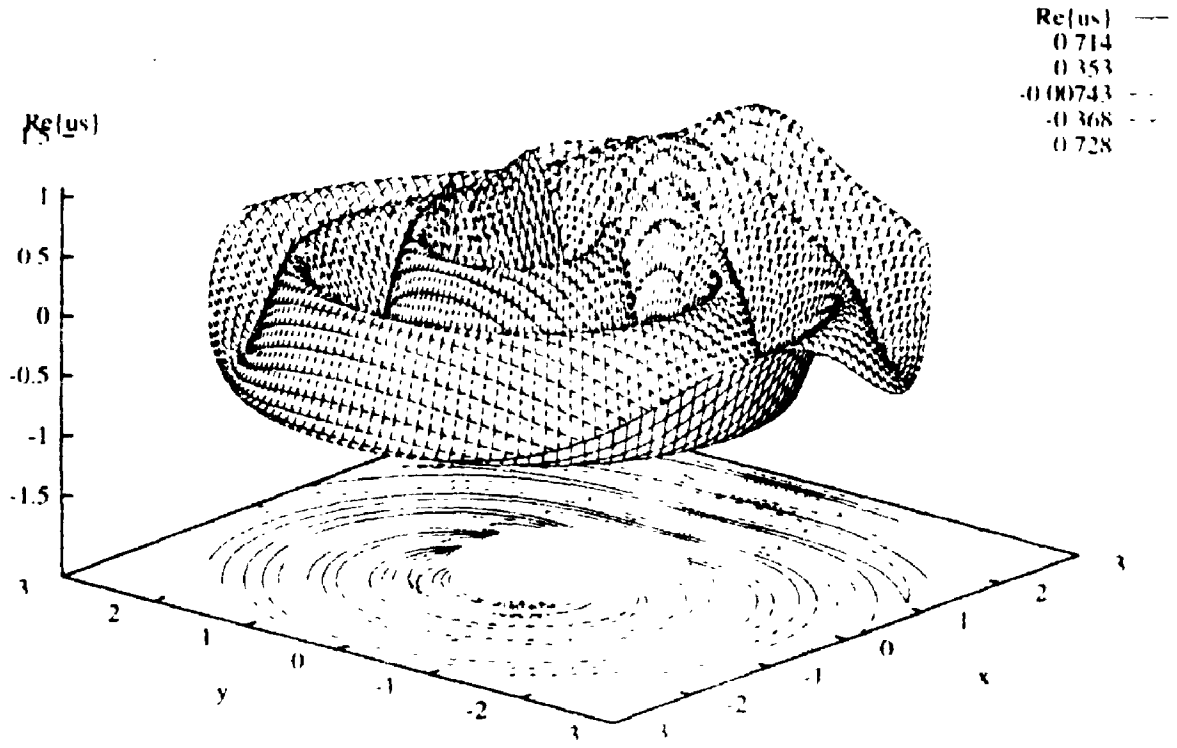

Figure 4-5a)

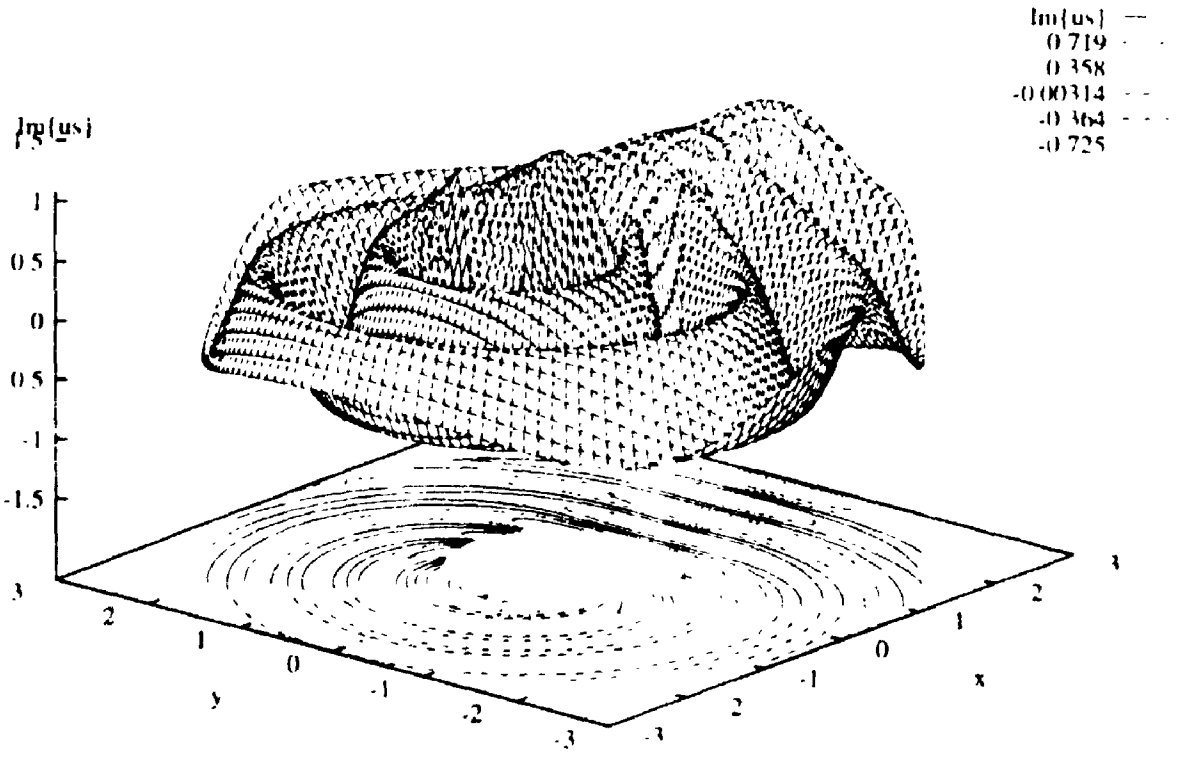

Figure 4-5b)

Figure 4-5. a) Real and b) imaginary parts of the scattered waves for the analytic solution of the obstacle scattering problem. Note the larger magnitude of the waves in the wake of the cylinder ($\theta = 0$) indicating that refraction of the waves around the cylinder is occurring.

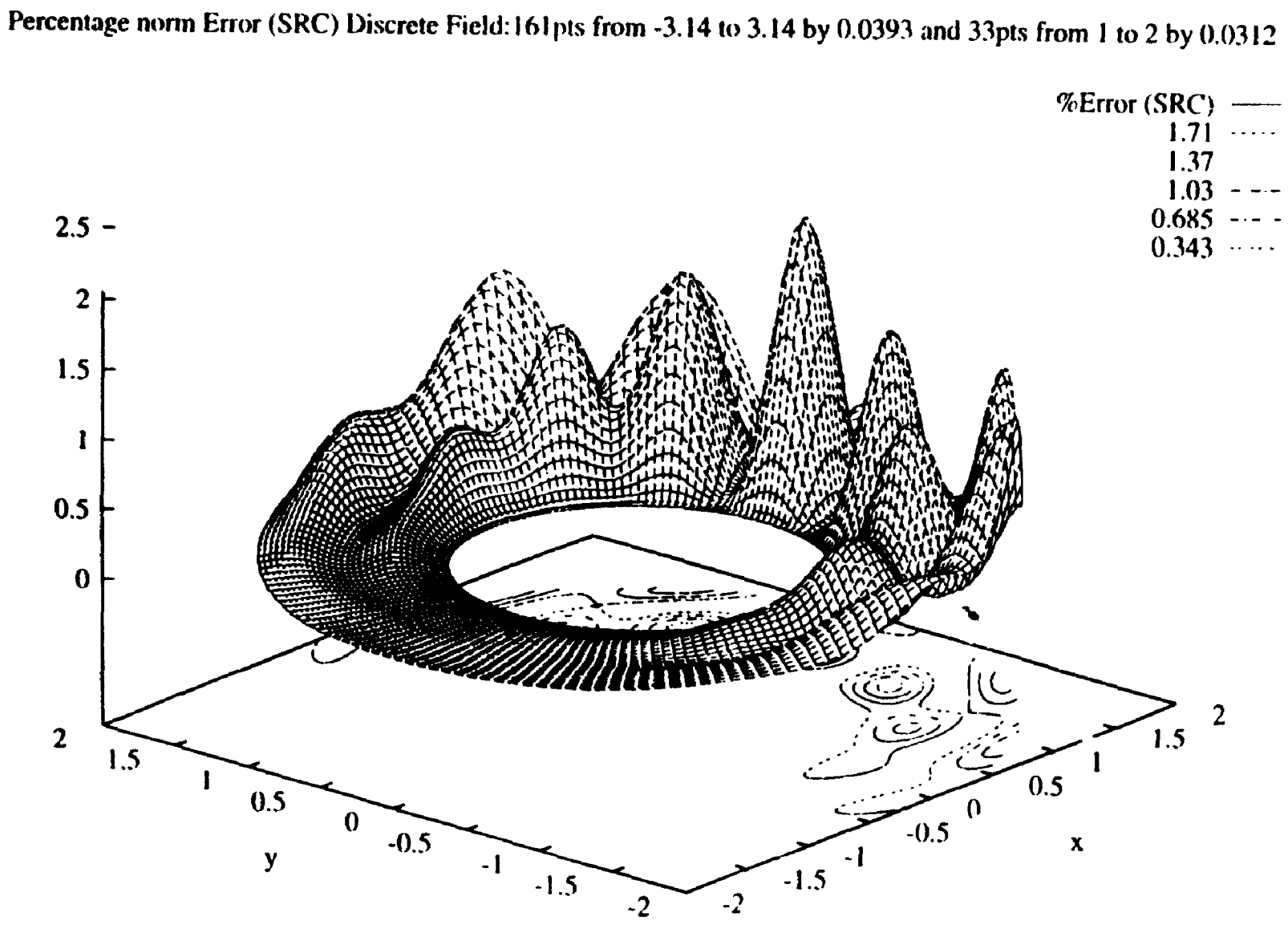
Percentage norm Error (SRC) Discrete Field:161pts from -3.14 to 3.14 by 0.0393 and 33pts from 1 to 2 by 0.0312
%Error (SRC)
1.71
1.37
1.03
0.685
0.343
2.5
2
1.5
1
0.5
0
y
x

Figure 4-6a)

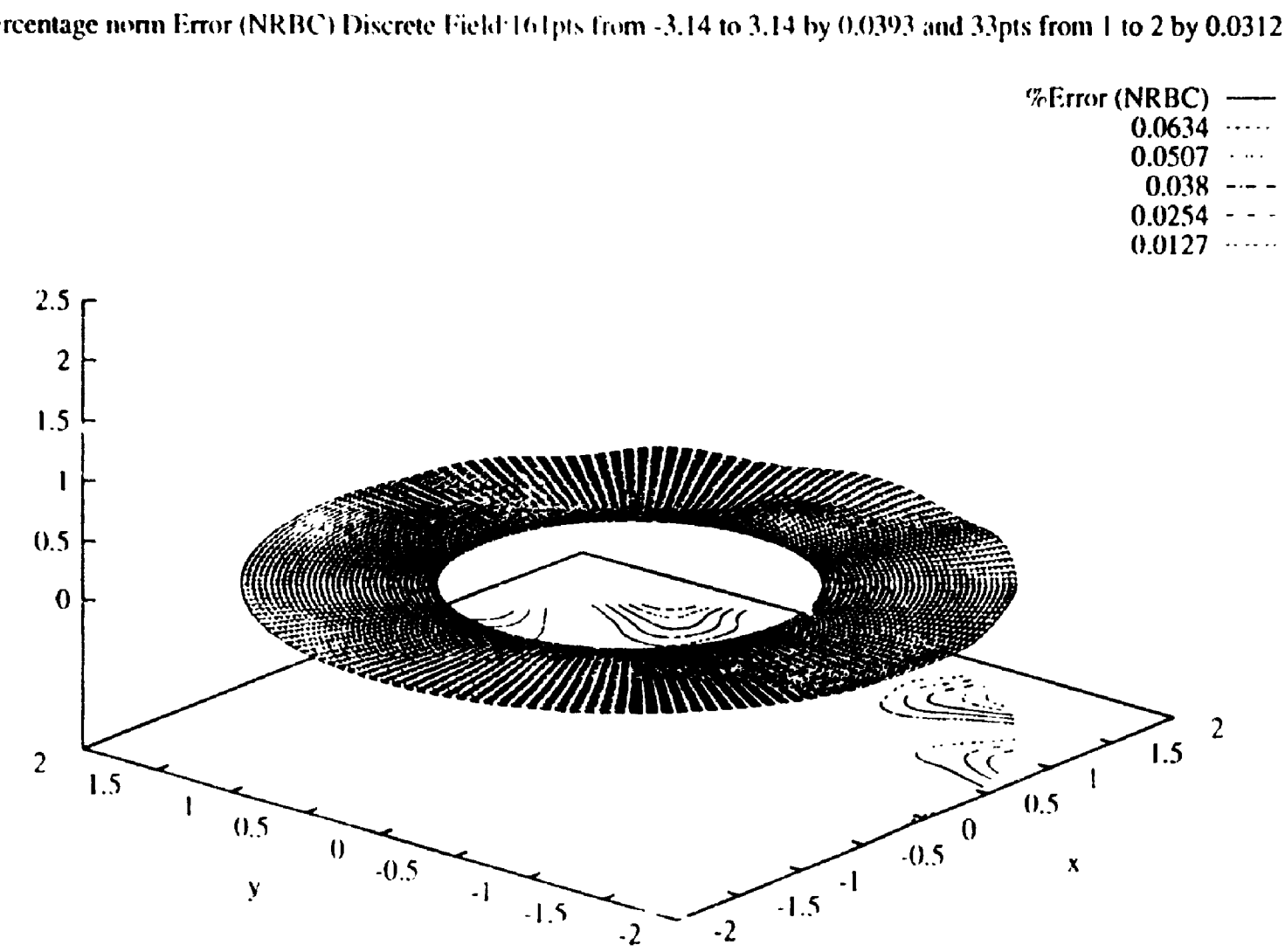

Figure 4-6b)

Figure 4-6. Percentage error in $\tilde{u}_s$ of the numerical solution using a) Sommerfeld radiation condition and b) non-reflecting boundary condition to approximate the boundary condition at infinity. The percentage error is calculated using $|u_s - \tilde{u}_s|/|u_s| \cdot 100\%$.

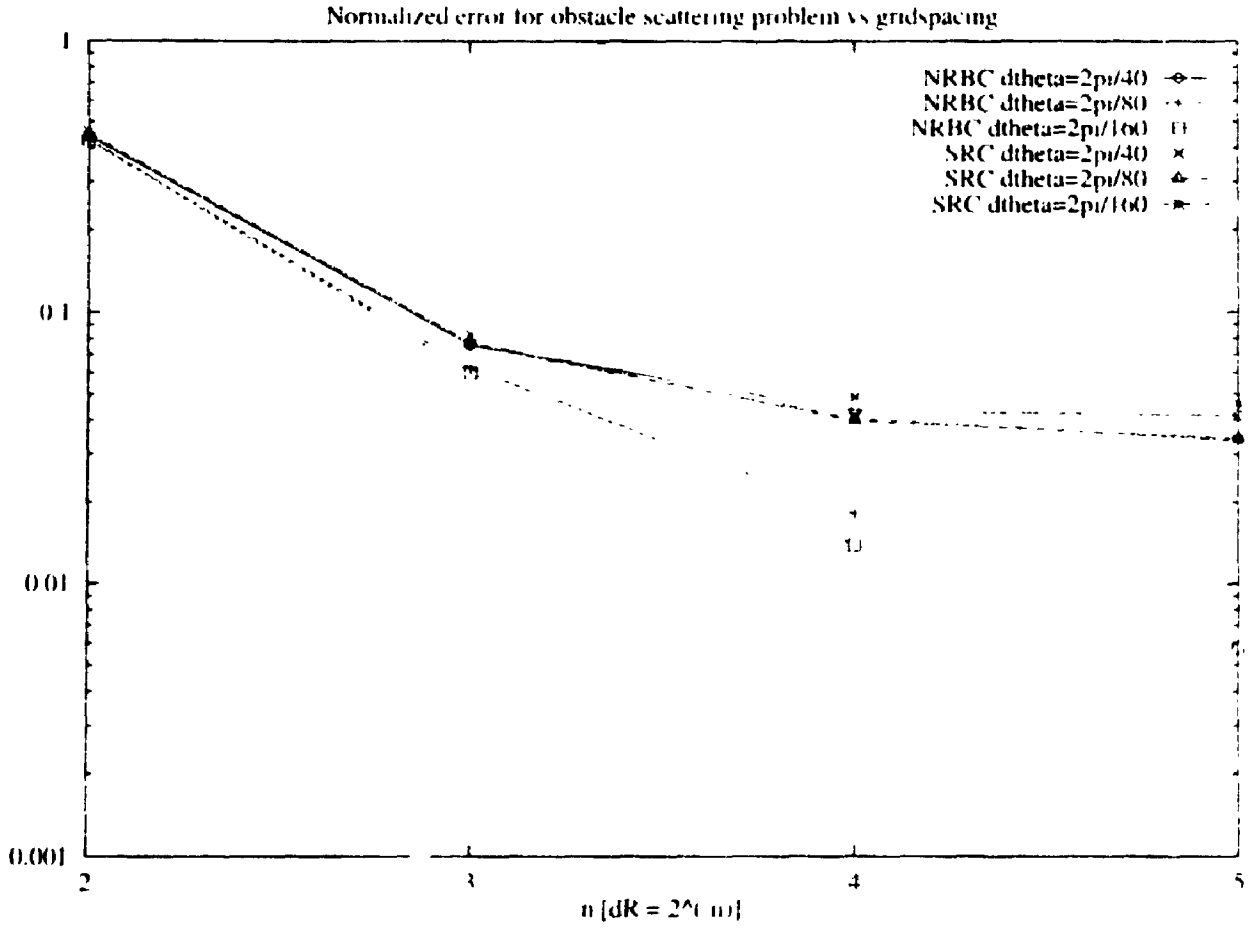

Figure 4-7. Error vs. gridspacing for both SRC and NRBC boundary conditions. The error measure is given by $\| u_s - \tilde{u}_s \|_{L_2} / \| 1 \|_{L_2}$. The normalization factor $\| 1 \|_{L_2}$ is include to allow for comparison of solutions on different size domains. The SRC formulation saturates as the gridspacing decreases. The NRBC method outperforms the SRC formulation for all grid spacings.

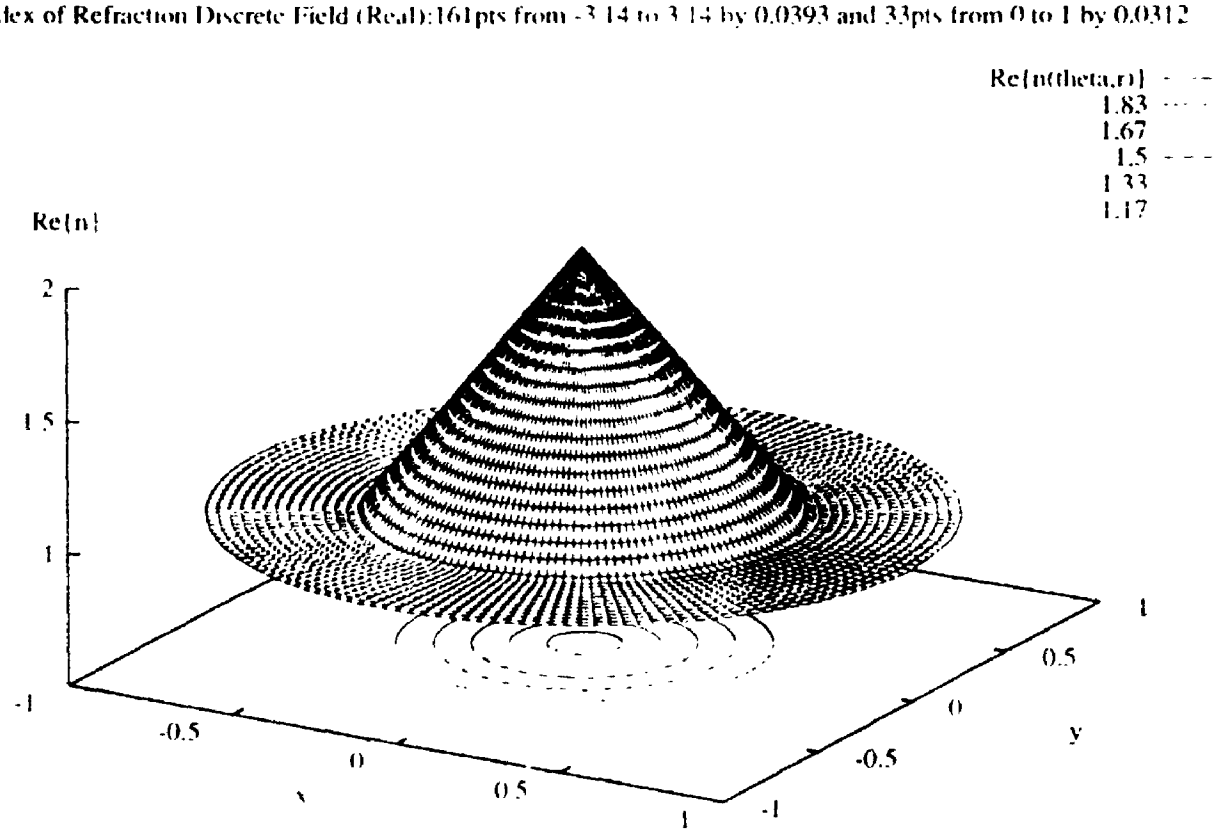

Figure 4-8. Real part of the sample index of refraction, $n(\theta, R)$ used to compare the PDE solution to the IE solution. The index of refraction was chosen such that $Im\{n(\theta, R)\} = 0$. The imaginary part can be used to model an absorbing medium.

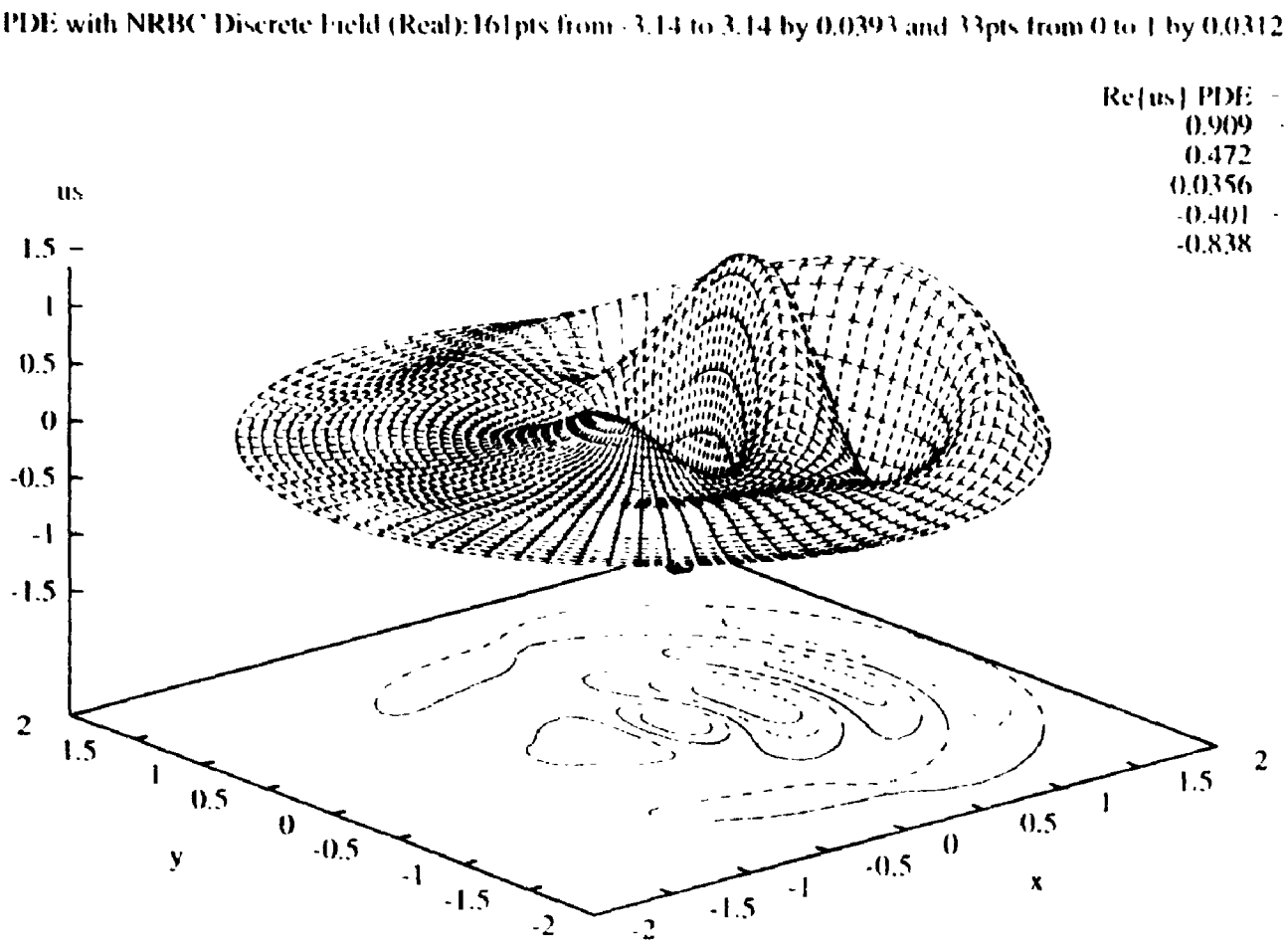
PDE with NRBC Discrete Field (Real): 161pts from -3.14 to 3.14 by 0.0393 and 33pts from 0 to 1 by 0.0312
Re{us} PDE
0.909
0.472
0.0356
-0.401
-0.838
us
1.5
1
0.5
0
-0.5
-1
-1.5
2
1.5
1
0.5
0
-0.5
-1
-1.5
-2
y
-2
-1.5
-1
-0.5
0
0.5
1
1.5
2
x

Figure 4-9a)

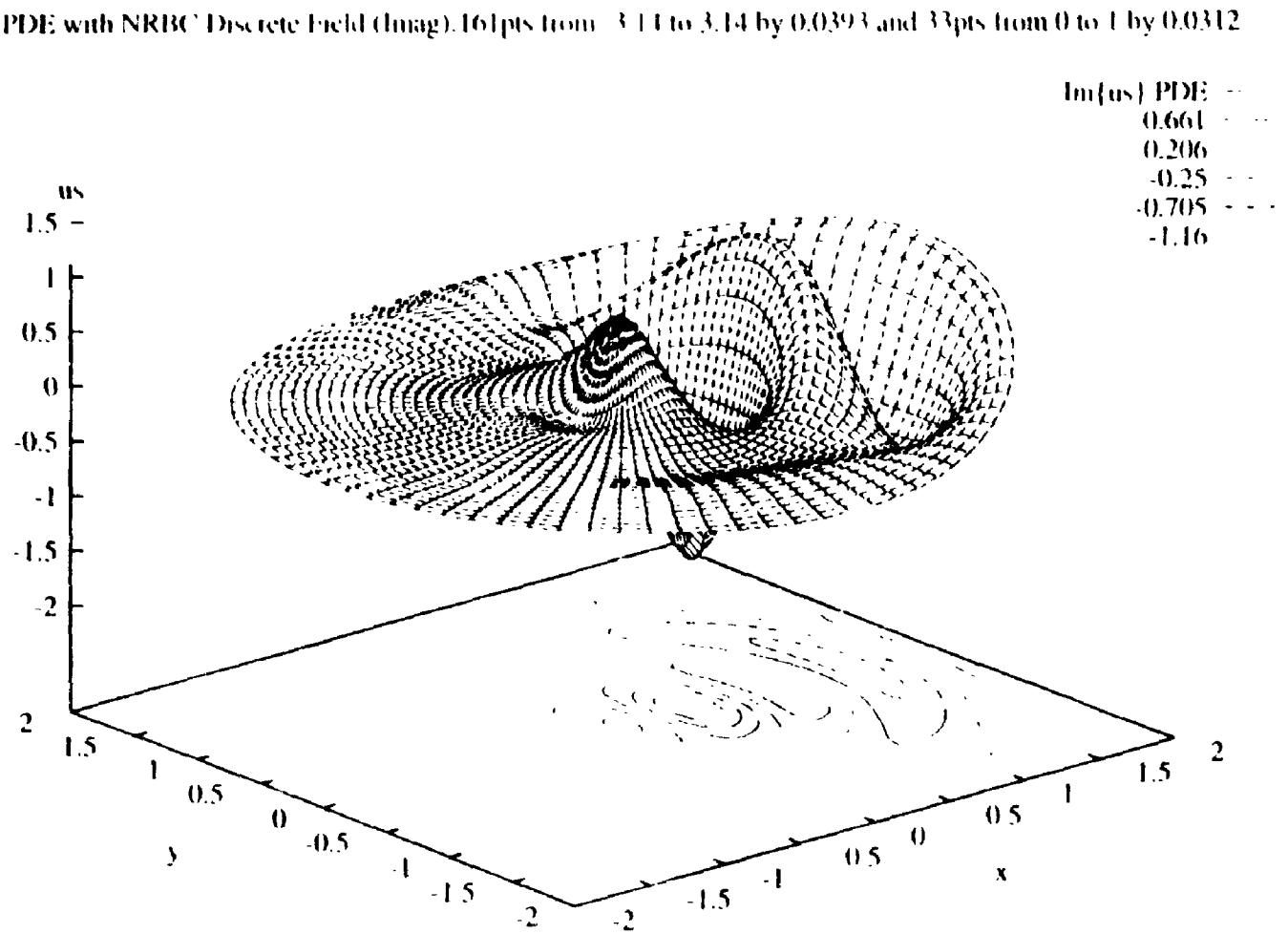

Figure 4-9b)

Figure 4-9. a) Real and b) imaginary part of the finite difference solution for the inhomogeneous medium using the partial differential equation formulation with non-reflecting boundary conditions. The index of refraction used was that of figure 4-8. Notice that the maximum amplitude waves are found for $\theta = 0$, which is in the wake of the medium.

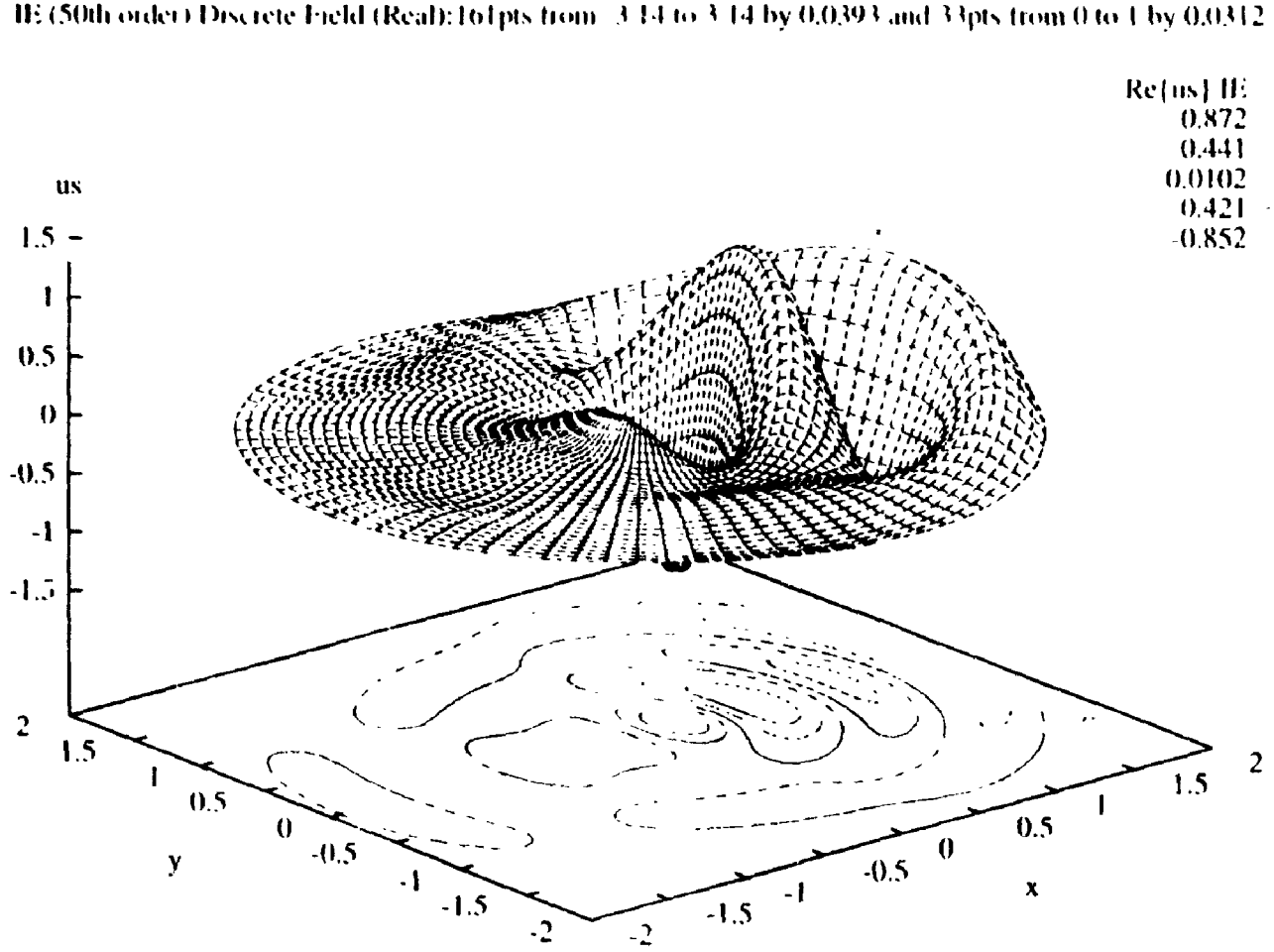
IE (50th order) Discrete Field (Real): 161pts from -3.14 to 3.14 by 0.0393 and 33pts from 0 to 1 by 0.0312
Re{us} IE
0.872
0.441
0.0102
-0.421
-0.852
us
1.5
1
0.5
0
-0.5
-1
-1.5
2
1.5
1
0.5
0
-0.5
-1
-1.5
-2
y
-2
-1.5
-1
-0.5
0
0.5
1
1.5
2
x

Figure 4-10a)

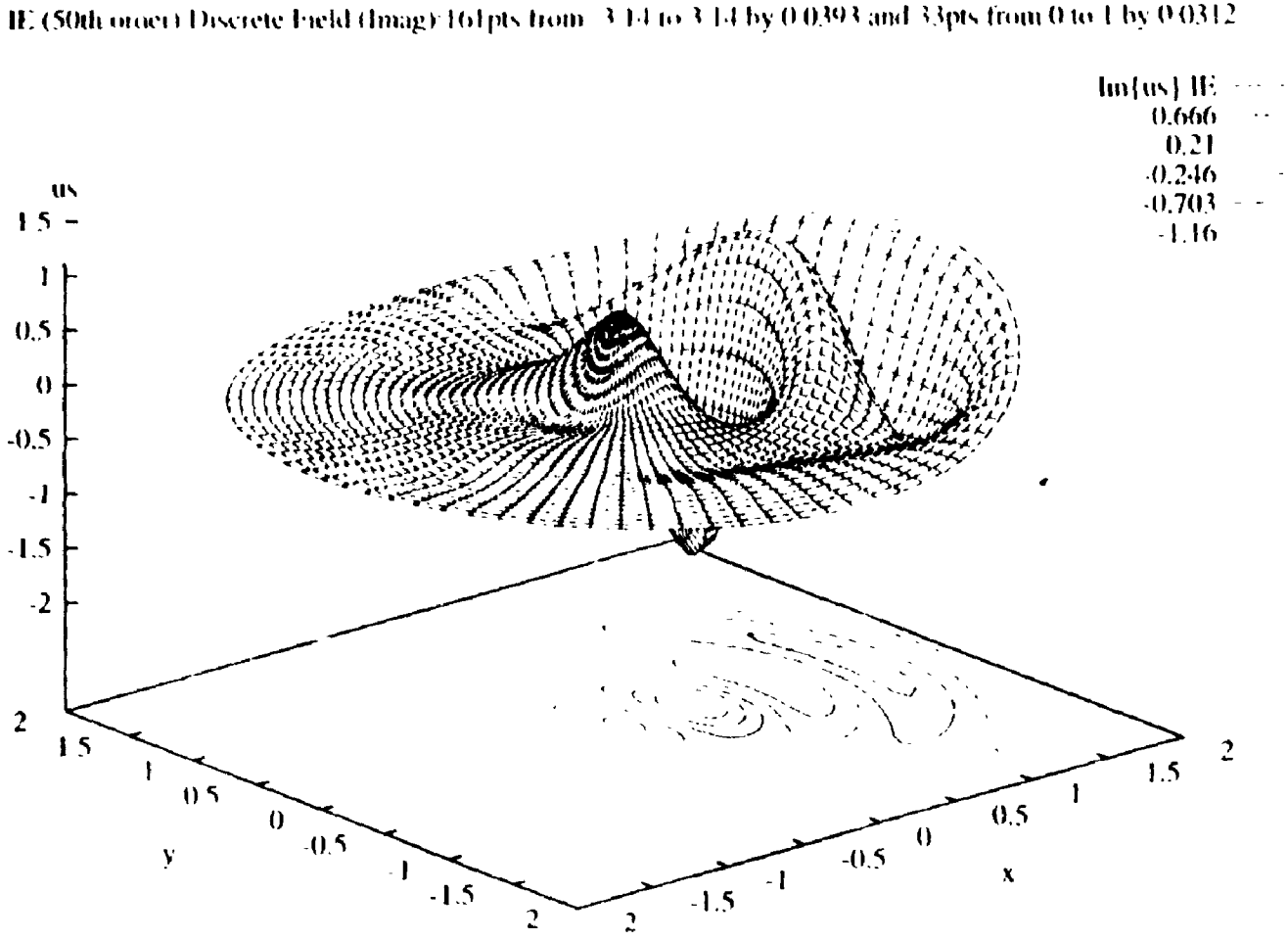

Figure 4-10b)

Figure 4-10. a) Real and b) imaginary part of the waves scattered by the inhomogeneous medium of figure 4-8. Solution was found using an integral equation with a 50th order Born approximation. The error estimate was $\| u^{(50)} - u^{(49)} \|_{L_2} < 10^{-5}$. This solution was assumed to be exact to provide a benchmark for the numerical solution of the associated PDE.

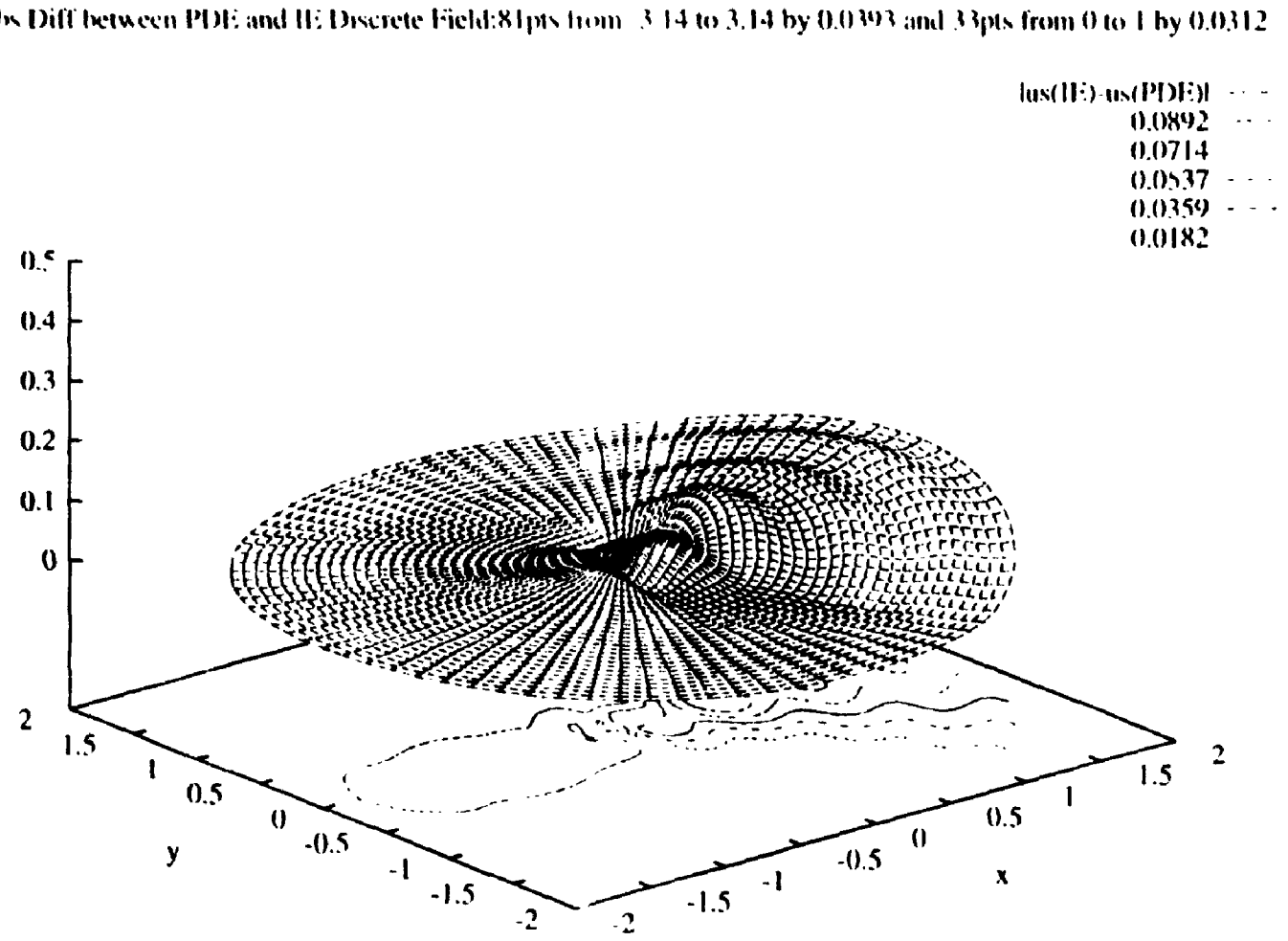

Figure 4-11. Absolute difference between the 50th order IE solution and the finite difference solution using NRBC given by $|u_s - \tilde{u}_s|^2$. The largest values occur on the centreline in the wake of the medium. The maximum percentage error in the wake occurs on the outer boundary where $|u_s - \tilde{u}_s| / |u_s| \cdot 100\% = 1.3\%$.

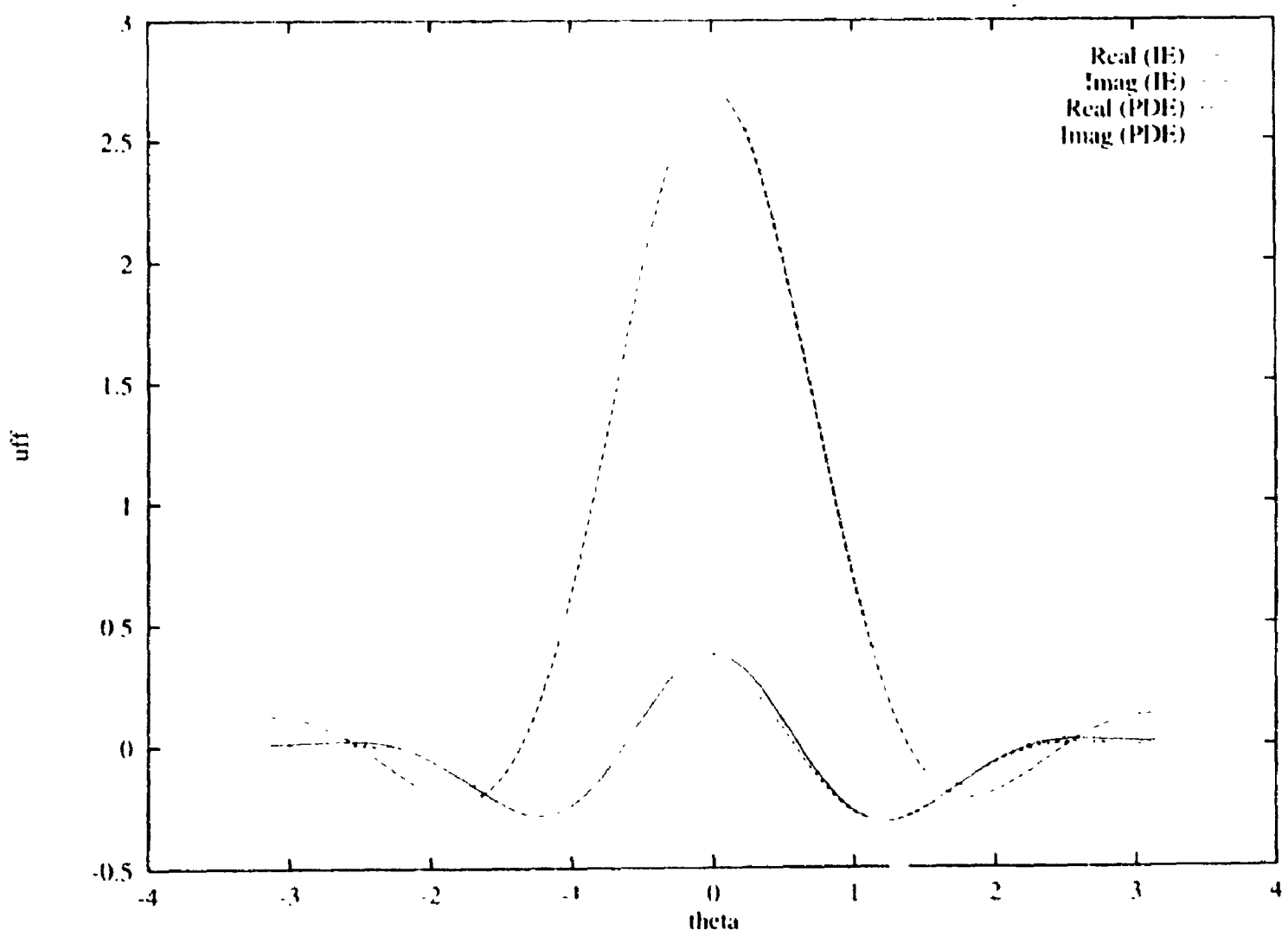

Figure 4-12. Far-field function corresponding to the conical cap in figure 4-8. The farfield is calculated by the 50th order IE solution and the finite difference solution of the PDE using NRBC. The PDE is solved on a 161x33 point grid. The far-field solution is given by the expression, $u_s(\theta, R) = \frac{e^{2\pi R}}{\sqrt{2\pi R}} u_{ff}(\theta) + O(1/R)$. This function is estimated using u_s at a finite distance $R_\infty = 20$.

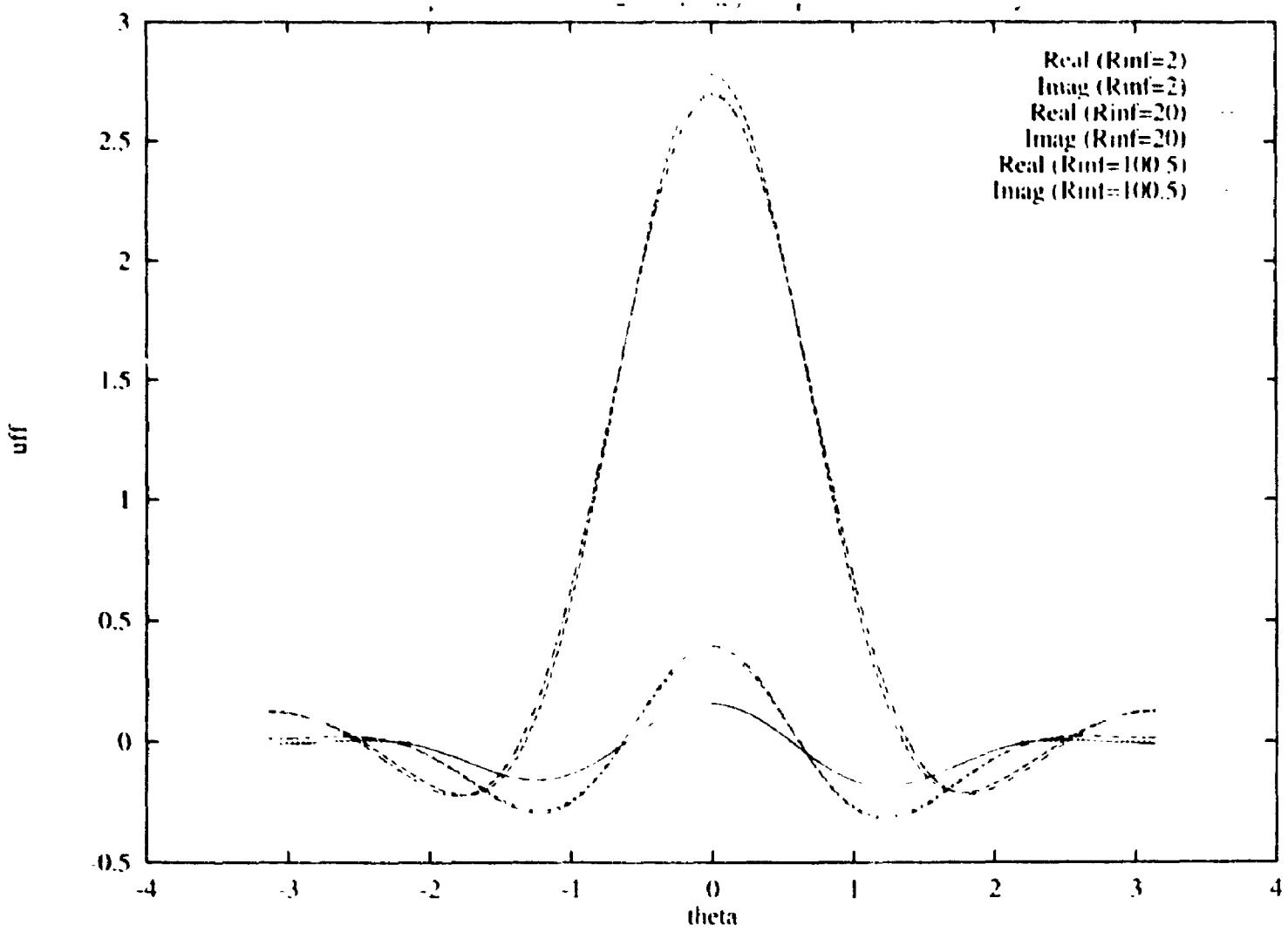

Figure 4-13. Far-field function for various values of R_∞. The function u_{ff} generated at $R_\infty = 2$ is significantly different than the far-field patterns computed for $R_\infty = 20, 100.5$. This indicates that the scattered wave at R=2 is not in the far-field. The far-field solutions were generated using a finite difference solution to the PDE with NRBC on a 161x33 point grid. The index of refraction which generated this pattern is the conical cap in figure 4-8.

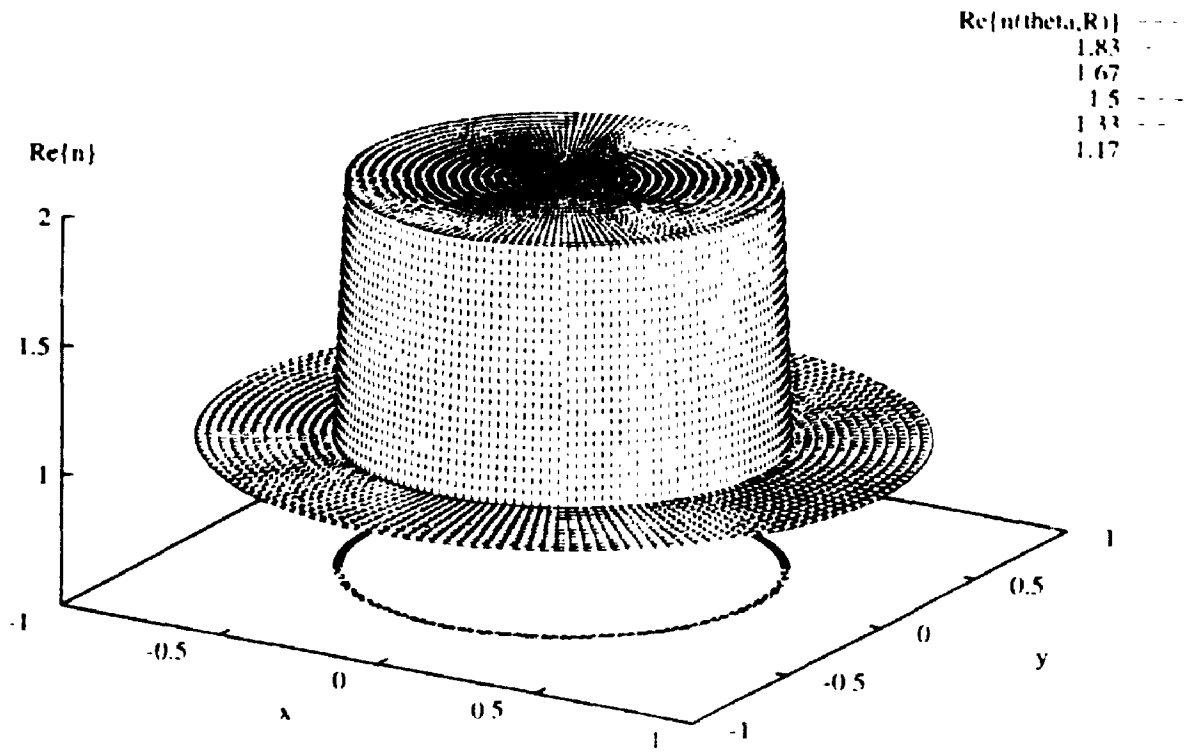

a)

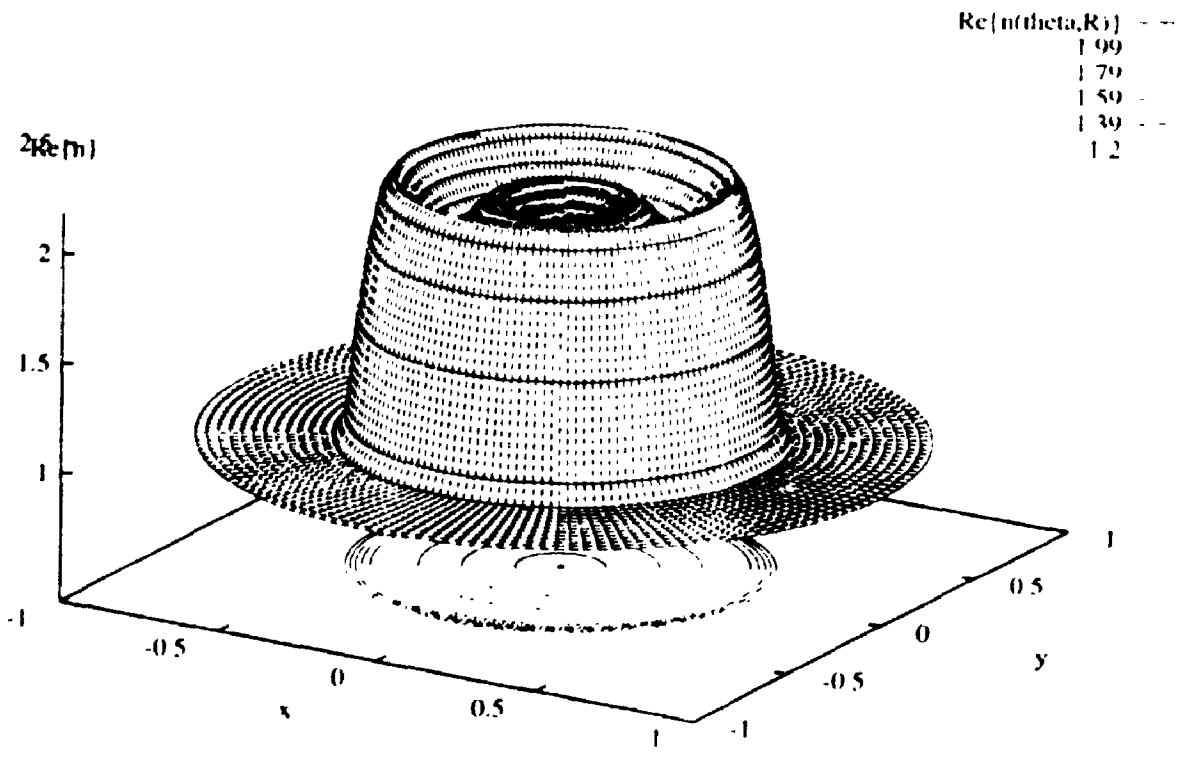

b)

Figure 4-14. a) Real part of the top hat function of example 4-2 used to test the reconstruction algorithm. While this function is axi-symmetric, it contains many high frequencies du to the sharp cut-off. b) Parameterization of the top hat using $L=0$ and $M=2$. Note the ringing in the function near the sharp edge.

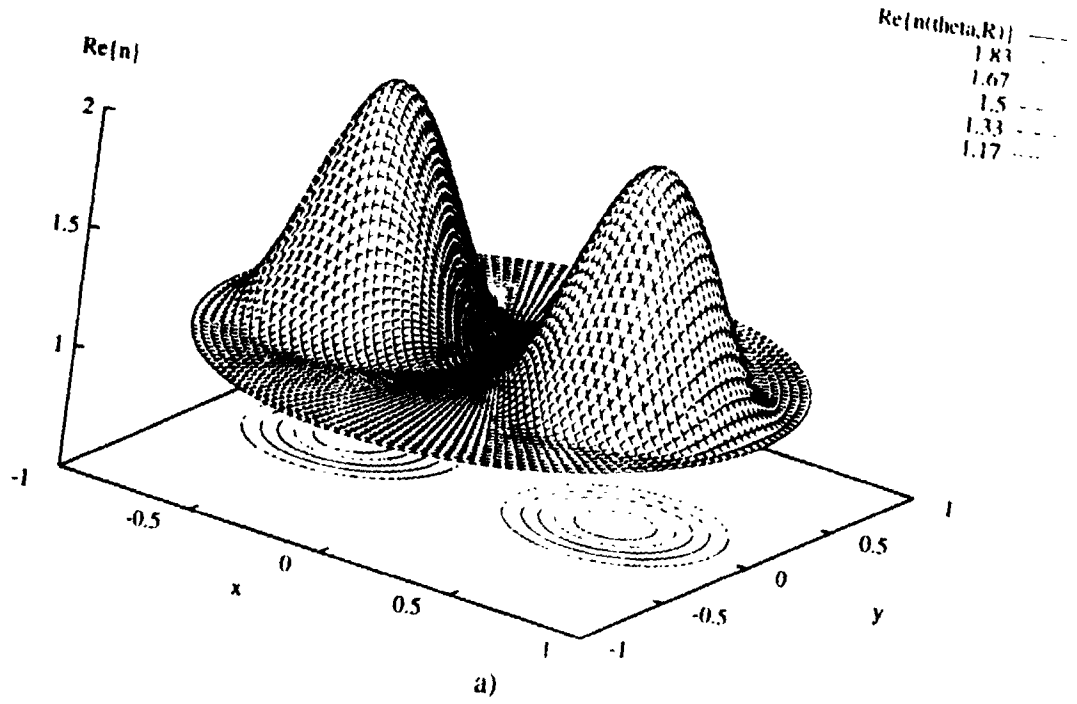

a)

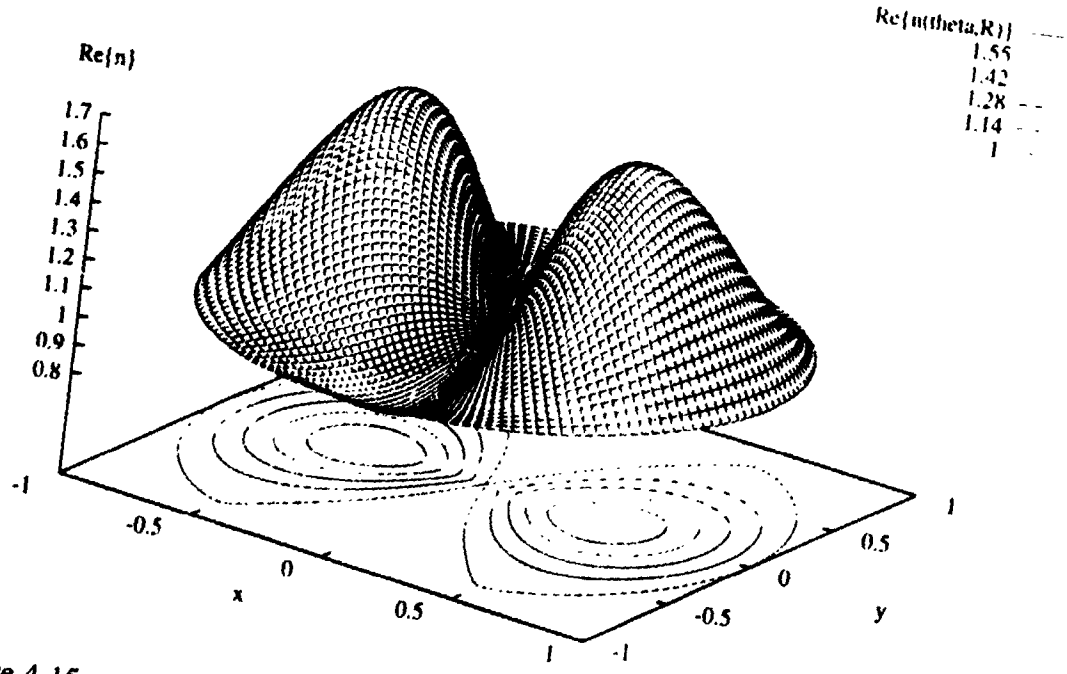

b)

Figure 4-15. a) Real part of the twin peaks index of refraction from example 4-3. This function is not axi-symmetric and will require several incident wave directions for the reconstruction. b) Parameterization of the function using $L=2$ and $M=2$.

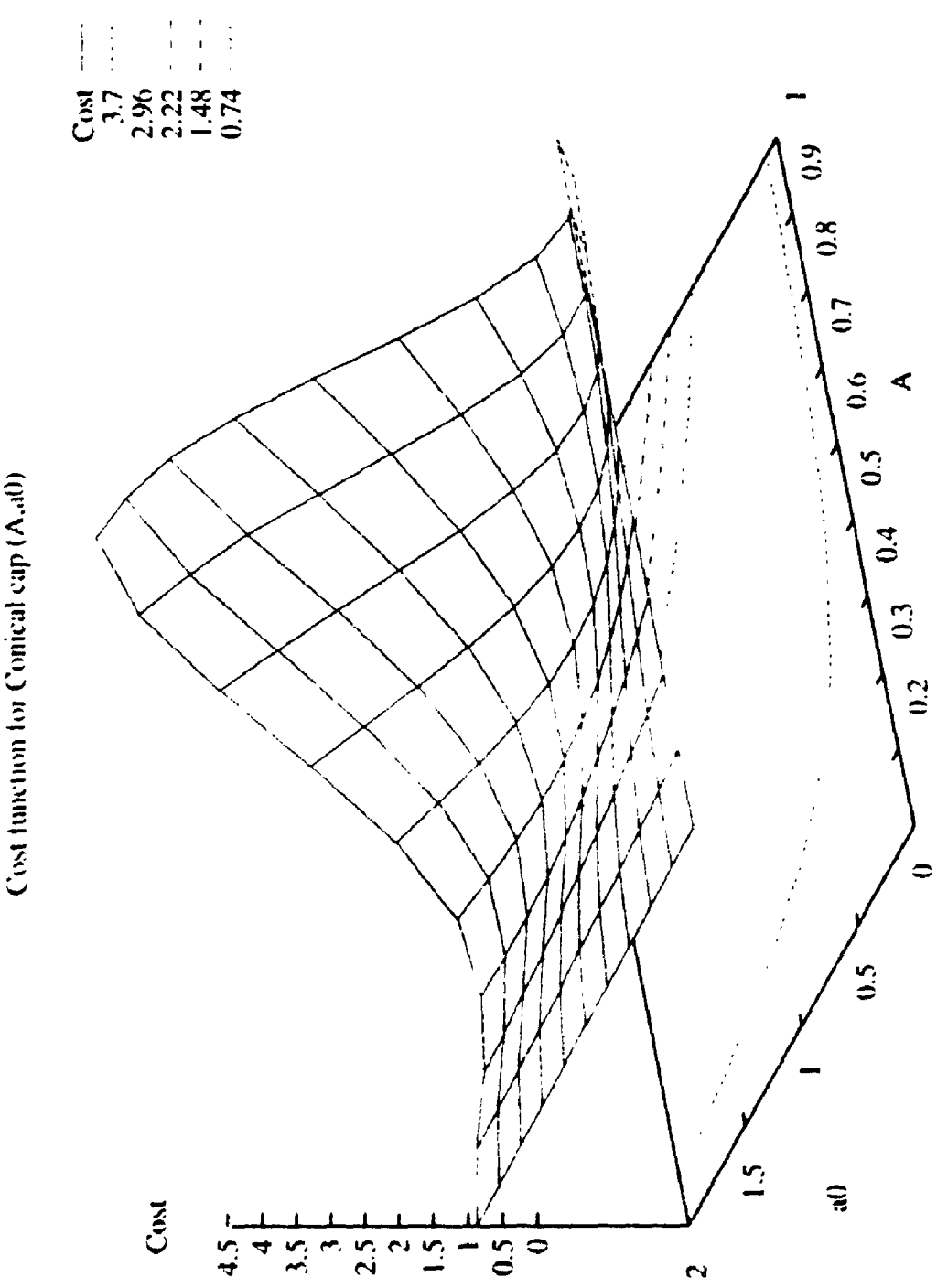
Cost function for Conical cap (A,a0)
Cost
3.7
2.96
2.22
1.48
0.74
Cost
4.5
4
3.5
3
2.5
2
1.5
1
0.5
0
2
1.5
1
0.5
0
a0
0.2
0.3
0.4
0.5
0.6
0.7
0.8
0.9
1
A

Figure 4-16a)

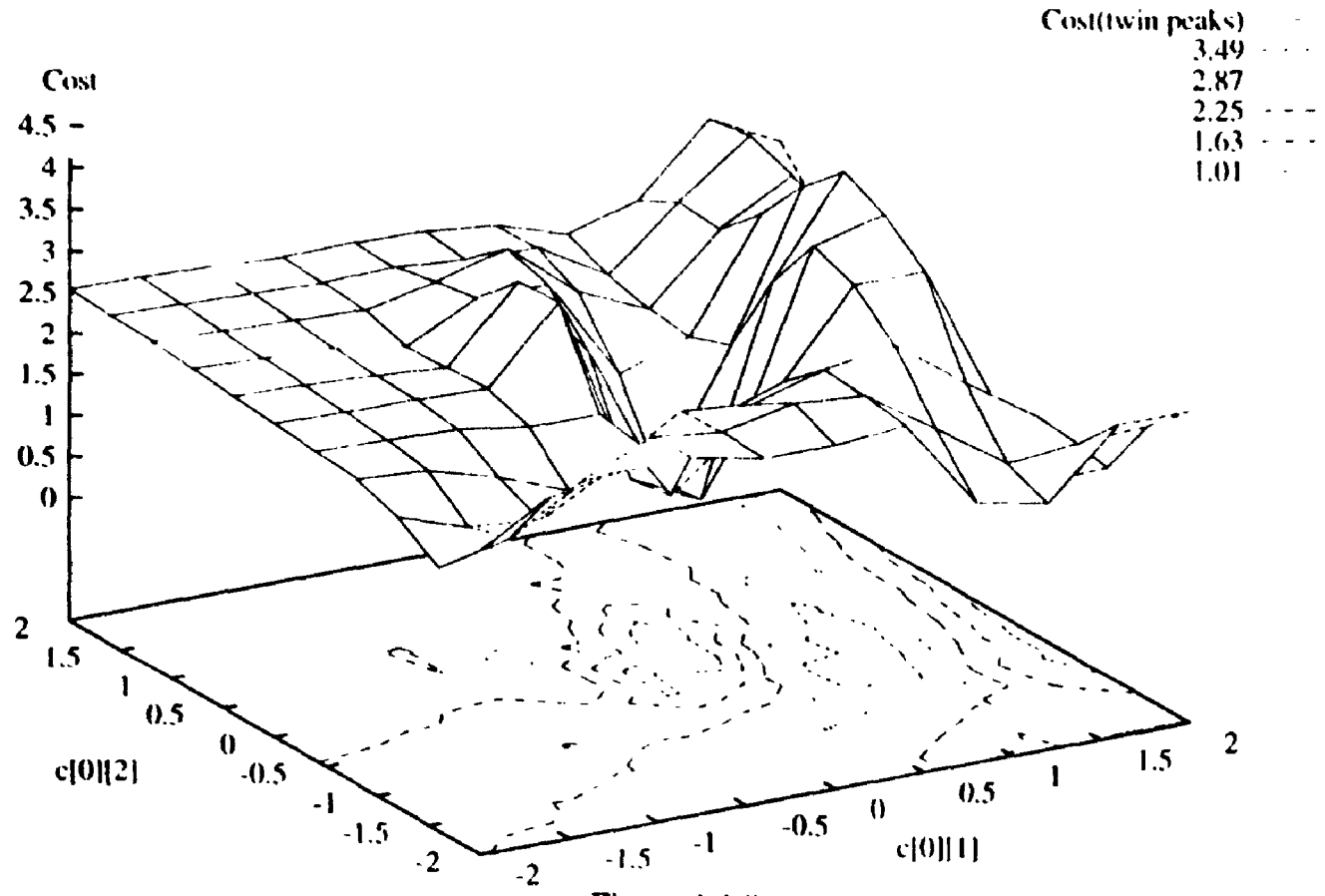

Figure 4-16b)

Figure 4-16. Cross-sections of the cost functions used for the reconstruction. These cross-sections are calculated about the point in parameter space which generates the theoretical global minimum based on the parameterization of the synthetic index of refraction. In a) the cost function for the conical cap of figure 4-8 vs. the parameters a_0 and A. This cost function is well behaved due to the simple nature of the index of refraction. In b) the cost function for the twin peaks of figure 4-14b) vs the parameters c_{01} and c_{02}. Notice the multimodal nature of this function. This fact makes it impossible for a gradient method to find a global minimum from all starting points. The cost function is $\sum_{\alpha}^{N_\alpha} \| u_{ff}^m - \hat{u}_{ff} \|$.

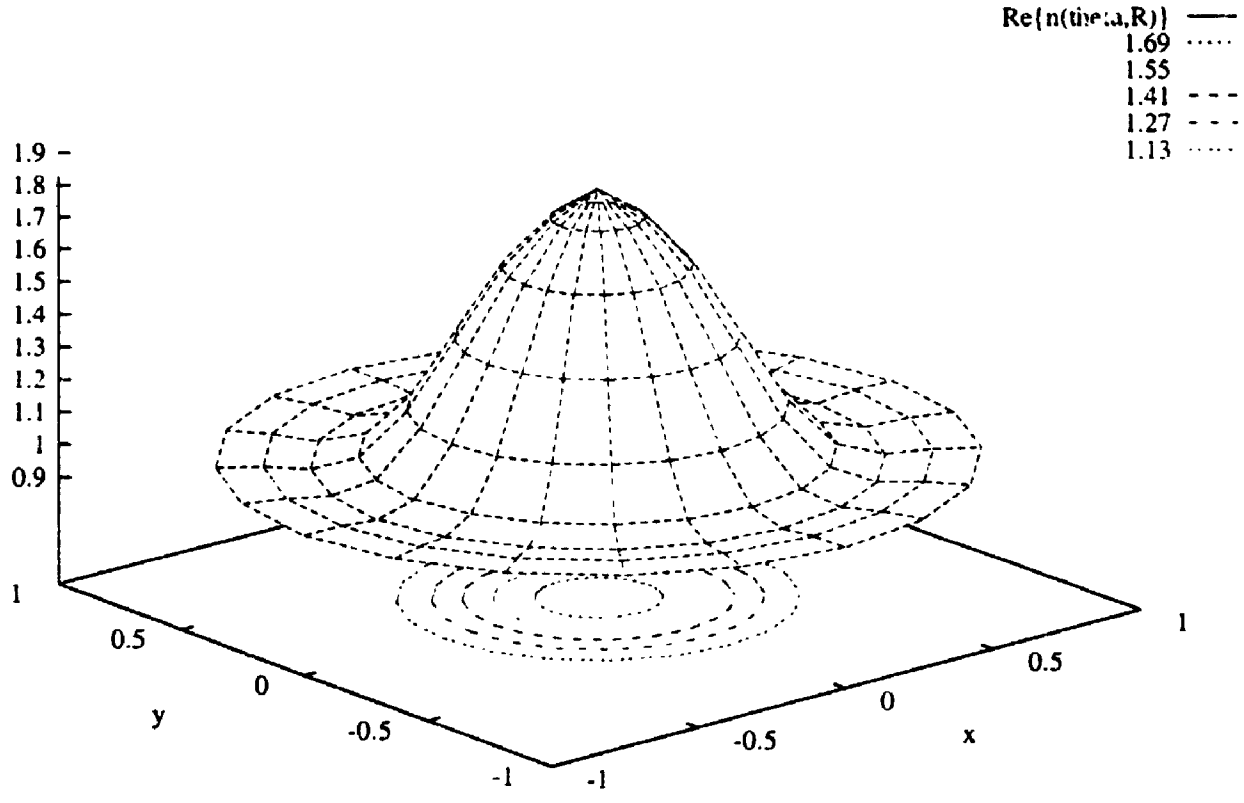

a)

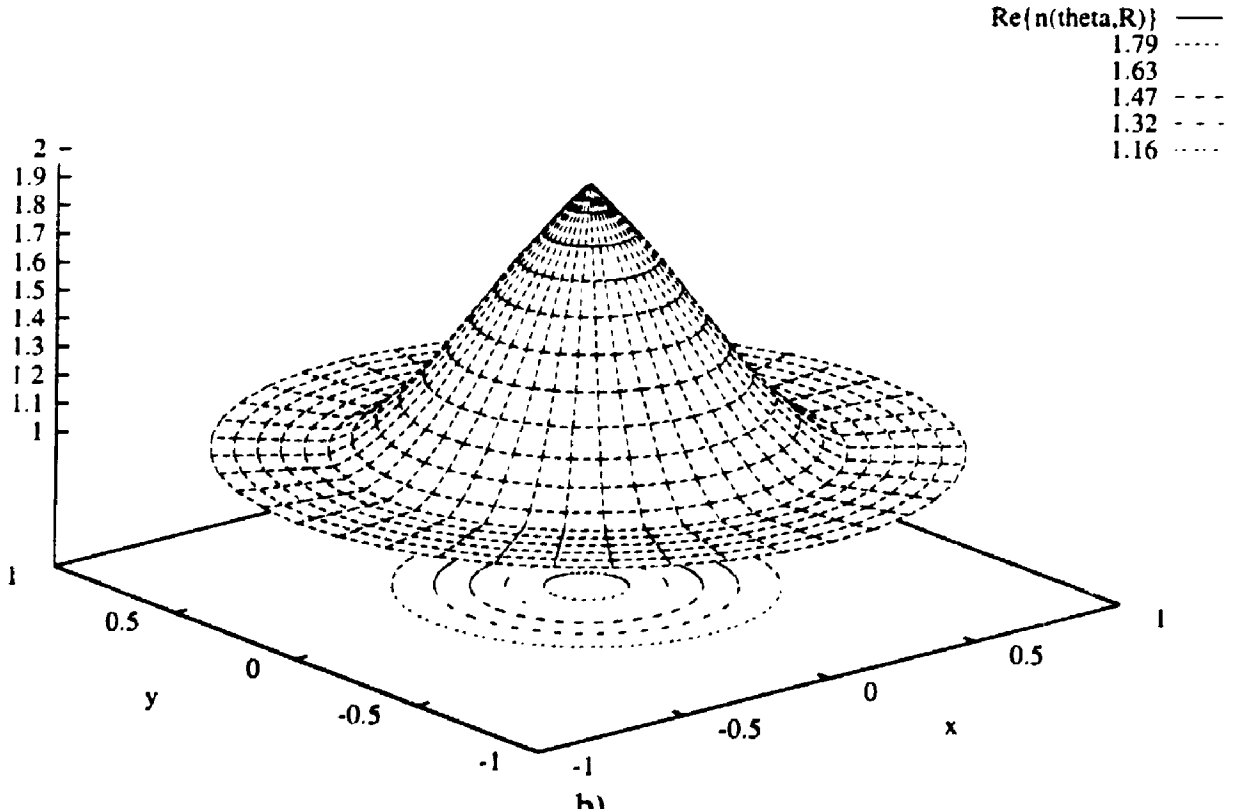

b)

Figure 4-17. Reconstructions of the index of refractions using the far-field data for the conical cap. One irradiation direction is used. The reconstruction is attempted with a function parameterized with $L=0$ and $M=2$. In a) a 21x9 point mesh gives a reconstruction error of 1.3%. In b) a 41x17 point mesh yields an error of 1.4%. The reconstruction in b) produces a sharper function. The reconstruction error is defined as $\|n-\tilde{n}\|/\|n\| \cdot 100\%$.

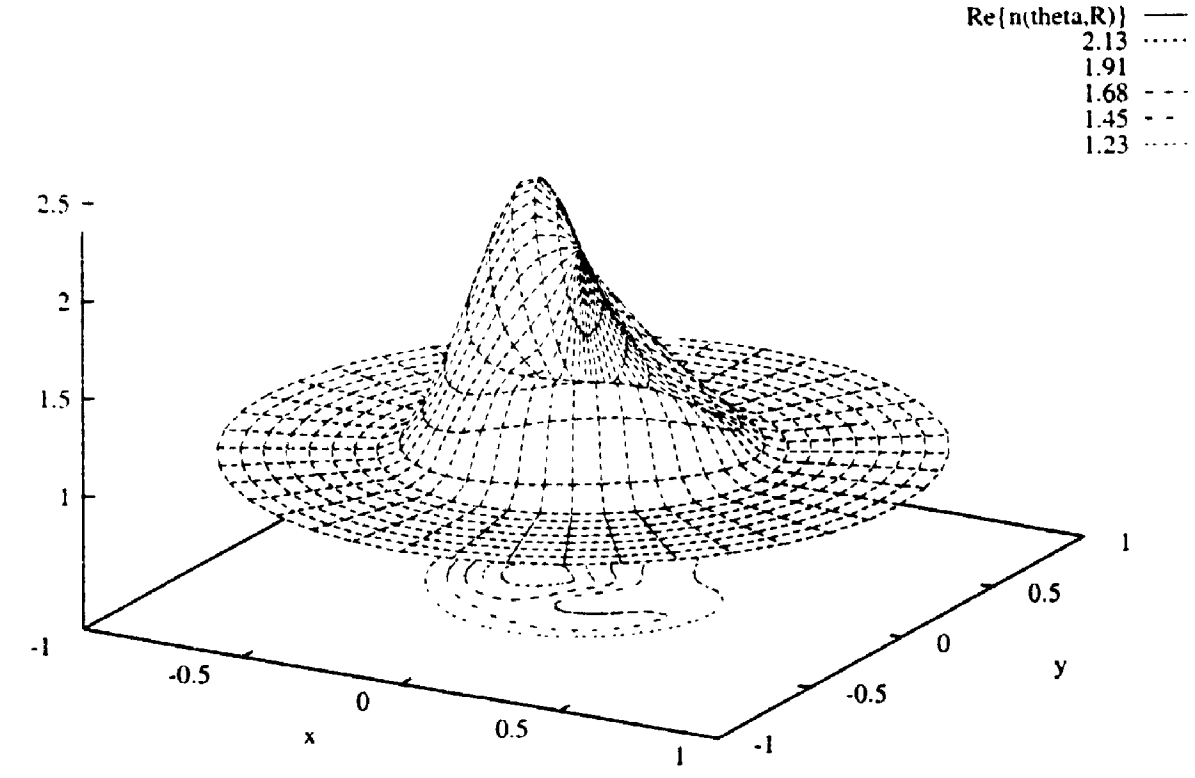

a)

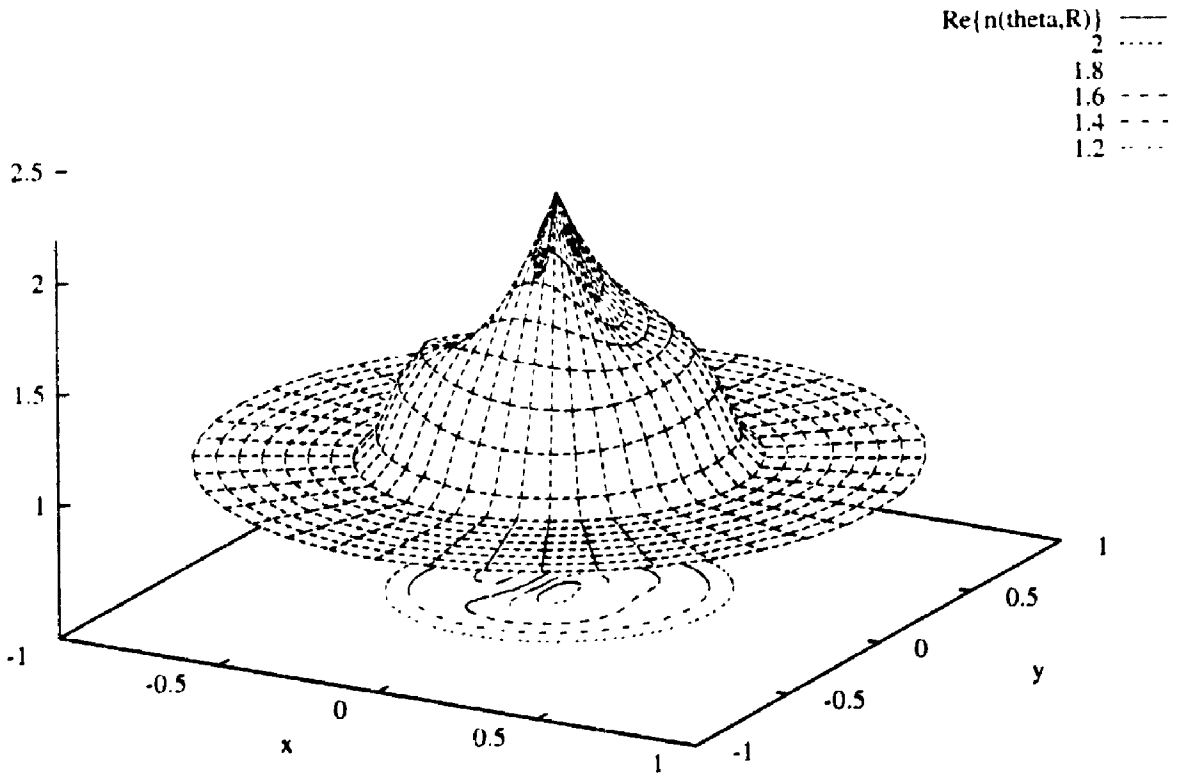

b)

Figure 4-18. Reconstructions of the index of refractions using the far-field data for the conical cap. One irradiation direction is used in a) giving a reconstruction error of 9.8%. In b) three incident wave directions are used to give an error of 4.4%. More than one wave direction is required because a non-axisymmetric parameterization of the index of refraction is used.

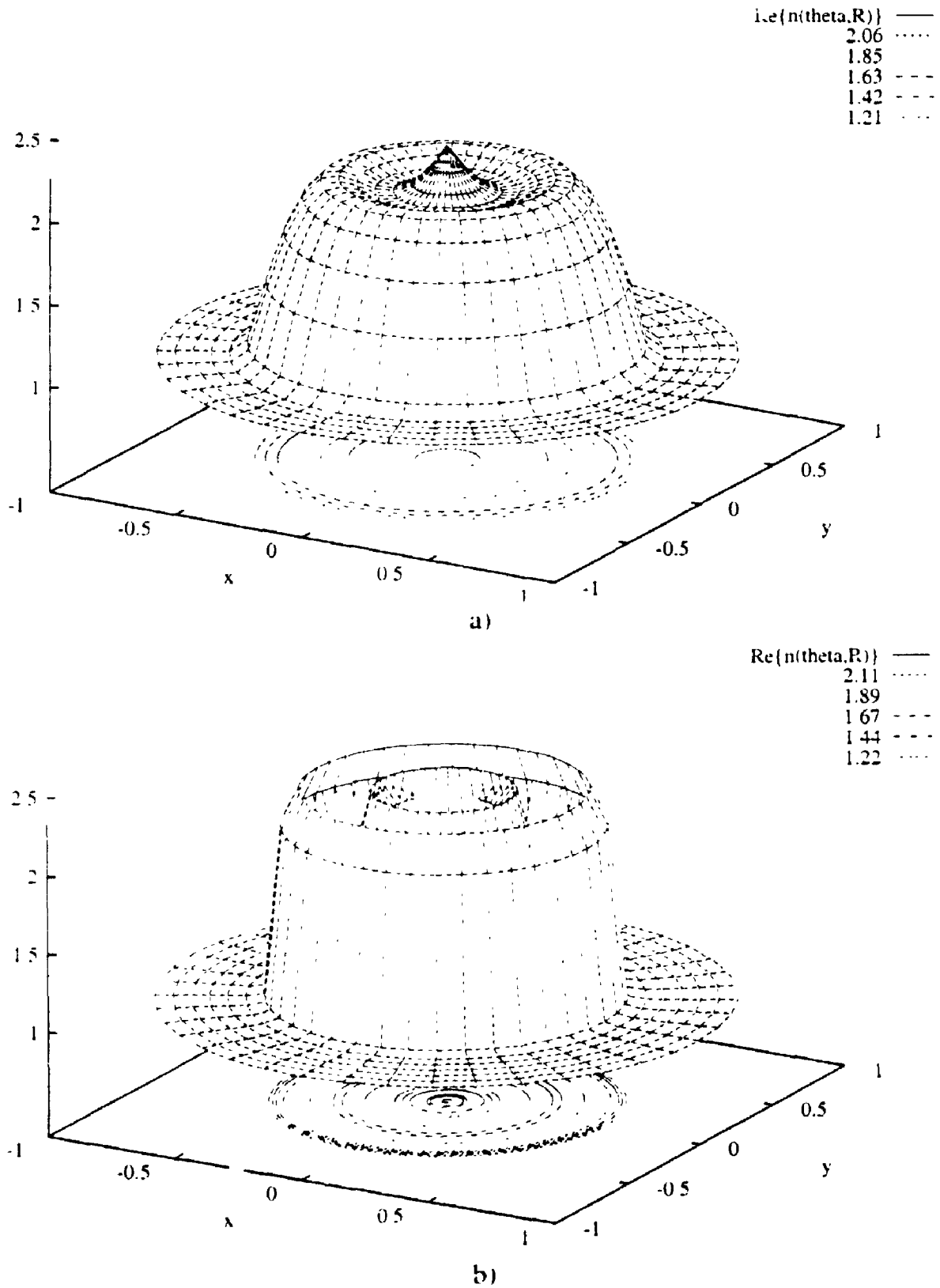

Figure 4-19. Reconstructions of the index of refractions using the far-field data for the top hat. One irradiation direction is used on a 41x17 grid. In a) 2 radial terms ($L=0, M=2$) in the Fourier series were used giving a reconstruction error of 9.2%. In b) 4 radial ($L=0, M=4$) terms in the Fourier series were used giving a reconstruction error of 9.9%. In this case, more terms do not reduce the reconstruction error but they do sharpen the profile.

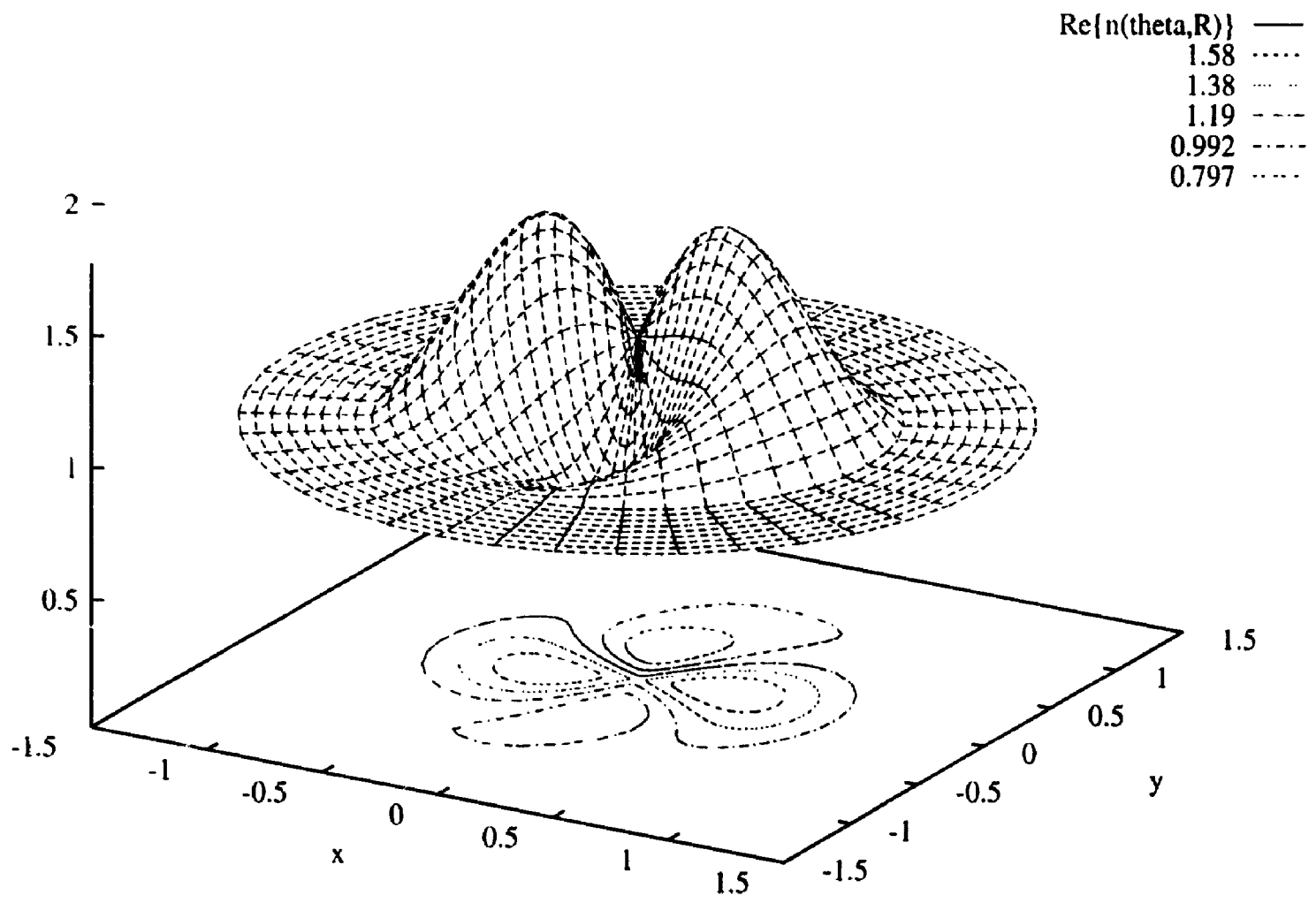

Figure 4-20. Reconstructions of the index of refractions using the far-field data for the twin peaks of example 4-3. For (L=2,M=2) with nine irradiation directions the reconstruction error was 9.2%.

CHAPTER 5

Conclusions

5.1 Current Work

The quasi-solutions technique yields a workable way to solve ill-posed inverse problems provided that one has a reasonable parameterization of the solution space based on the physics of the problem. Existence and uniqueness are guaranteed by this method. Only the stability of the solutions need be considered. Regularization of the problem provides the required stability. There is a compromise of course between stability and accuracy. Strong regularization of the problem provides stability but reduces accuracy. The simulated annealing algorithm applied to the cost function formulated by the quasi-solution performed reasonably well at selecting out the global minima from numerous local minima. However, the simulated annealing minimization requires numerous function evaluations. For this reason, it is imperative to have a fast, efficient, and accurate solution to the forward problem.

The inversion algorithm was successfully applied to two inverse problems motivated by physical situations. The associated direct problem of both examples were open domain problems which require special techniques to be solved numerically. Finite difference expansions were used to approximate the derivatives in both cases. The infinite boundary conditions for the electrostatic potential problem were approximated using a Robbin condition on the boundary. This boundary condition is a local condition. The second example solved Helmholtz's equation with non-reflecting boundary conditions to approximate the Sommerfeld radiation condition. This is a global boundary condition. Successful reconstructions were performed in both examples using synthetically generated data. The inverse conductivity problem included inversion with random uniform noise added to the synthetic data.

5.2 Future Work

An obvious extension to the mise-à-la-masse inversion algorithm is to test it with experimentally measured data. This would be a true test of the usefulness of the proposed inversion method. In the inverse acoustic scattering problem more incident wave directions

maybe with multiple frequencies would provide better resolution of the inhomogenous medium. In addition, the simulated annealing algorithm while able to deal with multimodal cost functions does not economize on function evaluations. Each function evaluation is quite costly when fine grids and numerous incident wave directions are used. It would be worthwhile exploring the use of other minimization techniques. Even a combination of minimization algorithms could prove useful. For example, one could use simulated annealing to perform a rough exploration of the cost function to find some valleys which may contain the global minimum. Then the depth of each valley could be explored using a traditional gradient method.

I was allowed the pleasure, in the discourse of this work, of sampling many areas of research. The field of inverse problems is intimately connected to the fields of integral equations, partial differential equations, numerical analysis and functional analysis as well as many applied sciences such as geophysics and medical biophysics. For inverse problems: I have gained an appreciation for them as well as a respect for them, while inspired by them I do remain humbled by them.

REFERENCES

1. E. Aarts and J. Korst, "Simulated Annealing and Boltzmann Machines". (John Wiley & Sons Ltd. 1989).

2. R. Barrett, M. Berry, T. Chan, J. Demme, J. Donato, J. Dongarra, V. Eijkhout, R. Pozo, C. Romine and H. van der Vorst "Templates for the solution of linear systems: Building Blocks for Iterative Methods" (SIAM, Philadelphia, 1994).

3. A. Bayliss, M. Gunzburger and E. Turkel, Boundary Conditions for the Numerical Solution of Elliptic Equation in Exterior Regions, *SIAM J Appl Math* **42(2)** (1982) 430-451.

4. C.W. Beasley and S.H. Ward, Three-dimensional mise-à-la-masse modeling applied to mapping fracture zones. *Geophysics* **51(1)** (1986) 98-113.

5. A. Binder, H.W. Engl et al, Weakly closed non-linear operators and parameter identification in parabolic equatations by Tikhonov regularization, *Institutsbericht No. 444* University of Linz, (1991).

6. I.O. Bohachevsky, M.E. Johnson and M.L. Stein, Generalized Simulated Annealing for Function Optimization. *Technometrics* **28(3)** (1986) 209-217.

7. R.P. Brent, "Algorithms for Minimization without Derivatives". (Prentice-Hall Inc: Englewood Cliffs, NJ, 1973).

8. M.A. Brodsky, On the uniqueness of the inverse potential problem for homogeneous polyhedrons. *SIAM J Appl Math* **46(2)** (1986) 345-350.

9. S. Clift, P.A. Forsyth and J.R. Knightley, *Watsit* Sparse Matrix Solver User Guide, Private Communication.

10. D. Colton and R. Kress, "Inverse Acoustic and Electromagnetic Scattering Theory" (Springer-Verlag: New York 1992).

11. D. Colton and P. Monk, The numerical solution of an inverse scattering problem for acoustic waves, *IMA J App Math* **49** (1992) 163-184.

12. A. Corana, M. Marchesi, C. Martini and S. Ridella, Minimizing Multimodal Functions of Continuous Variables with the "Simulated Annealing" Algorithm, *ACM Trans. on Mathematical Software* **13(3)** (1987) 262-280.

13. A. Dey and H.F. Morrison, Resistivity modeling for arbitrarily shaped three-dimensional structures, *Geophysics* **44(4)** (1979) 753-780.

14. D.C. Dobson, Convergence of a reconstruction method for the inverse conductivity problem, *SIAM J Appl Math* **52(2)** (1992) 442-458.

15. G. Dueck and T. Scheuer, Threshold Accepting: A General Purpose Optimization Algorithm Appearing Superior to Simulated Annealing, *J Comp Phys* **90** (1990) 161-175.

16. E. Eloranta, A method for calculating mise-à-la-masse anomalies in the case of high conductivity contrast by the integral equation technique, *Geoexploration* **22** (1984) 77-88.

17. B. Engquist and A. Majda, Absorbing Boundary Conditions for the Numerical Simulation of Waves, *Math Comp* **31(139)** (1977) 629-651.

18. P.A. Forsyth and J.R. Knightley, *Mat1* User Guide, Private Communication.

19. S. Geman and D. Geman, Stochastic relaxation, Gibbs distributions, and the Bayesian restoration of images, *IEEE Trans Pattern Analysis and Machine Intelligence* **PAMI-6(6)** (1984) 721-741.

20. D. Givoli, Non-reflecting Boundary Conditions, *J Comp Phys* **94** (1991) 1-29.

21. C.I. Goldstein, The Finite Element Method with Non-Uniform Mesh Sizes Applied to the Exterior Helmholtz Problem, *Numerische Mathematik* **38** (1981) 61-82.

22. C.W. Groetsch, "Inverse Problems in the Mathematical Sciences" (Braunschweig; Wiesbaden: Vieweg, 1993).

23. S. Gutman and M. Klibanov, Iterative method for multi-dimensional inverse scattering problems at fixed frequencies, *Inverse Problems* **10** (1994) 573-599.

24. J. Hadamard, Sur les Problemes aux Derivees Partielles et leur Signification Physique, *Bull. Univ. Princeton* **13** (1902) 49.

25. K.I. Hopcraft and P.R. Smith, "An Introduction to Electromagnetic Inverse Scattering" (Kluwer Academic Publishers: Boston, 1992).

26. V. Isakov and J. Powell, On the Inverse Conductivity Problem with One Measurement. *Inverse Problems* **6** (1990) 311-318.

27. K.V. Ivanov, Integral equations of the first kind and an approximate solution. *Soviet Math Doklady* **3** (1962) 210-212.

28. K.V. Ivanov, On linear problems which are not well-posed. *Soviet Math Doklady* **3** (1962) 981-983.

29. D.S. Jones, "Acoustic and Electromagnetic Waves" (Oxford University Press: New York, 1986).

30. J.B. Keller, D. Givoli, Exact Non-reflecting Boundary Conditions, *J Comput Phys*, **82(1)** (1989) 172-192.

31. S. Kirkpatrick, C.D. Gelatt, Jr. and M.P. Vecchi, Optimization by Simulated Annealing, *Science* **220** (1983) 671-680.

32. R.E. Kleinman and P.M. van den Berg, A modified gradient method for two-dimensional problems in tomography, *J Comp App Math* **42** (1992) 17-35.

33. N. Metropolis, A. Rosenbluth, M. Rosenbluth, A. Teller and E. Teller, Equation of state calculations by fast computing machines, *J Chem Phys* **21** (1953) 1087-1092.

34. P.M. Morse and H. Feshbach, "Methods of Theoretical Physics: II" (McGraw-Hill: New York, 1953).

35. D.J. Moseley, H. Rasmussen and P.A. Forsyth, Three dimensional inversion scheme for mise-à-la-masse prospecting data using simulated annealing, *Can App Math Quart* (to appear).

36. C.J. Mwenifumbo, Intepretation of mise-à-la-masse data for vein type bodies, Ph.D. Thesis, Univ. of Western Ontario, London (1980).

37. A. Nachman, Reconstructions from boundary measurements, *Annals of Math* **128** (1988) 531-576.

38. A. Neubauer, Tikhonov regularization for non-linear ill-posed problems: optimal convergence rates and finite dimensional approximation, *Inverse Problems* **5** (1989) 541-547.

39. R.L. Parker, The Inverse Problem of Resistivity Sounding, *Geophysics* **49(12)** (1984) 2143-2158.

40. R.L. Parker and K.A. Whaler, Numerical methods for establishing solutions to the inverse problem of electromagnetic induction, *J Geophy Res* **86(10)** (981) 9574-9584.

41. A.G. Ramm, Recover of the potential from fixed energy scattering data, *Inverse Problems* **4** (1988) 877-886.

42. A.G. Ramm, "Multidimensional inverse scattering problems" (Longman Scientific & Technical: New York, 1992).

43. O. Scherzer, H.W. Engl and K. Kunisch, Optimal a posteriori parameter choice for Tikhonov regularization for solving nonlinear ill-posed problems, *SIAM J Num Anal* **30(6)** (1993) 1796-1838.

44. C. Schlumberger, Etude sur la prospection electrique du sous-sol: (*Gauthier-Villars* 1920).

45. M.K. Sen and P.L. Stoffa, Nonlinear one-dimensional seismic waveform inversion using simulated annealing. *Geophysics* **56(10)** (1991) 1624-1638.

46. B.D. Sleeman, The Inverse Problem of Acoustic Scattering, *IMA J App Math* **29** (1982) 113-142.

47. V.N. Strakhov and M.A. Brodsky, On the uniqueness of the inverse logarithmic potential problem. *SIAM J Appl Math* **46(2)** (1986) 324-344.

48. C.K.W. Tam and J.C. Webb, Radiation Boundary Condition and Anisotropy Correction for Finite Difference Solutions of the Helmholtz Equation, *J Comp Phys* **113** (1994) 122-133.

49. A.N. Tikhonov and V.Y. Arsenin, "Solutions of ill-posed problems" (John Wiley & sons: New York, 1977), 426-432.

50. A.N. Tikhonov and A.A. Samarskii, "Equations of Mathematical Physics" (The MacMillan Co.: New York, 1963), 426-432.

51. D. Vanderbilt and S.G. Louie, A Monte Carlo Simulated Annealing Approach to Optimization over Continuous Variables, *J Comp Phys* **56** (1984) 259-271.

52. H.A. van der Vorst, Bi-CGSTAB: a fast and smoothly converging variant of Bi-CG for the solution of nonsymmetric linear systems, *SIAM J Sci Stat Comput* **13(2)** (1992) 631-644.

53. D.A. Williams *et al*, Cavendish Township Geophysical Test Range, 1973 Diamond Drilling, *Geol Survey of Canada* **74(62)**.

54. S. Xu, Z. Gao and S. Zhao, An integral formulation for three-dimensional terrain modelling for resistivity surveys, *Geophysics* **53(4)** (1988) 546-551.